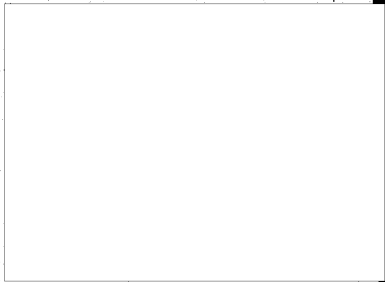


AFMDC TR 58-7
AD 135014

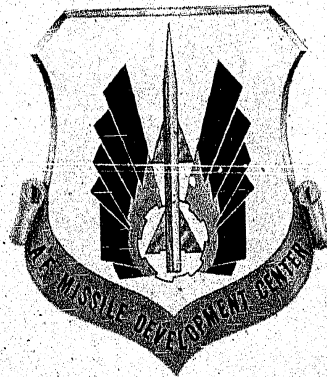
AFMDC TR 58-7
AD 135014

AIR FORCE MISSILE DEVELOPMENT CENTER TECHNICAL REPORT

**SOLAR FURNACE
SUPPORT STUDIES**



STAT



**HOLLOMAN AIR FORCE BASE
NEW MEXICO**

STAT

1958



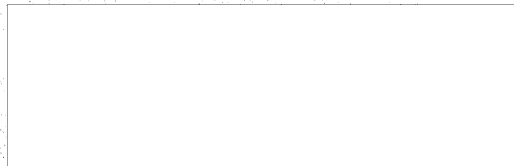
AFMDC TR 58- 7
AD 135014

AFMDC TR 58-7
AD 135014

SOLAR FURNACE SUPPORT STUDIES

prepared by

Scientific Consultants to the
Operations Research Office



STAT

AIR FORCE MISSILE DEVELOPMENT CENTER

AIR RESEARCH AND DEVELOPMENT COMMAND
UNITED STATES AIR FORCE
Holloman Air Force Base, New Mexico

1958

"Sun, stand thou still at Gibeon... and the sun stood still."

Joshua 10

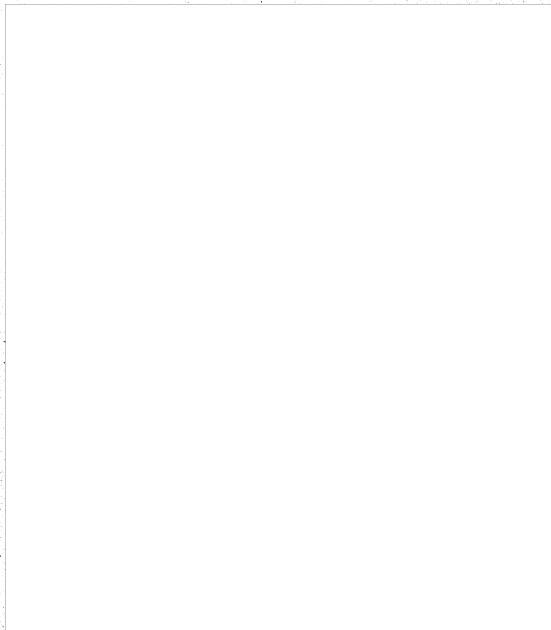
SUMMARY

This Technical Report is a consolidation of ten papers prepared by scientific consultants to the Operational Research Office at the Air Force Missile Development Center during the summer of 1957.

Each paper is the report submitted, upon the completion of his studies, by a consultant or consultant team. Pyrheliometer measurements showing the solar energy which can be expected to be available to a solar furnace located at Cloudcroft, New Mexico, are reported in the first paper. This is followed by an appraisal of the potential performance of such a solar furnace. The next paper, written by two of the nation's outstanding astronomers, explains certain basic optical considerations governing the design of solar furnaces. This is followed by three penetrating papers on the theory of absorption and reflection in solar furnace components and of the concentration of radiation through, and outside of, focal spots. Next is an examination of the rigid-body torsional oscillation which would result from aerodynamic excitation. Another study in which theories of transient temperature distribution in a solar target are discussed is followed by a presentation of an alternate design method.

FOREWORD

The order of arrangement of the individual papers was selected to secure as logical a presentation as possible for the reader who would choose to read the report from cover to cover. The sequence starts with measurement of solar energy, then to performance of the proposed Department of Defense furnace, then to considerations governing design, followed by theoretical studies which would pertain to any solar furnace, and lastly, to topics of least interest from the point of view of optical considerations and of least immediate practical application. The reader can stop at any point after the second paper and still have a fair concept of the proposed solar furnace.



STAT

Page Denied

CONTENTS

<u>Chapter</u>	<u>Page</u>
1. PRELIMINARY MEASUREMENTS OF THE SOLAR RADIATION AT CLOUDCROFT, NEW MEXICO	1
I. Introduction	3
II. Instrumentation	3
III. Measurements and Results	5
IV. Discussion	8
References	10
APPENDIX - Calibration Measurements	17
2. NOTES ON THE POTENTIAL PERFORMANCE OF THE CLOUDCROFT SOLAR FURNACE	23
I. Introduction	25
II. Mirror Locations	25
III. Off-axis Images from Spherical Mirrors	29
IV. Flux Concentration	32
References	38
3. SUGGESTED METHODS OF ALIGNING THE PLANES OF THE SOLAR FURNACE HELIOSTAT MIRRORS INTO PARALLELISM	47
I. An Optical Method	49
II. A Second Optical Method	52
III. A Mechanical Method	53

<u>Chapter</u>	<u>Page</u>
4. BASIC OPTICAL CONSIDERATIONS IN THE CHOICE OF A DESIGN FOR A SOLAR FURNACE	57
I. Introduction	59
II. Characteristics of a Paraboloid	64
III. Two-Mirror Systems	67
IV. Mounting for a Two-Mirror System	73
V. Alternative System Using a Paraboloidal Mirror	76
5. THE LOSS OF ENERGY BY ABSORPTION AND REFLECTION IN THE HELIOSTAT AND PARABOLIC CONDENSER OF A SOLAR FURNACE	89
I. The Method	91
II. Calculation of the Reflectivity of a Glass - Silver Mirror	92
III. Calculations	95
References	102
6. CALCULATION OF THE CONCENTRATION OF A SOLAR RADIATION THROUGH THE FOCAL SPOT OF A PARABOLIC MIRROR	105
I. The Method	107
II. Procedure	112
III. Check of the Formulas for a Uniform Sun	113
IV. Calculations	115
References	125
7. CALCULATION OF THE CONCENTRATION OF ENERGY AT POINTS OUTSIDE THE FOCAL SPOT OF A PARABOLIC CONDENSER	127
References	138

<u>Chapter</u>	<u>Page</u>
8. RIGID-BODY TORSIONAL OSCILLATIONS OF AXIALLY SUPPORTED HELIOSTAT MIRROR	141
I. Introduction	143
II. Numerical Data	145
III. Response to Random Torque Excitation	157
IV. Conclusions	160
9. TRANSIENT TEMPERATURE DISTRIBUTION IN A THERMALLY IRRADIATED BODY WITH VARIABLE HEAT-TRANSFER COEFFICIENT	169
I. Introduction	171
II. Results	172
References	181
APPENDIX I - Nomenclature	182
APPENDIX II - Sample Calculations	183
10. A SOLAR FURNACE USING A HORIZONTAL HELIOSTAT ARRAY	197
I. Introduction	199
II. The Condenser and Its Housing	199
III. The Heliostat	201
IV. The Turntable	203
V. Conclusion	205

CHAPTER 1

PRELIMINARY MEASUREMENTS OF THE
SOLAR RADIATION AT
CLOUDCROFT, NEW MEXICO

STAT



ABSTRACT

Measurements of the solar radiation at Cloudcroft, New Mexico, have been made with a normal incidence pyrheliometer. From the readings, an average transmittance has been determined that can be used to calculate the available flux at any time. Superscripts found through the text refer to numbered references.

I. Introduction

Preliminary design has been made for the construction of a large solar furnace near Cloudcroft, New Mexico, to be operated by the Air Force Missile Development Center for the Department of Defense. For proper utilization of the furnace, knowledge of the available solar energy is necessary. Spectroradiometric measurements⁽¹⁾ at nearby Sunspot, New Mexico, have furnished data for successfully determining the solar constant. However, accurate atmospheric transmission data are not available in the infrared portion of the spectrum and the amount of solar radiation received at Sunspot cannot be conveniently calculated. If these data were available, precise calculations of the received solar energy flux would be most difficult since intense water-vapor absorption bands (942, 1135, 1379, 1872 and 2650 μ) are located in a spectral region contributing about 40% of the total energy. To date, transmission coefficients in this infrared region are generally obtained from curves drawn smoothly over the tops of the water-vapor bands.⁽²⁾

In order that the amount of solar radiation be known at Cloudcroft, preliminary measurements at and near the proposed solar furnace site were made during the summer of 1957.

II. Instrumentation

A normal incidence pyrheliometer is generally employed for the measurement of the solar radiation.⁽³⁾ Calibrated instruments are

available⁽⁴⁾ and the manufacturer's bulletin should be consulted for construction details and performance characteristics of this type of pyrheliometer.

Attempts to obtain a calibrated pyrheliometer for immediate summer use at Cloudcroft were unsuccessful since a delivery date of over three months was required by the supplier. In order that normal incidence readings could be taken during the summer of 1957, a pyrheliometer was constructed jointly by the shops of the Air Force Missile Development Center and by the authors at Cloudcroft.

The initial sensing element of the instrument was similar to that used for radiation pyrometers⁽⁵⁾ and consisted of 10 copper-constantan thermocouples in series. The completed pyrheliometer had a radiation sensitivity of 0.2 millivolts per langley per minute, about one-tenth that of its manufactured counterpart. The thermopile was subsequently redesigned, using 8 copper-constantan thermocouples with the hot and cold junctions placed further apart. The new detecting element had an improved sensitivity of 4.1 mv/langley/minute, but required about five minutes for 95% response and eight minutes for steady-state response. While the long response time was disadvantageous for quick readings, it was tolerated.

The Cloudcroft pyrheliometer was calibrated in Tucson, Arizona, on August 2 against Eppley pyrheliometer No. 2191. The calibration

curve is shown in Figure 1. The abscissae are the dial readings of the potentiometer used to indicate the emf produced by the Cloudcroft instrument. The ordinates are the solar radiation values obtained from the Eppley pyrheliometer chart recording. The latter measurements are accurate within 2% according to Donovan and Bliss.⁽⁶⁾ A typical portion of the calibration measurements taken at Tucson are given in the Appendix.

III. Measurements and Results

The months of July and August constitute the rainy season at Cloudcroft and afforded little chance of obtaining continuous data. However, 26 readings of the pyrheliometer were obtained on the grounds of the Cloudcroft High School or on the proposed solar furnace site nearby. For normalization, these measurements were increased by an amount required to correct them to mean solar distance. Figure 2 shows the corrected radiant energy flux measurements plotted as a function of the number of unit air masses through which the flux travelled. The latter is taken as the secant of the angle between the zenith and the elevation of the sun.* The data roughly fall on a straight line and indicate that the flux ϕ received on the surface of the earth obeys Bouguer's law, viz.,

$$\phi = \phi_0 \tau^m \quad (1)$$

* An error of less than 1% results from neglecting the refraction in the atmosphere of the earth and its curvature up to air mass 3.

where ϕ_0 is the y-intercept of the curve, τ is the transmittance, and m the air mass.

A table of all values measured at Cloudcroft and the site is given in the Appendix. The corrections introduced for the difference in longitude and latitude between Cloudcroft and the site are not significant since the experimental error in determining ϕ can be as much as 5%. Therefore, the radiant flux values received at the two places are considered equal.

A calculation of m and the correction of ϕ to mean solar distance for one of the measurements are shown in the Appendix.

The ϕ_0 indicated on Figure 2 is not a constant during the year but is equal to the intercept value of 1.78 langley/min only on April 4 and October 5 when the relative radius of the earth equals unity. Figure 3 gives the variation of ϕ_0 as a function of the time of year.

Assuming the curve in Figure 2 represents the average of the data shown, the value of τ can be computed. Equation (1) then becomes

$$\phi \text{ (langleys/min)} = 1.78 (0.876)^m$$

and by calculating the pertinent m , ϕ can be found for any time of the year. Calculations for the value of ϕ at 11:00 on December 15 is given in the Appendix.

An alternate method for obtaining the flux at any time can be employed, using graphical procedures. Figure 4 is a plot of the ratio of

ϕ/ϕ_0 , using values from Figure 2. After the air mass m is calculated, the ratio of ϕ/ϕ_0 is obtained from Figure 4, and this ratio is multiplied by ϕ_0 from Figure 3. An example of a typical calculation made in this manner is found in the Appendix.

While the available radiant flux at the top of the atmosphere increases in the winter, due to the decrease in distance between the earth and the sun (Figure 3), the amount of flux available at the site can decrease in the winter since the elevation of the sun is less and the flux will traverse a much greater air mass. Figure 5 illustrates this variation. The ordinates are the flux ϕ calculated for 12:00 noon on the 15th day of each month. The graph shows that March, April, and May are the months having the highest available flux around the noon hour. It is significant to note that the noontime flux for the months of June, July, August, September, October, and February is only 2% less than the maximum. Only three months, November, December, and January, have an appreciable decrease which may influence the operation of the furnace.

Figure 5 shows about 5% variation in the noontime flux throughout the year. This curve may be deceptive for much larger variations will occur at other hours. At 11:00 a.m. on December 15, the available solar flux is 1.44 l/min., (see calculation in Appendix); this corresponds approximately to the flux received at 8:45 and 3:15 on April

15. Note also that the flux available at noon of December 15 is 1.44 l/min.

IV. Discussion

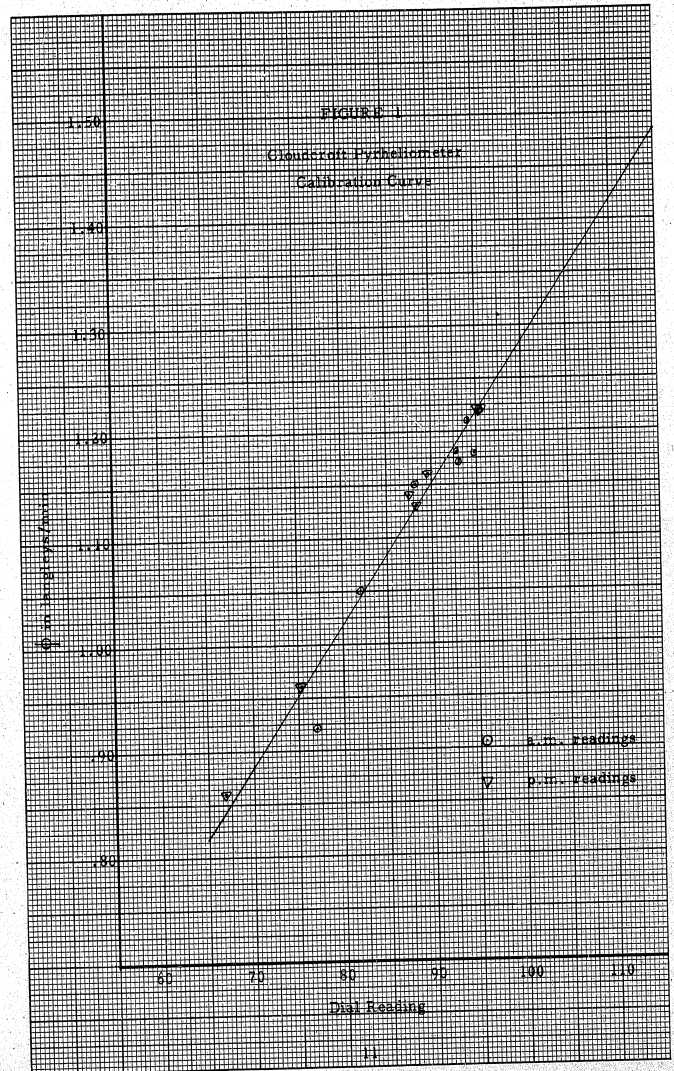
It is evident that curves given in Figures 3, 4, and 5 are greatly dependent on (1) the calibration curve (Figure 1) of the Cloudcroft pyr-heliometer, and (2) the slope of the line drawn in Figure 2. The data presented in Figure 2 indicate that a different slope might be drawn for morning and afternoon measurements. This same morning-afternoon characteristic exists for data taken at Tucson on August 2 with an Eppley pyr-heliometer. These data, corrected similarly to that in Figure 2, are shown in Figure 6. Also included are average data from Miami, Florida (sea level), and Montezuma, Chile (elevation 9,000 feet).⁽²⁾

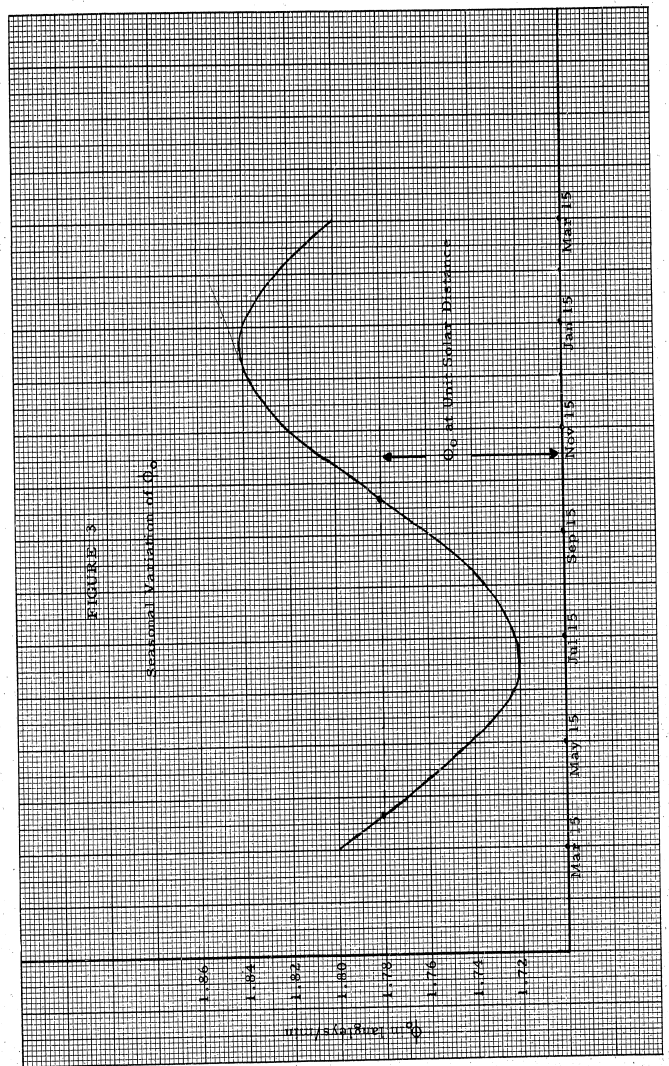
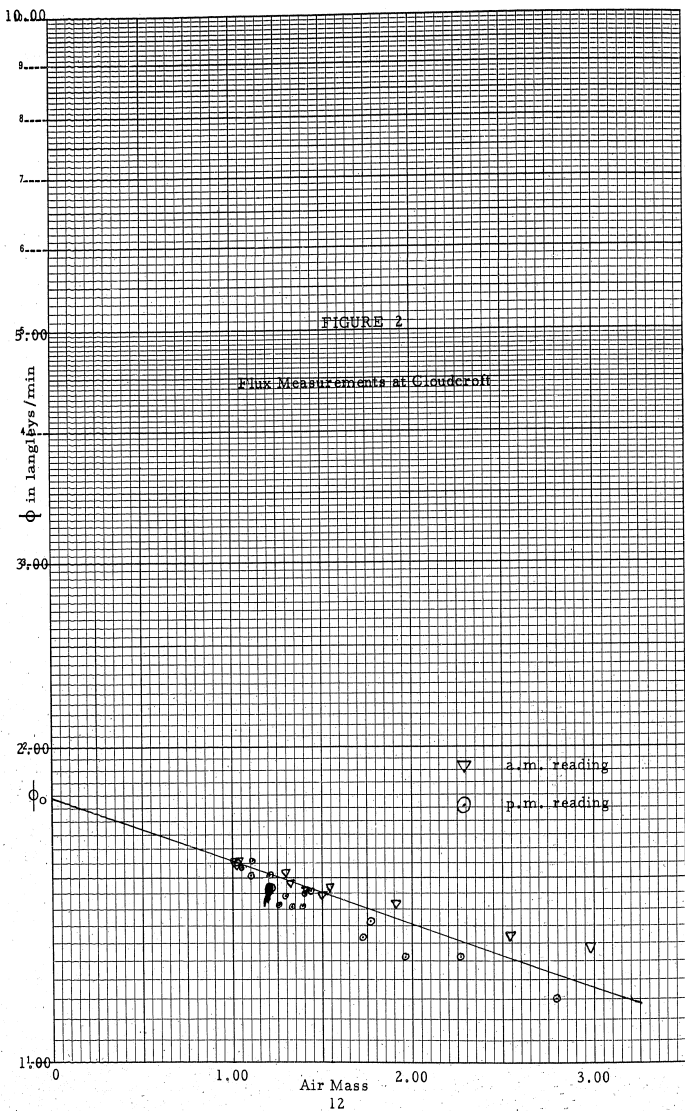
While the measurements are limited in number, the morning-afternoon recorded variations of ϕ having the same absorption path (or same air mass) appear real. The differences could be caused by a lack of an ambient correction to the pyr-heliometers although other workers⁽⁶⁾ do not find such an effect significant. The difference might also be due to non-linear scattering or absorption having a dependency on the time of day. Since the readings might also correctly indicate the solar flux at the time, no definite conclusions can be reached regarding this apparent effect until more data are available.

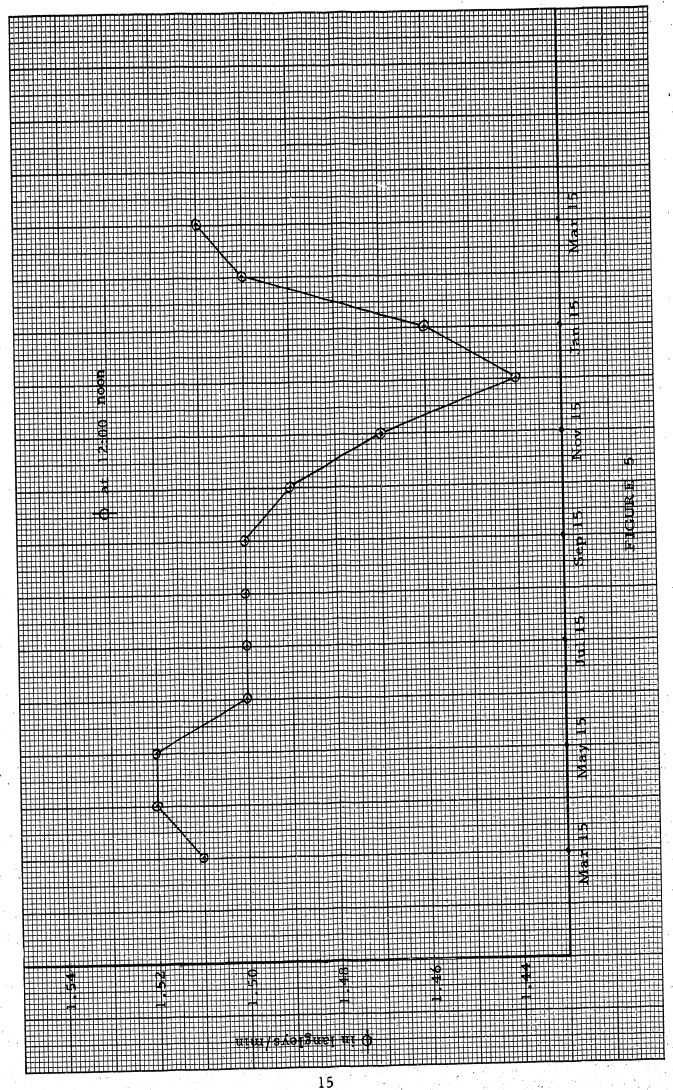
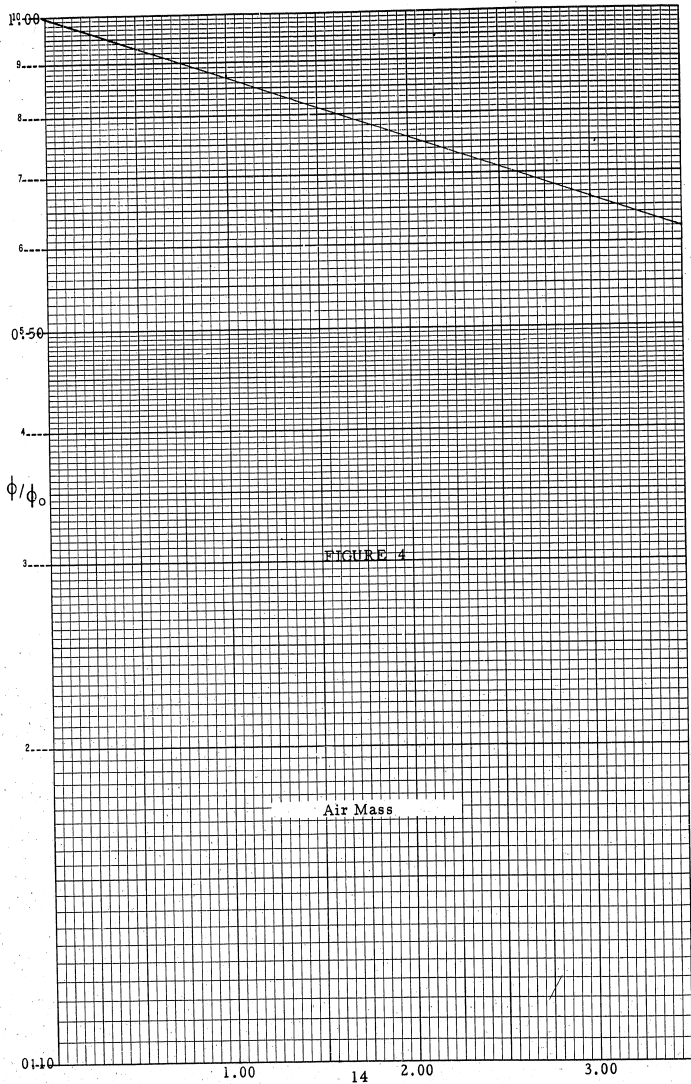
The data presented in Figure 2 are essentially an average of flux measurements taken in August. These measurements show a considerable spread but readings taken during a single day indicated good agreement. The data taken on August 26 are shown in Figure 7. Since seasonal and daily variations in ϕ are well known⁽²⁾, measurements should be taken over the year before extrapolation of these data to other months. This limitation is recognized but the methods employed in calculating data for Figures 3, 4, and 5 do not depend on the values of ϕ_0 and the calibration curve. When more accurate measurements of ϕ are made in sufficient quantity, the calculation of ϕ for any time of the day and year will be correspondingly more dependable.

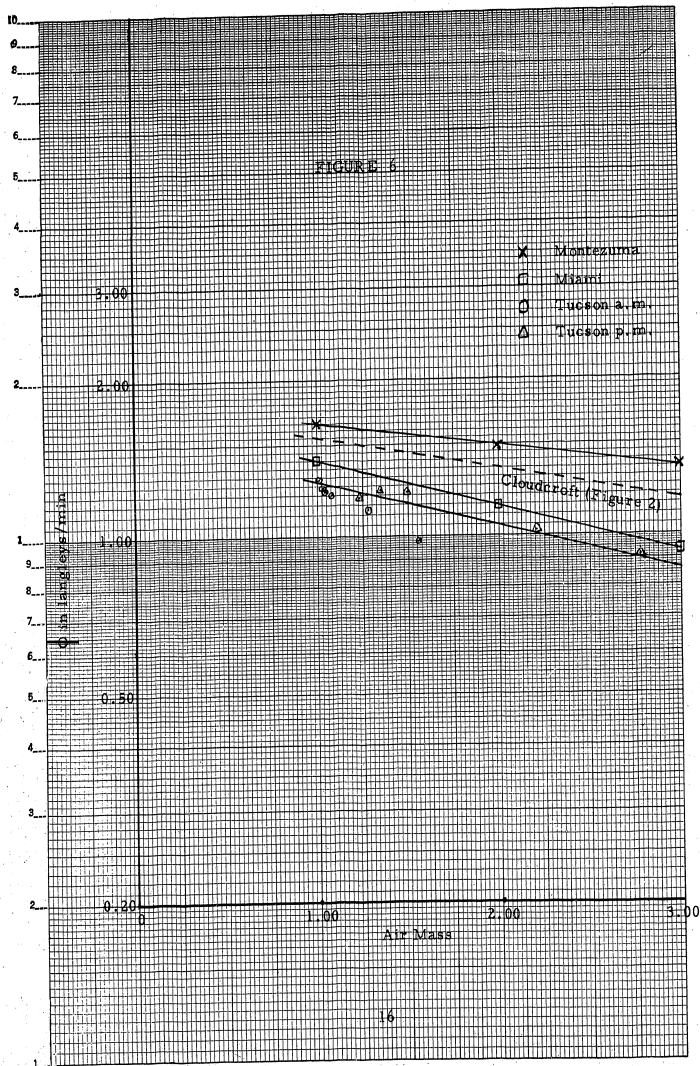
References

- (1) Ralph Stair and Russell G. Johnston, "Preliminary Spectroradiometric Measurements of the Solar Constant", Journal of Research of the National Bureau of Standards, Vol. 57 (1956), p. 205.
- (2) William E. Forsythe, Smithsonian Physical Tables, Ninth Revised Edition (1954), Smithsonian Institution, Washington.
- (3) I. F. Hand, "Pyrheliometers and Pyrheliometric Measurements", U. S. Weather Bureau, 1946.
- (4) The Eppley Laboratory, Inc., Newport, R. I.
- (5) T. R. Harrison and W. H. Wannamaker, "Improved Radiation Pyrometer", Temperature - Its Measurement and Control in Science and Industry, A Collection of Papers Presented in Symposium Held in 1939, Under the Auspices of the American Institute of Physics, Reinhold Publishing Corporation, New York, New York, Vol. 2 (1941), p. 1219.
- (6) Donovan and Bliss, "Field Calibration of Eppley Pyrheliometers Nos. 2191 and 2796", Technical Report No. 16, University of Arizona.









APPENDIX

Calibration Measurements

The following measurements are a portion of those taken on the roof of the Engineering Building at Tucson, Arizona, on August 2, 1957. The Cloudcroft instrument was located about 10 feet from the Eppley pyrheliometer. Clouds dotted the sky until about 11:00 a.m.; a shifting, milky haze was evident until 2:30 p.m. Thereafter, until late afternoon, the sky appeared clear.

Time (MST)	Dial Reading	Eppley Reading (langley/min)
11:01 a.m.	Pyrheliometer tube covered with aluminum foil.	
11:02	4.3	
11:04	.5	
11:06	-.2	
11:08	-1.5	
11:10	-2.0	
11:13	-2.2	
11:13:10	Pyrheliometer uncovered.	
11:14	76.0	
11:15	85.5	
11:16	88.2	
11:17	90.0	
11:18	90.3	
11:20	91.2	
11:21	92.0	
11:22	92.3	
11:23	92.8	
11:24	92.8	1.18
11:25	92.8	

Time (MST)	Dial Reading	Eppley Reading (langley/min)
11:25:10	Pyrheliometer covered.	
11:27	6.5	
11:29	3.0	
11:31	0.8	
11:32	-0.2	
11:33	-1.0	
11:34	-1.0	
11:35	-2.0	
11:37	-2.0	
11:37:10	Pyrheliometer uncovered.	
11:39	73.5	
11:40	84.5	
11:43	90.6	
11:44	91.5	
11:45	91.6	
11:46	92.0	
11:47	91.8	1.21
11:48	92.0	
11:49	92.0	

Measurements of ϕ at Cloudcroft

Summer 1957

Date	Time (Local sun time)	Air Mass m	ϕ in Langley/min (corrected to mean radius)	
July 27	8:00	1.73	1.31	
	29	12:00	1.03	1.55
		2:49	1.31	1.47
		3:09	1.40	1.46
		3:27	1.50	1.44
August	8	9:30	1.26	1.42
	9	9:14	1.33	1.41
		9:48	1.21	1.47
	10	11:55	1.05	1.54
		9:00	1.39	1.41
	12	9:26	1.29	1.44
		8:57	1.43	1.46
		9:58	1.20	1.51
	16	10:51	1.10	1.51
		7:54	1.96	1.26
	20	9:59	1.21	1.47
		7:33	2.27	1.26
	21	8:13	1.76	1.36
		7:09	2.79	1.15
	22	9:07	1.41	1.45
11:09		1.11	1.56	
23	2:23	1.30	1.51	
	3:13	1.54	1.47	
26	3:57	1.91	1.42	
	4:37	2.54	1.32	
	4:54	2.98	1.28	

Calculation of m and Correction of Measurement
of August 9 at 9:14 to Mean Solar Distance

Time: 9:17 MST, 9:14 local sun time
 Latitude θ : $32^{\circ}57'$
 Longitude: $105^{\circ}44'$
 Hour angle t : 2 hr 46 min = 41.6°
 Apparent declination of sun δ : $16^{\circ}10'$
 Measured ϕ : 1.37 langley/minute

$$\begin{aligned} h_s &= \text{elevation of the sun} \\ \sin h_s &= \sin \theta \sin \delta + \cos \theta \cos \delta \cos t \\ &= 0.753 \\ h_s &= 48^{\circ}50' \end{aligned}$$

$$\text{Air mass } m = \secant (90 - h_s) = 1.33$$

$$\text{Relative radius of earth} = 1.0139$$

$$\begin{aligned} \phi \text{ corrected to unit radius} &= 1.37 \times (1.0139)^2 \\ &= 1.41 \text{ langley/minute} \end{aligned}$$

Calculation of ϕ at Proposed Site
for 11:00, December 15

Latitude θ : $32^{\circ}57'$
 Longitude: $105^{\circ}44'$
 Hour angle t : 57 minutes = $14^{\circ}15'$
 Apparent declination of sun δ : $-23^{\circ}13'$

$$\begin{aligned} \sin h_s &= \sin \theta \sin \delta + \cos \theta \cos \delta \cos t \\ &= -0.2145 + 0.7473 = 0.5328 \\ h_s &= \text{elevation of sun} = 32^{\circ}12' \end{aligned}$$

$$\text{Air mass } m = \secant (90 - 32^{\circ}12') = 1.88$$

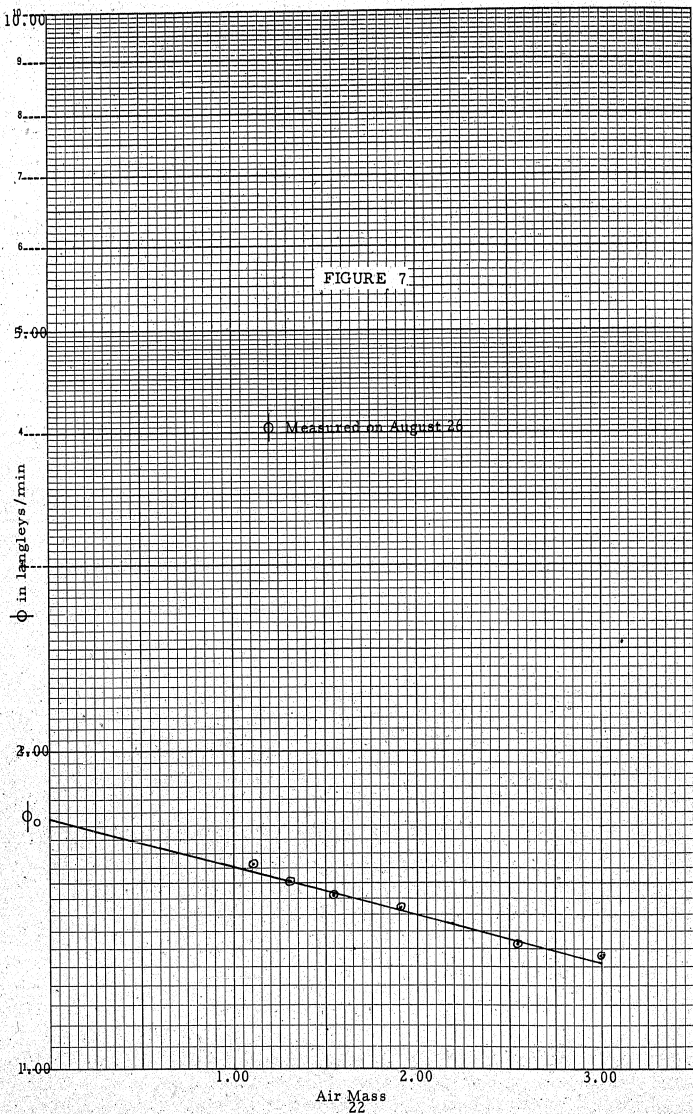
$$\phi_0 \text{ for December 15 (Figure 3)} = 1.84 \text{ langley/minute}$$

$$\phi = 1.84 (0.876)^{1.88} = 1.44 \text{ langley/minute}$$

Also:

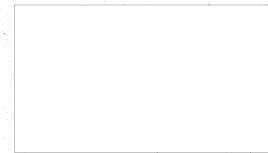
$$\phi/\phi_0 \text{ from Figure 4} = 0.787$$

$$\phi = 1.84 \times 0.787 = 1.44 \text{ langley/minute}$$



CHAPTER 2

NOTES ON THE POTENTIAL PERFORMANCE OF THE CLOUDCROFT SOLAR FURNACE



ABSTRACT

Using the specifications of the Cloudcroft Solar Furnace as prepared by the Pittsburgh-Des Moines Steel Company, the precise locations of mirror centers and edges are determined with respect to the principal axis of the optical system. The image formation from a single spherical mirror of the mosaic is examined at three locations and the flux concentration computed at two of these. It is shown that for the furnace as specified, placing the target at the secondary off-axis focal point of the individual mirrors produces a flux concentration on the target equal to that produced by a perfect parabola. This conclusion assumes a uniform flux distribution across the disc of the sun.

I. Introduction

The individual spherical mirrors making up the mosaic of mirrors of the condenser of the Cloudcroft Solar Furnace may be specified in a variety of focal lengths. Inasmuch as the choice of focal length may be one of the critical factors in determining the net flux concentration of the furnace, it is desirable to determine from the optics of off-axis image formation the optimum focal length of the mirrors in each annular ring of the mosaic.

II. Mirror Locations

These calculations are based on an aperture of the paraboloid of 105 ft. and a focal length of 44.76 ft. The mirrors forming the mosaic are, for these considerations, 2 ft. x 2 ft. squares as specified in the proposal of 18 May 1956, prepared by the Pittsburgh-Des Moines Steel Company, except for certain modifications suggested below. It is assumed that the mirrors are to be arranged in zones of concentric array around the vertex of the paraboloid.

a. Relationship between arc lengths (s) of the parabola and the corresponding ordinates (y):

$$s = \int_0^y \left[1 + \left(\frac{dy}{dx} \right)^2 \right]^{\frac{1}{2}} dx$$

However, from the equation of the parabola:

$$y^2 = 2px, \text{ hence: } \frac{dy}{dx} = \frac{p}{y}, \text{ and: } dx = \frac{y}{p} dy$$

$$s = \int_a^{y_1} \left(1 + \frac{p^2}{y^2}\right)^{\frac{1}{2}} \frac{y}{p} dy$$

$$s = \frac{1}{p} \int_a^{y_1} (y^2 + p^2)^{\frac{1}{2}} dy \quad (1)$$

The integral in Eq. (1) is readily evaluated:

$$s = \frac{y_1}{2p} \left(y_1^2 + p^2\right)^{\frac{1}{2}} + \frac{p}{2} \ln \left[\frac{y_1 + \left(y_1^2 + p^2\right)^{\frac{1}{2}}}{p} \right] \quad (2)$$

Successive integral values of y , at 2 ft intervals, are substituted in Eq. (2) and the corresponding values of s are computed as recorded in Columns 1 and 2 of Table I. In Column 4 of Table I are recorded values of y obtained by interpolation, corresponding to the integral values of s in Column 3. Since there is to be an aperture 12 ft. in diameter at the center of the paraboloid, the computed values begin with s equal to 7 ft.

The relationship between s and y is also shown graphically in Figure 8.

A record of all data computed in the evaluation of Eq. (2) is contained in Table VI in the Appendix.

Table I

y	s	s	y
7 ft.	7.00513 ft.	7 ft.	6.995 ft.
9	9.01605	9	8.984
11	11.02764	11	10.972
13	13.04516	13	12.995
15	15.0698	15	14.931
17	17.1021	17	16.900
19	19.1419	19	18.861
21	21.1903	21	20.814
23	23.2496	23	22.757
25	25.3212	25	24.690
27	27.4041	27	26.612
29	29.4986	29	28.524
31	31.6100	31	30.422
33	33.7323	33	32.310
35	35.8728	35	34.184
37	38.0282	37	36.046
39	40.1999	39	37.895
41	42.3917	41	39.730
43	44.5994	43	41.551
45	46.8282	45	43.360
47	49.0789	47	45.153
49	51.3471	49	46.930
51	53.6378	51	48.694
53	55.9518	53	50.443
55	58.2868	55	52.177

b. A meridian section of the paraboloid is shown in Figure 9, OX being the principal axis.

A spherical mirror M is tangent to the paraboloid at point P, on the center of which impinges a ray parallel to the principal axis of the paraboloid. From the geometry of Figure 9, the values of the designated angles ϕ , i , θ and length L are calculated and tabulated in Table II.

Table II

Zone	s	y	ϕ	i	θ	L
1	7 ft.	6.995 ft.	85°32'	4°28'	81°04'	45.045 ft.
2	9	8.984	84°16'	5°44'	78°32'	45.191
3	11	10.972	83°01'	6°59'	76°02'	45.459
4	13	12.995	81°46'	8°14'	73°32'	45.703
5	15	14.931	80°32'	9°28'	71°04'	46.017
6	17	16.900	79°19'	10°41'	68°38'	46.421
7	19	18.861	78°06'	11°54'	66°12'	46.738
8	21	20.814	76°55'	13°05'	63°50'	47.199
9	23	22.757	75°44'	14°16'	61°28'	47.642
10	25	24.690	74°35'	15°25'	59°10'	48.172
11	27	26.621	73°27'	16°33'	56°54'	48.731
12	29	28.524	72°20'	17°40'	54°40'	49.321
13	31	30.422	71°14'	18°46'	52°28'	49.936
14	33	32.310	70°09'	19°51'	50°18'	50.582
15	35	34.184	69°06'	20°54'	48°12'	51.287
16	37	36.046	68°04'	21°56'	46°08'	52.016
17	39	37.895	67°03'	22°57'	44°06'	52.769
18	41	39.730	66°04'	23°56'	42°08'	53.574
19	43	41.551	65°06'	24°54'	40°12'	54.406
20	45	43.360	64°09'	25°51'	38°18'	55.251
21	47	45.153	63°14'	26°46'	36°28'	56.146
22	49	46.930	62°20'	27°40'	34°40'	57.059
23	51	48.694	61°27'	28°33'	32°54'	57.995
24	53	50.443	60°36'	29°24'	31°12'	58.973
25	55	52.177	59°46'	30°14'	29°32'	59.969

The variation of L with arc length is shown graphically in Figure 10.

It is to be noted that the values of s and y given in Tables I and II refer to the mid-points of the respective mirrors, while in Table III they refer to the inner edges of the mirrors.

Table III

Zone	s	y	Zone	s	y
1	6	5.9980 ft.	13	30	29.475 ft.
2	8	7.9895	14	32	31.366
3	10	9.9780	15	34	33.247
4	12	11.9635	16	36	35.115
5	14	13.943	17	38	36.970
6	16	15.916	18	40	38.812
7	18	17.880	19	42	40.640
8	20	19.838	20	44	42.455
9	22	21.786	21	46	44.256
10	24	23.732	22	48	46.041
11	26	25.651	23	50	47.812
12	28	27.568	24	52	49.568
			25	54	51.310

III. Off-axis Images from Spherical Mirrors

a. The astigmatic image distances s_1 and s_2 of Figure 11, as measured along the chief ray, are known to be related to the angle of incidence and reflection i , the object distance s and the radius of curvature r of the reflecting surface by ⁽¹⁾

$$\frac{1}{s} + \frac{1}{s_2} = \frac{2}{r \cos i} \quad (3)$$

for the primary or tangential focus s_2 , and

$$\frac{1}{s} + \frac{1}{s_1} = \frac{2 \cos i}{r} \quad (4)$$

for the secondary or sagittal focus s_1 .

Taking the object distance s as infinity, s_1 and s_2 become F_1 and F_2 , the principal astigmatic focal points by definition, and the equations reduce to

$$\frac{1}{F_2} = \frac{2}{r \cos i} \text{ or } F_2 = \left(\frac{r}{2}\right) \cos i \quad (5)$$

$$\frac{1}{F_1} = \frac{2 \cos i}{r} \text{ or } F_1 = \left(\frac{r}{2}\right) \frac{1}{\cos i} \quad (6)$$

The distance between the two principal focal points measured along the chief ray is:

$$F_1 - F_2 = \frac{r}{2} \tan i \sin i.$$

A concave spherical mirror of square section EFGH, as in Figure 12, forms two line images JK and LM centered on the chief ray BC when the incident light strikes the mirror off-axis as along the line AB at angle i to the normal BD. The secondary or sagittal image lies in a plane containing the chief rays while the primary or tangential image stands normal to such a plane. The image distances in Equations (5) and (6) above are measured along line BC.

b. By constructing a plane that includes BC, the image JK and the aperture width ($NP = a$) of the concave spherical mirror, one may show that the length w of the line image JK is:

$$w = a \sin^2 i \quad (7)$$

and, with a plane at right angles to this that includes line image LM,

the length ℓ of this image is:

$$\ell = a \tan^2 i \quad (8)$$

Only when an infinitely narrow bundle of rays forms the images above are these images line images. The conical bundle of rays from the sun of angle α in diameter forms an image composed of a series of overlapping circles whose centers lie on ℓ or w as the case may be. Since the diameter of these circles is the product of the distance from the point in the image to the point on the mirror from which the light comes and the angular diameter of the sun, it is apparent that image JK will have the dimensions of Figure 13a and image LM, those of 13b, where L is taken as BC, JK as w , and LM as ℓ in Figure 5.

The slight distortion of Figure 13b comes from the fact that in Figure 12, rays HL and GL are shorter than rays EM and FM. The image distortion effect in this instance is negligible since the mirror aperture and image lengths are small compared to the focal length and will, therefore, be neglected in the discussion below. The similar effect in image JK is to make the image edge poorly defined. The image formed on a screen placed midway between JK and LM and at a distance L from the mirror will be in the form of a rectangle with rounded corners. The radius of the corners will be $\frac{\alpha L}{2}$ and the width and length of the rectangle will be $1/2 w + \alpha L$ and $1/2 \ell + \alpha L$, respectively.

IV. Flux Concentration

a. On the assumption that the intensity across the three images above is constant, the one of smallest dimensions should have the highest flux density and should, therefore, be used as the focal point for the separate spherical mirrors of the solar furnace array. Since a $\sin^2 i$ is always smaller than a $\tan^2 i$, and the third case above is intermediate, the primary or w focus appears most favorable.

b. The efficiency of a single spherical mirror in sending light flux to a target is seen as the ratio of the area of the target when projected onto a plane normal to the chief ray from the spherical mirror, to the area of the image of the sun on this plane as produced by the spherical mirror. It is therefore;

$$\text{Efficiency} = \frac{\left(\frac{\alpha F}{2}\right)^2 \pi \sin \theta}{\left(\frac{\alpha L}{2}\right)^2 \pi + \alpha L w} \quad (9)$$

The flux produced at the target may be obtained from the projected area of the circular ring or zone of mirrors of which the mirror evaluated in Eq. (9) was a part, the solar constant and the efficiency. The flux in cal/sec contributed by the zone is;

$$\text{Flux} = \left(\frac{Y^2 \pi}{2} - \frac{Y_1^2 \pi}{1}\right) \text{ cm}^2 \times 0.0264 \text{ cal/cm}^2/\text{sec} \times \text{efficiency.} \quad (10)$$

Considering the solar constant as 0.0264 cal/cm²/sec, the focal length of the parabolic mirror array as 44.76 ft, the mean diameter of the sun as 32', and the mirrors each 2 ft x 2 ft, the values of L, θ , i, and y from Tables I and II permit the efficiencies of spherical mirrors as they might actually be employed. Column 2 of Table IV lists these calculated values.

Table IV

Zone No.	Spherical Mirrors Efficiency	Spherical Mirrors Flux(cal/sec)	Parabolic Mirrors Efficiency	Parabolic Mirrors Flux(cal/sec)	Cumulative Flux Total
1	0.941	1874	0.975	1943	
2	0.906	2496	0.961	2647	4,590
3	0.864	2900	0.941	3158	7,748
4	0.817	3228	0.919	3631	11,378
5	0.771	3500	0.895	4062	15,441
6	0.720	3681	0.866	4429	19,868
7	0.672	3822	0.839	4775	24,643
8	0.622	3887	0.807	5042	29,685
9	0.575	3903	0.775	5267	34,952
10	0.529	3879	0.714	5437	40,389
11	0.485	3815	0.707	5555	45,944
12	0.445	3726	0.672	5631	51,574
13	0.406	3602	0.637	5648	57,222
14	0.371	3473	0.603	5642	62,864
15	0.337	3321	0.568	5587	68,450
16	0.308	3171	0.534	5500	73,950
17	0.280	3010	0.501	5384	79,335
18	0.254	2846	0.468	5239	84,574
19	0.231	2682	0.437	5076	89,650
20	0.209	2519	0.407	4893	94,543
21	0.190	2358	0.378	4691	99,234
22	0.172	2203	0.350	4483	103,716
23	0.156	2050	0.323	4262	107,979
24	0.141	1906	0.298	4040	112,019
25	0.127	1782	0.274	3846	115,865

The flux contribution of each mirror ring zone is presented in Column 3 of Table IV. It is to be noted that the values of s are odd numbered for the efficiency calculation since values for mirror centers are required; however, for flux calculations, s and y are for even numbered positions, since edge measurements are required.

Unfortunately, the total flux from this calculation reaches a value of only 75,634 calories/sec while 88,690 calories/sec are required for a flux density of 700 cal/cm²/sec.

c. It is a fact that the flux density across the mirror image is not constant as was assumed above, but is constant along the length l or w only when these lengths are greater than αL . When the lengths l or w are less than αL , as in Figure 14, the extreme images, produced by the edges of the mirror, overlap and in the overlapped section the light comes from all areas of the mirror. This fact permits a recalculation of the efficiency of the spherical mirror in that in the overlapped section, the spherical mirror is equal in light concentration efficiency to the parabolic mirror.

For the sagittal focus of a spherical mirror, the overlap section, if one occurs, approximates the shape of the target projection as referred to above. Moreover, if 1 ft x 2 ft mirrors are used instead of the 2 ft x 2 ft ones as presently planned for the solar furnace, the dimensions and area of the overlap section approximately equal those

of the projected target. These comparisons are shown in Table V below.

Table V

Zone No.	Overlap Section of 1 x 2 ft Mirrors			Target Projection		
	a	b	Area	Major Axis	Minor Axis	Area
1	0.4887 ft.	0.4126 ft.	0.1315 ft. ²	0.4159 ft.	0.4110 ft.	0.1342 ft. ²
2	0.4200	0.4100	0.1344	Same	0.4078	0.1333
3	0.4223	0.4076	0.1339	value	0.4038	0.1319
4	0.4243	0.4039	0.1329	for	0.3986	0.1303
5	0.4268	0.4000	0.1318	all	0.3936	0.1286
6	0.4301	0.3957	0.1309	zones	0.3875	0.1266
7	0.4322	0.3901	0.1290		0.3807	0.1244
8	0.4354	0.3847	0.1275		0.3734	0.1220
9	0.4381	0.3782	0.1255		0.3655	0.1195
10	0.4413	0.3718	0.1236		0.3573	0.1167
11	0.4443	0.3647	0.1214		0.3486	0.1139
12	0.4462	0.3571	0.1172		0.3394	0.1109
13	0.4492	0.3488	0.1162		0.3299	0.1078
14	0.4518	0.3399	0.1132		0.3201	0.1046
15	0.4548	0.3309	0.1100		0.3102	0.1014
16	0.4560	0.3214	0.1069		0.3000	0.9803
17	0.4566	0.3112	0.1030		0.2896	0.9463
18	0.4575	0.3010	0.0993		0.2791	0.9122
19	0.4575	0.2903	0.0952		0.2686	0.8777
20	0.4568	0.2789	0.0909		0.2579	0.8427
21	0.4557	0.2675	0.0850		0.2473	0.8082
22	0.4536	0.2556	0.0820		0.2367	0.7734
23	0.4506	0.2431	0.0771		0.2260	0.7386
24	0.4469	0.2307	0.0723		0.2151	0.7044
25	0.4420	0.2178	0.0672		0.2051	0.6703

These data make it appear that the projected area of the target may all lie within the overlapped sections of the mirror images.

Under these circumstances, the flux produced by each pair of 1 ft x 2 ft mirrors may be computed as though they were parabolic sections making images $\propto L$ in diameter. The efficiencies of such parabolic mirrors may be calculated as:

$$\text{Efficiency} = \frac{\left(\frac{\alpha F}{2}\right)^2 \pi \sin \theta}{\left(\frac{\alpha L}{2}\right)^2 \pi} \quad (11)$$

and are shown in Column 4 of Table IV, and the flux contribution as calculated from Eq. (10) for each zone is shown in Column 5 of that Table.

A minor error in the results tabulated should be noted here. The substitution of 1 ft x 2 ft mirrors naturally doubles the number of values of L , i , etc., and the number of mirror zones. This effect was not considered in the computation since the smaller mirrors were considered as located centrally in the space required for the larger ones. A recalculation of the flux concentration based on a more exact formulation would tend to raise the flux values given above.

Column 6 of Table IV is the cumulative total of the flux contributions of the several zones, starting with the innermost zone; On the basis of 100% efficiency (with no losses due to absorption, reflection and shadowing) a mirror of 19 zones would suffice to achieve a flux density of 700 cal/cm²/sec. If the entire 25 zones are used, this same flux

density may be achieved with an overall loss due to above effects of 23.5%.

d. The calculations of the flux contributions of the several mirrors to the target have not considered the effect of the limb darkening of the sun as described by Jose.⁽²⁾ It is to be noted that in the scheme proposed here, the target projection does not lie in the center of a circular focal spot for a single mirror, and, therefore, the percentage increase in flux due to limb darkening may not be in the amount Jose proposes.

References

- (1) R. A. Houston, "Treatise on Light", Longman's-Green and Company, Inc., New York, New York, 1938.
- (2) Paul D. Jose, "The Flux Through the Focal Spot of a Solar Furnace", Holloman Air Development Center, Technical Memorandum No. HDRRM-TM-57-3, April 1957.

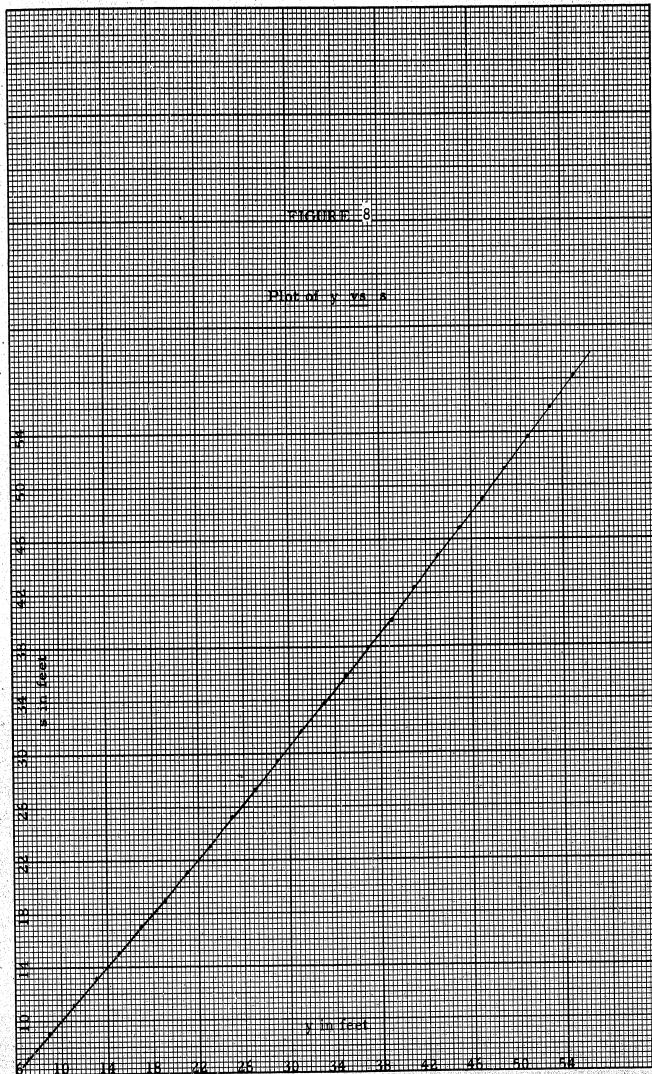


FIGURE 9

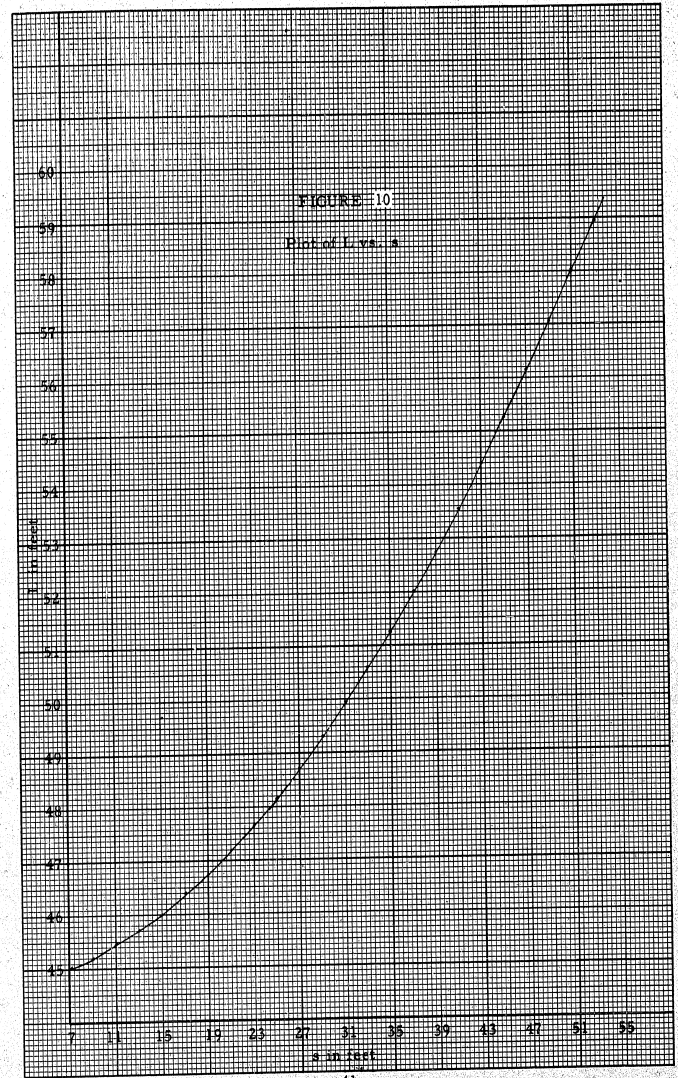
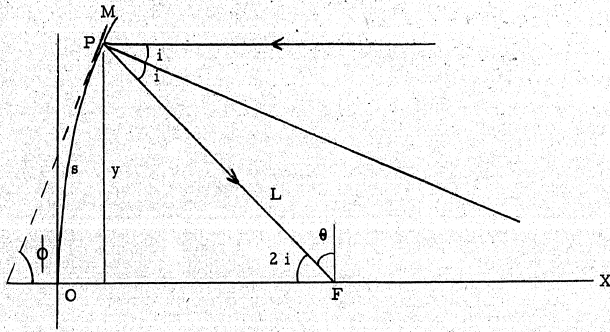
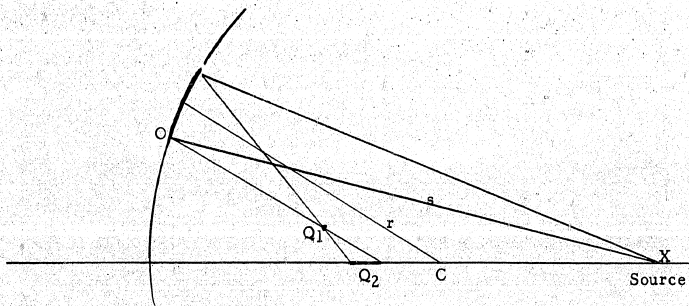
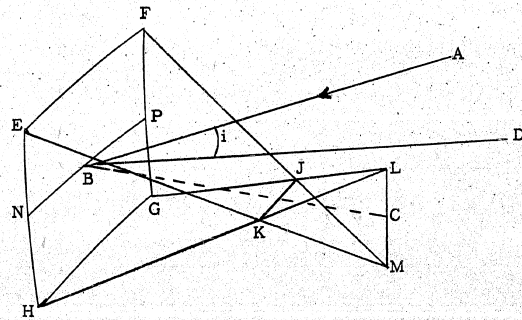


FIGURE 11
OFF-AXIS IMAGE



$s_1 = OQ_1$
 $s_2 = OQ_2$

FIGURE 12



$NP = a$
 $JK = w$
 $LM = l$

FIGURE 13

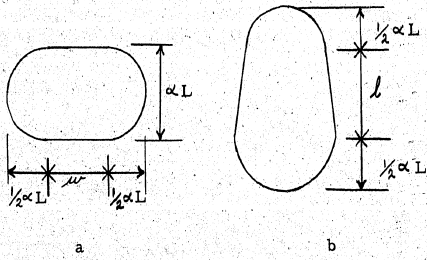
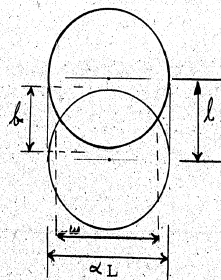


FIGURE 14



APPENDIX

Table VI

y	$\frac{y}{2P}$	y^2	$y^2 + P^2$	$\sqrt{y^2 + P^2}$	$y + \sqrt{y^2 + P^2}$	$\frac{y + \sqrt{y^2 + P^2}}{P}$	$\frac{y}{2P} \sqrt{y^2 + P^2}$	$\frac{P}{2} \ln \left(\frac{y + \sqrt{y^2 + P^2}}{P} \right)$	$S = \frac{y}{2P} \sqrt{y^2 + P^2} + \frac{P}{2} \ln \left(\frac{y + \sqrt{y^2 + P^2}}{P} \right)$
7	0.0390974	49	8062.83	89.7932	96.7932	1.08125	3.51068	0.078071	7.00513
9	.0502681	81	8094.83	89.9713	98.9713	1.10558	4.52269	0.100388	9.01605
11	.0614387	121	8134.83	90.1933	101.1933	1.13040	5.54136	.122571	11.02764
13	.0726094	169	8182.83	90.4590	103.4590	1.15571	6.56817	.144705	13.04516
15	.0837801	225	8238.83	90.7680	105.7680	1.18150	7.60455	.166784	15.0698
17	.0949508	289	8302.83	91.1199	108.1199	1.20777	8.65191	.188789	17.1021
19	.1061215	361	8374.83	91.5141	110.5141	1.234519	9.71161	.210686	19.1419
21	.1172921	441	8454.83	91.9501	112.9501	1.261731	10.78502	.232468	21.1903
23	.1284628	529	8542.83	92.4274	115.4274	1.289404	11.87348	.254159	23.2496
25	.1396335	625	8638.83	92.9453	117.9453	1.317530	12.97828	.275757	25.3212
27	.1508043	729	8742.83	93.5031	120.5031	1.346103	14.10067	.297217	27.4041
29	.1619749	841	8854.83	94.1001	123.1001	1.375112	15.24185	.318516	29.4986
31	.1731455	961	8974.83	94.7356	125.7356	1.404553	16.40304	.339746	31.6100
33	.1843162	1089	9102.83	95.4088	128.4088	1.434415	17.58539	.360745	33.7323

Table VI (Continued)

y	$\frac{y}{2P}$	y^2	$y^2 + P^2$	$\sqrt{y^2 + P^2}$	$\frac{y + \sqrt{y^2 + P^2}}{P}$	$\frac{y}{2P} \sqrt{y^2 + P^2}$	$\frac{y}{2P} \ln \left(\frac{y + \sqrt{y^2 + P^2}}{P} \right)$	$\frac{y}{2P} \sqrt{y^2 + P^2} + \frac{P}{2} \ln \left(\frac{y + \sqrt{y^2 + P^2}}{P} \right)$
35	0.1954869	1225	9238.83	96.1188	1.464687	18.78997	.381653	35.8728
37	.2066576	1369	9382.83	96.8650	1.495364	20.01789	.402376	38.0282
39	.2178283	1521	9534.83	97.6465	1.526435	21.27017	.422915	40.1999
41	.2289989	1681	9694.83	98.4623	1.557889	22.54776	.443339	42.3917
43	.2401696	1849	9862.83	99.3118	1.589721	23.85167	.463532	44.5994
45	.2513403	2025	10038.83	100.1940	1.621917	25.18379	.483588	46.8282
47	.2625110	2209	10222.83	101.1080	1.654469	26.54196	.503505	49.0789
49	.2736817	2401	10414.83	102.0531	1.687367	27.93007	.523169	51.3471
51	.2848523	2601	10614.83	103.0283	1.720602	29.34784	.542672	53.6378
53	.2960230	2809	10822.83	104.0328	1.754164	30.79610	.562014	55.9518
55	.3071937	3025	11038.83	105.0658	1.788045	32.27555	.581125	58.2868

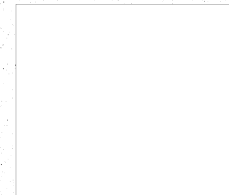
$F = 44.76 \text{ ft.}$

$P = 89.52 \text{ ft.}$

$P^2 = 8013.83 \text{ ft.}^2$

CHAPTER 3

SUGGESTED METHODS OF ALIGNING THE PLANES OF THE SOLAR FURNACE HELIOSTAT MIRRORS INTO PARALLELISM



STAT

ABSTRACT

Three possible methods for measuring the alignment of the planes of the individual mirrors of the heliostat of the proposed Department of Defense solar furnace are described. Two of the methods are optical and one is mechanical. The optical methods require, in one case, a theodolite of high precision and large aperture, and, in the other case, a specially built instrument as shown in Figure 18. The mechanical method would use high precision spirit levels with the heliostat set in the horizontal plane.

I. An Optical Method (By Dr. Fred Allison)

This method is based on adjustments made possible by means of the Gaussian eyepiece.

The frame holding the heliostat mirrors is brought as nearly as possible into the East-West vertical plane and clamped. *With the heliostat so positioned, the mirrors, one by one, are to be aligned with their planes parallel by means of the adjustment screws.

A theodolite of high precision and large aperture, securely mounted on a "cat walk" in as close proximity as possible to the heliostat mirror, is adjusted so that the azimuth circle and the axis of the telescope lie in horizontal planes.

In order to expedite the work of alignment, it is suggested that the mirrors in groups of four may be aligned without resetting the theodolite, in the following manner.

The theodolite telescope, its axis set in the N-S plane and the cross-hairs of the Gaussian eyepiece properly illuminated, is directed at the contiguous corners of four mirrors, as A, B, C, D. (See Figs.

*Note: The foregoing paper was written early in the summer, when it was understood, according to temporary plans then available, that the heliostat mirror could be set in the vertical plane. Revised plans do not permit vertical setting of the heliostat mirror. For positions of the heliostat mirror other than vertical, the method above suggested, with certain obvious modifications in the adjustment of the theodolite and the constant-deviation prism, should have practically the same applicability.

15 and 16) One of these mirrors, say A, is adjusted by the screws until it is autocollimated with the telescope, i. e., until the light reflected from A forms an image of the cross-hairs in coincidence with the direct image of the cross-hairs as seen in the eyepiece.

In a precisely similar manner, one proceeds with the adjustment of B to obtain coincidence of the cross-hair image with the two already in coincidence. In the same way the cross-hair image due to light reflected from C is brought into coincidence with the other three; and finally, the image due to D. Five cross-hair images would thus be in coincidence when the planes of the four mirrors are parallel. If the multiplicity of cross-hair images in the field of view should cause confusion, one could first adjust mirror A, with the corners of B, C, and D covered, then proceed to align each of these three in turn, keeping the corners of the others covered.

The operation described above would be repeated for other groups of four mirrors in the same double row until all mirrors of the heliostat were included.

Some variations in the procedure may be suggested.

a. Set the telescope on the four contiguous corners of mirrors B, D, E, and G. (See Fig. 15) Instead of readjusting the theodolite by the levels, adjust it until the cross-hair image due to B (and D) falls on the cross-hairs of the eyepiece. Then adjust E and G as above described.

The next setting would be in the corners of E, F, G, H, and so on. This process would align only two mirrors at a setting and the errors would be accumulative.

b. Instead of working with the groups of four mirrors, groups of two, as M, N, etc., using the same method, may be aligned across each horizontal row.

Once the mirrors are adjusted for parallelism, the test for accumulated errors in their overall alignment throughout the heliostat mosaic is suggested as indicated below.

The telescope is autocollimated on a selected mirror and is then accurately turned in azimuth through 90° looking into a constant-deviation prism which is on an adjustable mounting in front of a second selected mirror in the same horizontal row. (See Fig. 17) If the planes of the two selected mirrors have been correctly aligned, the light incident on the second selected mirror will retrace its path through the constant-deviation prism, and the cross-hair images due to the returned light will be in coincidence with the cross-hair image of the eyepiece. By proper adjustment of the telescope in altitude, the second mirror may be selected in any horizontal row as well as in any vertical column of mirrors.

Whether the methods above suggested would yield satisfactory results could be determined by preliminary experimentation.

II. A Second Optical Method (By Dr. Gordon Hughes)

The method to be proposed assumes that an observer and a device may be held in a relatively fixed position within some 10 ft of the heliostat mirrors.

Suppose a relatively rigid metal tube, say some 8 to 9 ft long, is provided with side ports as indicated in Figure 18. Mirror "a" is a half-silvered surface placed at 45° with the axis of the tube. Mirror "b" is full silvered and placed as shown. An electric lamp with its filament in the shape of an x is placed at the focal point of lens L_1 and observed through lens L_2 with an eye lens.

Two dishes of mercury, M_1 and M_2 , are observed. Since these two surfaces are parallel, two images of the light source indicate that mirror "b" should be adjusted until the single image of the lamp filament is seen. A color filter at point F in the system might be employed to distinguish the light returned from the two floating mirrors.

Now if the device is placed before two of the heliostat mirrors instead of the two floating mirrors they may be aligned with an accuracy determined by the sharpness of the lamp filaments and their magnification.

If the alignment procedure starts at one side of the heliostat and progresses across the entire face, an error may accumulate of sufficient magnitude to render the alignment as unsatisfactory. Since the

instrument is designed with appreciable length, it should be possible to align alternate mirrors and then check between the alternate pairs.

A penta prism may be employed to replace mirror "b" if the deformation of the tube under its own weight throws the device out of alignment.

Advantages of this method of alignment:

- a. There is no loading of the glass surface using this technique.
- b. The mirrors may be aligned when the heliostat is in any position.
- c. The reference signal is from the heliostat itself with this device so that random motions of the heliostat from wind gusts will not negate the method.
- d. The device will work even though it may be turned through small angles with reference to the normal to the mirrors.
- e. Cumulative errors in the alignment may be detected and corrected.

III. A Mechanical Method (By Dr. Fred Allison)

This method is based on the possibilities of achieving horizontal adjustments of plane surfaces by means of high precision spirit levels of the cross-arm type. It is assumed that in the revised design of the heliostat mounting the mosaic mirror may be set in the horizontal plane. With the mirror so positioned and with a movable walk-way immediately

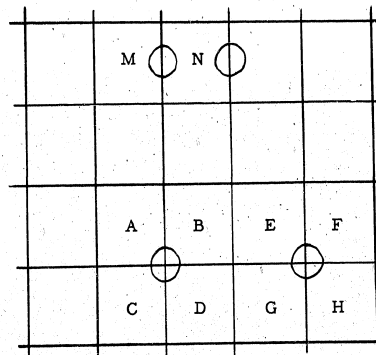
above the mirror, the procedure of bringing in turn, by the adjustment screws, each of the component mirrors into the horizontal plane as determined by the spirit level, could be accomplished with comparative ease and speed. The work could be facilitated by using a number of workers, each provided with a properly designed spirit level.

This method appears to have the following advantages:

- a. Precision comparable and probably superior to that of optical methods.
- b. No accumulative errors.
- c. Highly trained personnel not required.
- d. Ease and speed of operation.

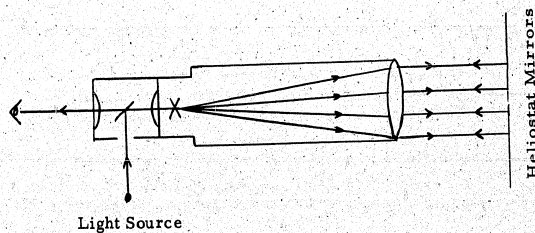
A disadvantage as compared with optical methods: The spirit level would make contact with each mirror, adding its weight thereto.

Heliostat Mirrors



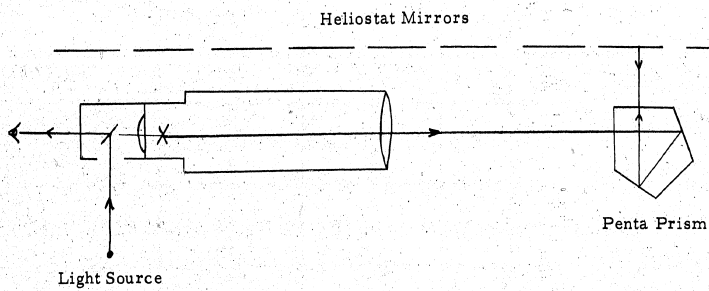
(Not to Scale)

FIGURE 15



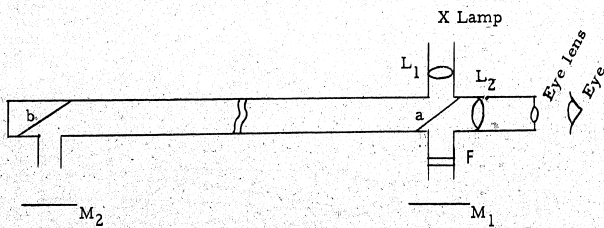
(Not to Scale)

FIGURE 16



(Not to Scale)

FIGURE 17

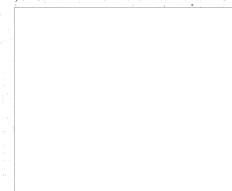


(Not to Scale)

FIGURE 18

CHAPTER 4

BASIC OPTICAL CONSIDERATIONS
IN THE CHOICE OF A
DESIGN FOR A SOLAR FURNACE



STAT

ABSTRACT

Simple relationships exist between the aperture of a solar furnace, the target size, the angle of convergence, the maximum attainable concentration ratio, the overall efficiency, and the amount of spill light surrounding the target. For optical systems having continuous unobstructed surfaces and no spherical aberration, the concentration ratio is determined solely by the angle of convergence. Various systems differ considerably, however, in the amount by which their apertures exceed that of an ideal system of equal performance; in the resulting efficiency at which

they operate; in the associated amount of waste light spilled outside the target; in the distribution of this spill light; and in the relative convenience with which they can be fabricated and adjusted. A paraboloidal mirror with heliostat does not seem to be an optimum choice. The optical possibilities afforded by other two-mirror systems are discussed and illustrated by example. We also present a structural design for a two-mirror system which appears to possess some practical advantages over the heliostat-paraboloid combination.

I. Introduction

The purpose of a solar furnace is to concentrate as much flux as possible onto a specified target area. There are many different optical systems which might be used for this purpose, and they differ considerably both in performance and practicability. The use of a paraboloid, which has been given first consideration for the Cloudcroft furnace, does not appear to be an optimum choice. The purpose of this report is to call attention to the range of possible alternatives and to show by example what might be achieved. It would be regrettable indeed if design and construction were to proceed without recognition of these alternatives.

For a specified target size and a specified solid angle from which flux converges toward the target, there is (as shown below) a fundamental upper limit on the amount of flux which can be concentrated onto the target. No optical system, however ideal it may be, can exceed this upper limit. If an optical system receives more than this amount of flux, it cannot deliver all of the received flux onto the specified target area, and it accordingly has two faults: (a) It is bigger than theoretically necessary. (b) It spills the excess flux into a halo around the target where it is not wanted. In these terms, a paraboloidal mirror of the proportions now under consideration for the Cloudcroft furnace (say, 104-foot aperture and 120° cone of convergence) is more than

1.7 times larger than ideally necessary, and it spreads the excess light (44% of the total received) over an area 7 times as large as that of the target. While we know of no practical furnace system exactly meeting the conditions required for ideal performance, we do know of practical systems which excel a paraboloid.

The criteria of an ideal system would be that it have no spherical aberration and no coma — in short, that it meet the Abbe sine condition. This situation is represented by Figure 19, where the sine condition requires, for any particular ray, that

$$h = f \sin \theta.$$

If the angular radius of the sun is taken to be 16 minutes of arc, and if the target radius is r , we have

$$f = 215r.$$

The aperture under these conditions is

$$2h_0 = 430 r \sin \theta_0.$$

If the target diameter is 5 inches ($r = 2.5$), as contemplated for the Cloudcroft furnace, and if the peripheral angle θ_0 is 60° , the aperture turns out to be about 78 feet. This is the maximum aperture of an ideal system for which all of the light can be delivered to a 5-inch target. If there were no reflection or absorption losses, the maximum possible concentration ratio for $\theta_0 = 60^\circ$ would be

$$\frac{\pi h_0^2}{\pi r^2} = (215)^2 \sin^2 (60^\circ) = 34600$$

Any optical system with continuous unobstructed surfaces and free of spherical aberration can produce the same concentration ratio for the same value of θ_0 , but the associated aperture will automatically be greater than $2h_0$ if the sine condition is not also met. One can also arrive at the foregoing conclusions from purely geometrical arguments without invoking the sine condition per se.

The geometrical efficiency of an optical system having continuous unobstructed surfaces and free of spherical aberration will be simply

$$\mathcal{E} = h^2/Y^2$$

where Y is the radius of the aperture. For a paraboloid with $\theta = 60^\circ$ and with a 5-inch paraxial solar image, we find $2Y$ is about 104 feet, yielding:

$$\mathcal{E} = \left(\frac{78}{104}\right)^2 = 56\%.$$

This result can be laboriously verified by dividing the paraboloid (or any other system having the same Y , f , θ) into annular zones, computing the image profile for each zone, finding what fraction of this image actually hits the target, weighting these zonal efficiencies in proportion to the relative areas of the zones, and finally summing the zonal contributions. This procedure was actually carried out for two very different systems, and the results (with suitable allowance for obstructed areas) have checked the conclusions above.

The actual efficiency of a system will be considerably less than the geometrical efficiency discussed above because of losses due to glass absorption, imperfect reflection, obstructed areas, and interstices between the facets that comprise the optical elements. Optimistically assuming two reflections of 0.9 efficiency and other losses totaling 0.1, we find that an actual efficiency of 41% is unlikely to be exceeded by any system with a 104-foot aperture, a 5-inch target, and a 120° cone of convergence ($\theta = 60^\circ$).

Four important conclusions can be summarized:

a. If we are interested in a 5-inch target with $\theta = 60^\circ$, a 104-foot aperture is not necessarily needed. Only 56% of the flux received by a 104-foot aperture can be geometrically utilized. A somewhat smaller aperture (theoretical minimum = 78 feet) can achieve equal performance if a suitable and practical optical system can be found. We do not need to belabor this possibility - its importance is appreciated when one recalls that costs of large constructions vary roughly as the cube of the aperture. Or, turning the argument around, we can say that a 104-foot aperture should be capable of performing efficiently on a target larger than 5 inches (theoretical maximum = 6.6 inches).

b. We noted that all 104-foot optical systems with continuous unobstructed surfaces and with no spherical aberration will put 56% of their unabsorbed or unobstructed flux onto a 5-inch target if $\theta = 60^\circ$.

They are all basically equal in that respect. They differ considerably, however, in where the 44% spillage goes. A 104-foot paraboloid spreads this spillage over a 13-inch disc, whereas an alternative system discussed in Section III confines nearly all of the spillage to an 8-inch disc. In the latter case, the spillage lies close enough to the 5-inch central disc to be of frequent practical use.

c. It is possible to design optical systems which not only are superior to the paraboloid with respect to a and b above, but which in addition possess certain advantages with respect to simplicity of optical fabrication and convenience of adjustment. For example, the cases discussed in Section III employ surfaces which are either spherical or nearly spherical over most of their area.

d. A substantial gain in concentration ratio is potentially available by allowing θ to exceed 60° . Since the concentration ratio varies as $\sin^2 \theta$, one can theoretically gain a factor of 1.18 by making $\theta = 70^\circ$, a factor of 1.29 by making $\theta = 80^\circ$, or a factor of 1.33 by making $\theta = 90^\circ$ (which is the absolute limit for a flat target). However, values of θ beyond 70° are probably not optically practical. At $\theta = 70^\circ$, the maximum attainable concentration ratio (neglecting losses) is 40700, and the associate aplanatic aperture $2h_0$ is 84 feet if a 5-inch target is used.

The remainder of this report is divided into four parts. Section

II concerns the characteristics of a paraboloidal mirror, Section III explores what might be achieved with a two-mirror system consisting of a large primary and a small secondary, Section IV discusses a structural design suited to the type of optical system presented in Section III, and Section V presents an alternate arrangement for using a paraboloid with a heliostat. The structural designs, prepared with the excellent artistic collaboration of Mr. Roger Hayward, appear to possess certain practical advantages over the proposed heliostat-paraboloid combination.

It should be emphasized that the present report does not pretend to be a complete survey of the optical or structural possibilities. Its primary purpose has been to show that the various possibilities of devising a solar furnace are not yet exhausted.

II. Characteristics of a Paraboloid

Figure 20 is the axial section through a paraboloid of rotation with various pertinent quantities labeled. In rectangular coordinates the equation for this section is simply:

$$Y^2 = 2RX,$$

where the origin is at the vertex V of the paraboloid, and where R is its radius of curvature in that neighborhood. The distance from the vertex to the focus is $R/2$. In polar coordinates the equation of the paraboloid is

$$\rho = \frac{R}{1 + \cos \theta},$$

where the pole is at the focus. The normal to the surface at P makes an angle $\theta/2$ with the axis, and the radius of curvature at P is given by

$$R \left(\frac{2}{1 + \cos \theta} \right)^{3/2}$$

in the meridional plane, and by

$$R \left(\frac{2}{1 + \cos \theta} \right)^{1/2}$$

in the sagittal plane. A pencil of rays parallel to the axis and incident at P is brought to an anastigmatic focus at F , so that the effective focal length in both the meridional plane and the sagittal plane is simply ρ . If a target surface is placed normal to the axis at F , the sagittal half-width of the solar image produced by a single facet at P is the product of ρ and the sun's angular radius:

$$b = 0.004654 \rho = \frac{0.004654 R}{1 + \cos \theta},$$

and the projected meridional half-width of the image is

$$a = b \sec \theta.$$

For paraxial rays, $a = b = 0.002327 R$. If the target is made to coincide with this paraxial image, the optical efficiency of any annular zone at angle θ is accordingly

$$\epsilon = \frac{(0.002327)^2 R^2}{a b} = 0.25 (1 + \cos \theta)^2 \cos \theta.$$

The fraction of the aperture area contained within a narrow zone of width ΔY is

$$\Delta A = \frac{2Y\Delta Y}{Y_1^2} = 2\left(\frac{R}{Y_1}\right)^2 \frac{\sin \theta \Delta \theta}{(1 + \cos \theta)^2},$$

where Y_1 is the radius of the full aperture. The overall efficiency of the system is therefore

$$E = \int_0^{\theta_1} \mathcal{E} dA = 0.5 \left(\frac{R}{Y_1}\right)^2 \int_0^{\theta_1} \sin \theta \cos \theta d\theta,$$

which yields

$$E = 0.25 (1 + \cos \theta_1)^2.$$

For a 104-foot paraboloid with a 5-inch paraxial image, we have $Y_1 = 52$ feet, $R = 89.5$ feet, $\theta = 60^\circ$, and we obtain $E = 56\%$. This is in agreement (as we should expect) with the result derived from the Abbe sine condition in Section I.

The 44% spillage of a paraboloid having $\theta = 60^\circ$ is spread over a disc 13.3 inches in diameter, or an area of 140 square inches. The distribution of this spill light can be computed by finding what fractions of the elliptical solar images ($2a$ long and $2b$ wide) formed by facets at various values of θ fall inside concentric circles of various diameters between 5 inches and 13.3 inches at the focal plane. When the elliptical image falls entirely inside a circle of radius r , the efficiency for the associated zone and for this value of r is 100%. When the circle

lies entirely inside the elliptical image, the zonal efficiency is r^2/ab .

When the circle intersects the ellipse, as sketched in Figure 3, the efficiency is $S/\pi ab$, where S is the area which the circle and the ellipse have in common. If $\alpha = a/r$ and $\beta = b/r$, it can be shown that the area in common is

$$S = \pi + 2\alpha\beta \arcsin\left(\frac{1-\beta^2}{\alpha^2+\beta^2}\right)^{1/2} - 2 \arcsin\left[\alpha\left(\frac{1-\beta^2}{\alpha^2+\beta^2}\right)^{1/2}\right].$$

This expression is rather complex for practical computation, and the following approximation is more expedient:

$$\mathcal{E} \approx \frac{r^2}{ab} \left\{ 1 - \left[\frac{(r-b)^3}{r^2(r-br^2/a^2)} \right]^{1/2} \right\}$$

When $b \rightarrow r$, $e \rightarrow r/a$; and when $a \rightarrow r$, $e \rightarrow 1$.

Sample results are listed in Table VII and plotted in Figure 24.

These data were assembled primarily for comparison with similar results for another system discussed in Section III.

III. Two-Mirror Systems

When only one mirror participates in the focusing, it must necessarily be a paraboloid, unless the mirror surface is a discontinuous curve. In general, discontinuous curves result in the utilization of less solid angle for the same peripheral θ and Y , and they consequently offer no gain over continuous curves.

When more than one mirror participates in the focusing, an infinite number of combinations become possible, and specific cases must be selected for investigation. Several combinations involving a large primary mirror and a small secondary mirror were investigated in varying degrees of detail. A particularly interesting case, diagrammed in Figure 22, provides a suitable example for discussion in the present report. A blend of this case with another one will also be discussed to show how the good features of two systems might be combined. It must be remembered that these cases are merely examples with arbitrarily chosen parameters, and that they do not represent optimum choices. Much additional computing and comparing would be required to afford a basis for the selection of an optimum case.

In Figure 22 the primary mirror, which includes about 90% of the total mirror area of the system, is a sphere of radius R. Such a choice would clearly be convenient both for construction and for adjustment. Except for the inner zone hidden by the secondary, the facets of the spherical primary can be adjusted very simply by autocollimation, using a small light source at the center of curvature C.

The secondary mirror, which amounts to about 10% of the total mirror area, serves to correct the spherical aberration of the primary. It is roughly paraboloidal in form and its facets can be adjusted with adequate precision by means of a template.

Strangely, the spherical aberration of the primary mirror serves a useful purpose. It prevents the effective focal length of the combination from increasing with θ , and it thereby keeps the solar image small for the outer zones of the system. It is especially effective in the meridional plane, where it also compensates for the $\sec \theta$ factor due to the oblique incidence of the zonal images on the target. As a consequence, the outer zones of the system are the most efficient ones, and the spillage around the target is confined to a much smaller disc than in the case of the paraboloid.

The exact shape of the secondary mirror can be derived by imposing the condition that optical path lengths must be the same for all rays that come to a focus at the center of the target. For any value of ϕ , the path is

$$L_{\phi} = \underbrace{-R \left(1 - \cos \frac{\phi}{2}\right)}_{\text{to Q}} + \underbrace{\frac{R}{2} \sec \frac{\phi}{2}}_{\text{to H}} + \underbrace{(x+p) \sec \phi}_{\text{to P}} + \underbrace{\left[(x-d+c)^2 + (x+p)^2 \tan^2 \phi \right]^{1/2}}_{\text{to G}}$$

where the spherical aberration of the primary is

$$p = \frac{R}{2} \left(\sec \frac{\phi}{2} - 1 \right).$$

For paraxial rays, $\phi \rightarrow 0$ and

$$L_0 = \frac{R}{2} + d + c.$$

Setting $L\phi = L_0$, we obtain

$$X = \frac{A^2 - p^2 \tan^2 \phi - (c-d)^2}{2(c-d) + 2A \sec \phi + 2p \tan^2 \phi},$$

where $A = c + d + p(2 \cos \frac{\phi}{2} - 1 - \sec \phi)$.

It follows that

$$y = (x + p) \tan \phi,$$

and the final angle of convergence is

$$\theta = \arctan \left(\frac{y}{x + c - d} \right).$$

In terms of R and ϕ , the coordinates of the primary sphere with the origin at the vertex are

$$X = R \left(1 - \cos \frac{\phi}{2} \right); \quad Y = R \sec \frac{\phi}{2}.$$

The solar image formed by a facet of the primary mirror at Q is strongly astigmatic, the meridional image falling at K and the sagittal image at H , but the secondary mirror puts these component images back together again at F . The magnification of the secondary mirror is therefore different for the two axes of the solar image, and (as remarked earlier) it has the desirable feature of decreasing with increasing ϕ and θ . For any particular P and Q , the final solar image formed on a plane normal to the optic axis at F is an ellipse similar to that formed by a facet of a paraboloid, except that its meridional dimension is now the smaller axis instead of the larger axis of the ellipse. To

compute the dimensions of the image ellipses associated with the various zones of the system, one must make use of the following expressions for the pertinent segments of the light path:

$$(QH) = 0.5 R \sec \frac{\phi}{2},$$

$$(QK) = 0.5 R \sec \frac{\phi}{2} - 0.5 Y \tan \frac{\phi}{2},$$

$$(HP) = y \csc \phi,$$

$$(KP) = y \csc \phi + 0.5 Y \tan \frac{\phi}{2},$$

$$(GP) = y \csc \theta.$$

On a plane normal to the optic axis at F , the meridional half-width of the image (semi-minor axis) is

$$a = 0.004654 (QK) \left(\frac{GP}{KF} \right) \sec \theta,$$

and the sagittal half-width of the image (semi-major axis) is

$$b = 0.004654 (QH) \left(\frac{GP}{HP} \right).$$

Some sample data for an optical system of this type are listed in Table VIII. For this case we adopted $c = 0.21R$ and $d = 0.10R$, and the system has been scaled to a 100-foot aperture for a peripheral ϕ of 65° , which yields a peripheral θ of approximately 60° and a value of 93 feet for R .

The spread of the spill light surrounding the target can be reduced still further by blending the outer zones of the sphere-corrector combination in Figure 22 with the inner zones of a system consisting of

a paraboloidal primary and an ellipsoidal secondary. This blended system is sketched in Figure 23. The transition was arbitrarily chosen to occur at $\phi = 50^\circ$ and the slope was made continuous across the transition so that neither the primary nor the secondary would have any optical discontinuity. It can be shown that the paraboloidal portion of the primary is

$$Y^2 = 2(R - X_0)(X + \Delta),$$

where X_0 is the coordinate of the junction (0.09369 R) and where $\Delta = 0.00484 R$. The ellipsoid is given by

$$\frac{(x + 0.08085 R)^2}{(0.17601 R)^2} + \frac{y^2}{(0.17357 R)^2} = 1.$$

Its eccentricity is found to be 0.1657. For $\phi < 50^\circ$, all rays from the primary pass through the same axial intercept E, and the magnification of the secondary is found to be

$$m = 1.0564 + 0.3406 \cos \phi.$$

The final images formed on a plane normal to the axis at F have sagittal half-widths of

$$b = 0.004654 (QE) m$$

and meridional half-widths of

$$a = b \sec \theta,$$

where the angle of convergence θ is given by

$$\theta = \arcsin \left[\frac{1}{m} \sin \phi \right],$$

The distribution of the spill light for this blended optical system of Figure 23 has been calculated as it was for the paraboloid. Both distributions are plotted in Figure 24 for comparison.

IV. Mounting for a Two-Mirror System

Figure 25 shows how the two-mirror optical system, described above, may be embodied with an alt-azimuth mounting. Such a mounting has a precedent in large construction — it has been used for the Manchester radio telescope of 250-foot aperture. The separate angular motions of altitude and azimuth may be controlled and coordinated by separate sun trackers with associated servomechanisms or by programmed drives.

This alt-azimuth mounting has several notable features:

- a. Relative immunity to high winds.
- b. Protection of optical parts from weather.
- c. Facility for optical adjustment.
- d. Target plane faces upward.
- e. Primary movable to a "horizontal" position for maintenance and repair.

Figure 25 illustrates the general appearance of the envisioned furnace, while Figure 26 shows three sectional views of the furnace. The main structure turns in azimuth on a circular track, and this frame

supports the furnace proper on trunnions that allow it to rotate in altitude.

This construction provides the observing station that is detailed in Figure 25 and shown further in Figure 26. Observation directly into the furnace hot spot is afforded from this station. Observers may work on its cylindrical half-floor when the furnace is tipped, and on the level half-floor when the furnace is pointing vertically. Experience of astronomers with the prime-focus cage of the 200-inch Palomar telescope serves as precedent to show that such an observing system is practical. Figure 26 shows how the observer enters the observing station by an elevator to the trunnion level, and thence by steps.

At the hot spot, when a crucible is exposed, it will be inclined upward by at least 30° and it will be nearly vertical at high noon in early summer. A prearranged set-up for an experiment or for routine exposure may be raised to trunnion level by the elevator indicated. From there it goes horizontally across the cat-walk to a door in the central shaft and thence to the hot spot by a lift. This cat-walk may be turned, during exposure, to a position affording minimum obstruction (as shown in Figure 26, upper right).

The artist has shown an ensemble of sloped radial vanes to serve (1) as an attenuator; (2) as the slow shutter; and (3) as a protecting

roof. The vanes are mounted so that they turn open over the beams that support the observing station, thereby minimizing light obstruction.

A similar but smaller ensemble of vanes (not shown) could conveniently be located radially (to form an inward pointing cone) and reach from the rim of the secondary mirror to the central shaft. Such a secondary set of vanes could serve as the fast shutter.

For adjusting the facets of the primary mirror, and aligning the primary with the secondary, we envision the furnace pointed toward a platform on a nearby tower. By bringing the center of curvature of the spherical part of the primary within surveillance of an observer there, the spherical facets can be adjusted by autocollimation, as remarked in Section III.

The facets of the aspheric secondary mirror may be adjusted with a radial template arm (not shown) which is perpendicular to the optical axis and rotatable around it.

If the central part of the primary mirror is paraboloidal, as discussed in the latter part of Section III, it may be lined-up simply by putting a point light source at the focus after preliminary adjustment of the secondary mirror. The parabolic facets may be observed by means of penta-prisms mounted, one for each zone of facets, on the template arm mentioned above.

Optical line-up may be carried out during cloudy weather or at night.

Finally, it is to be noted that this furnace construction is compact, and that it may be located in a depression of terrain to further protect it from winds during operation and from damage during storms. This mounting is certainly more immune to wind than one that has separated components separately mounted.

V. Alternative System Using a Paraboloidal Mirror

Figures 27 and 28 show Mr. Hayward's conception of an arrangement using a "horizontal" rather than the previously proposed "vertical" heliostat. This arrangement has the disadvantage of requiring a larger flat mirror; but the following advantages inhere in it:

- a. The working focal plane faces upward.
- b. By means of bi-parting shutters and a retractable shed, all optical parts may be protected from wind and weather.

In this arrangement we propose using the bi-parting shutter as attenuator, with a rotating half-hemisphere for the fast shutter. Access to the hot spot chamber by a passage in one of these bi-parting shutters provides for the safety of personnel.

TABLE VII

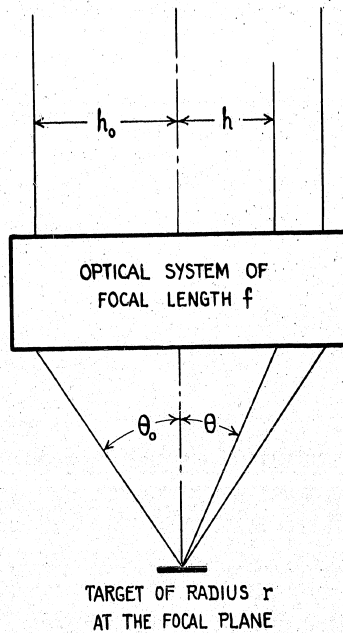
Zonal efficiencies and the distribution of spill light surrounding the target of a paraboloid. Aperture = 2Y₁ = 100 feet, peripheral $\theta = 60^\circ$, paraxial image = 4.84 inches.

Zone No.	1	2	3	4	5	6	7	8	9	10	% flux inside r
Inner Y (ft)	6.00	16.91	23.15	28.03	32.18	35.86	39.20	42.26	45.12	47.81	
Outer Y (ft)	16.91	23.15	28.03	32.18	35.86	39.20	42.26	45.12	47.81	50.36	
Mean θ	15°9'	26°2'	32°53'	38°20'	42°50'	46°45'	50°25'	53°32'	56°24'	59°5'	
a (inches)	2.549	2.836	3.131	3.455	3.808	4.200	4.631	5.106	5.630	6.220	
b (inches)	2.460	2.548	2.629	2.710	2.791	2.873	2.953	3.034	3.114	3.194	
	0.988	0.865	0.759	0.667	0.588	0.518	0.457	0.403	0.356	0.314	59.1
	1.000	1.000	0.986	0.910	0.826	0.737	0.656	0.581	0.513	0.452	76.6
	1.000	1.000	1.000	1.000	0.985	0.922	0.848	0.767	0.692	0.623	88.4
	1.000	1.000	1.000	1.000	1.000	1.000	0.975	0.905	0.834	0.757	94.7
	1.000	1.000	1.000	1.000	1.000	1.000	1.000	0.987	0.937	0.871	98.0
	1.000	1.000	1.000	1.000	1.000	1.000	1.000	1.000	1.000	0.994	99.9
for various r											

TABLE VIII

Sample two-mirror system having an all-spherical primary.
 $c = 0.21 R$, $d = 0.1 R$, aperture = 100 feet, $R = 93$ feet.

ϕ	20.0	27.5	35.0	42.5	50.0	57.5	65.0	deg.
P	0.72	1.37	2.26	3.39	4.81	6.54	8.64	feet
X	1.41	2.67	4.30	6.32	8.71	11.47	14.56	"
Y	16.15	22.10	27.96	33.70	39.30	44.73	50.00	"
x	8.82	8.25	7.49	6.24	4.44	1.92	-1.44	"
y	3.47	5.01	6.82	8.86	11.02	13.28	15.42	"
θ	10.330	15.181	21.060	28.266	36.915	47.543	60.326	deg.
(QH)	47.22	47.87	48.76	49.89	51.31	53.04	55.13	feet
(QK)	45.79	45.26	44.35	43.34	42.14	40.77	39.22	"
(HF)	10.16	10.85	11.89	13.07	14.39	15.75	17.01	"
(KF)	11.58	13.56	16.30	19.62	23.55	28.02	32.93	"
(GP)	19.37	19.15	18.98	18.70	18.35	18.00	17.75	"
2a	8.70	7.38	6.18	5.24	4.59	4.33	4.77	inches
2b	10.06	9.44	8.69	7.98	7.31	6.77	6.42	"
ϵ (5 in.)	28.5	35.8	46.5	59.8	72.7	79.6	80.5	%



ABBE'S SINE CONDITION: $h = f \sin \theta$

FIGURE 19

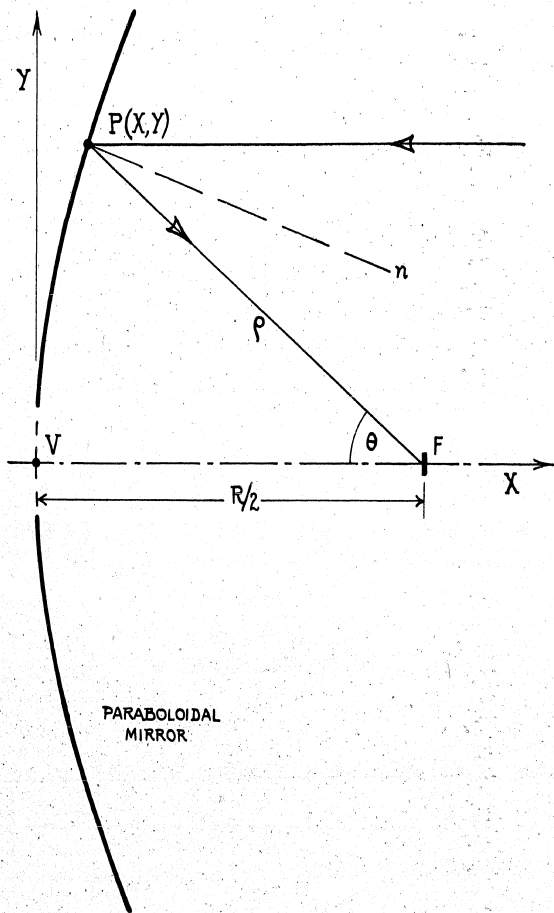
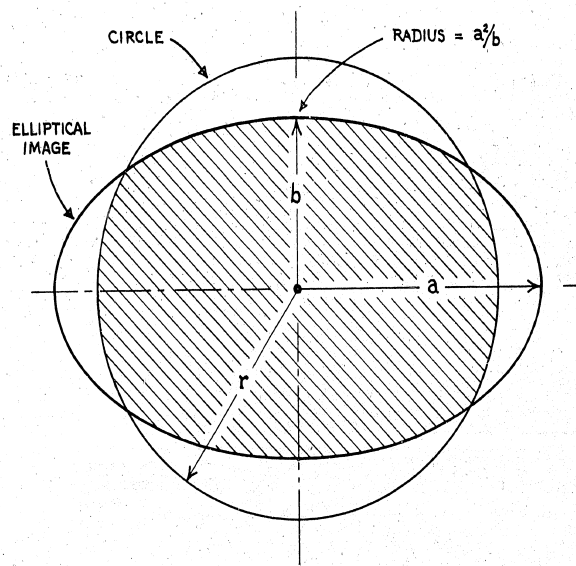


FIGURE 20



AREA COMMON TO CIRCLE AND ELLIPSE = S =



FIGURE 21

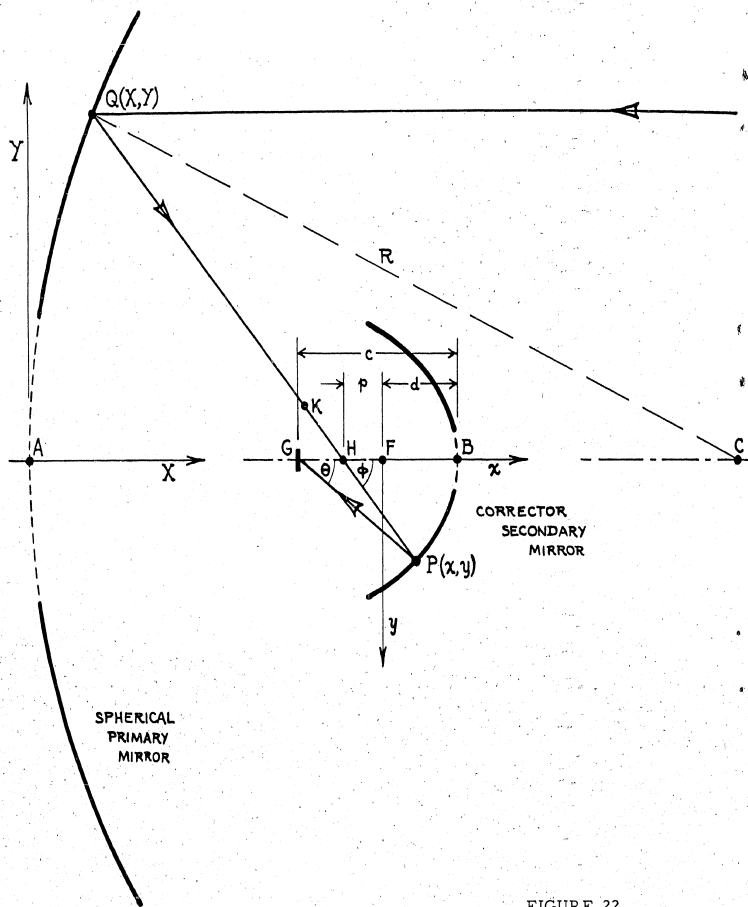


FIGURE 22

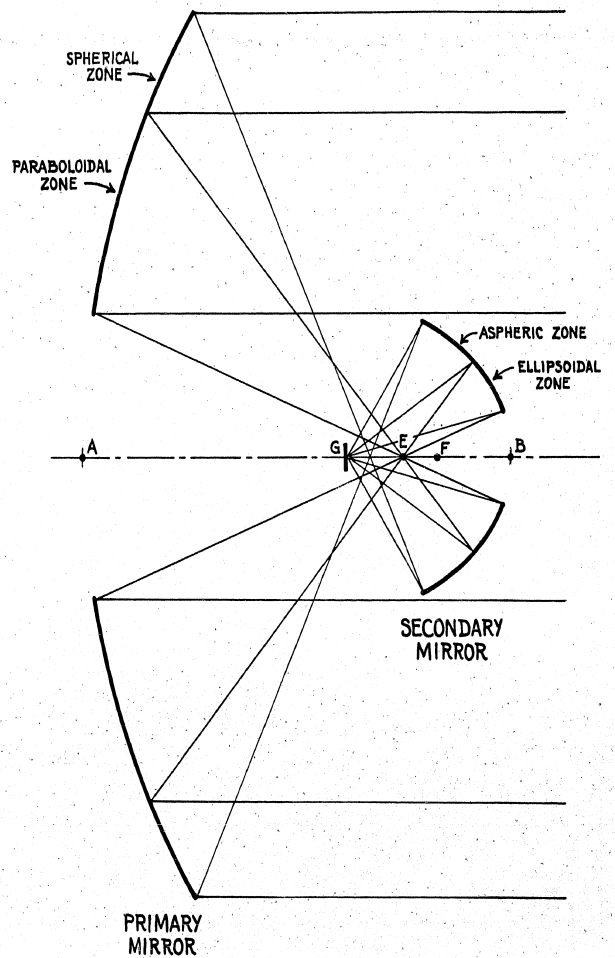


FIGURE 23

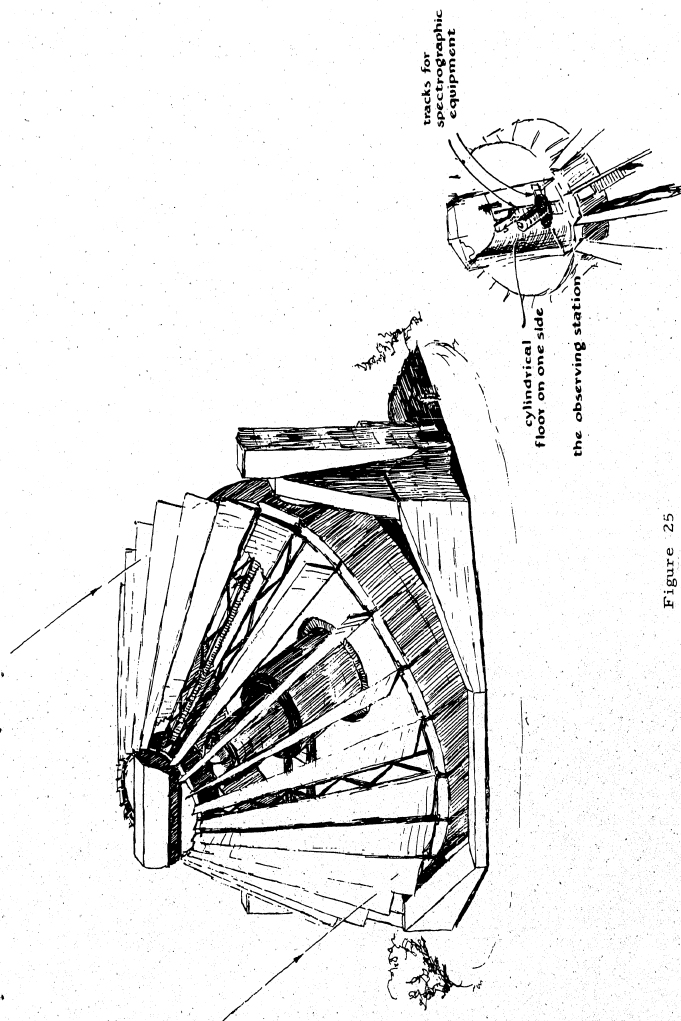
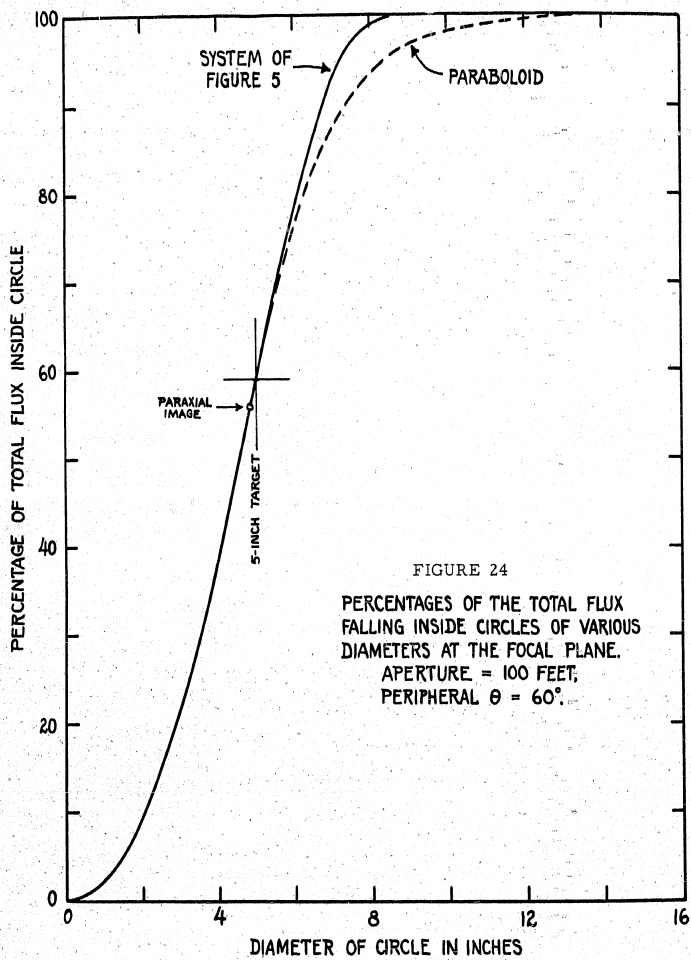


Figure 25

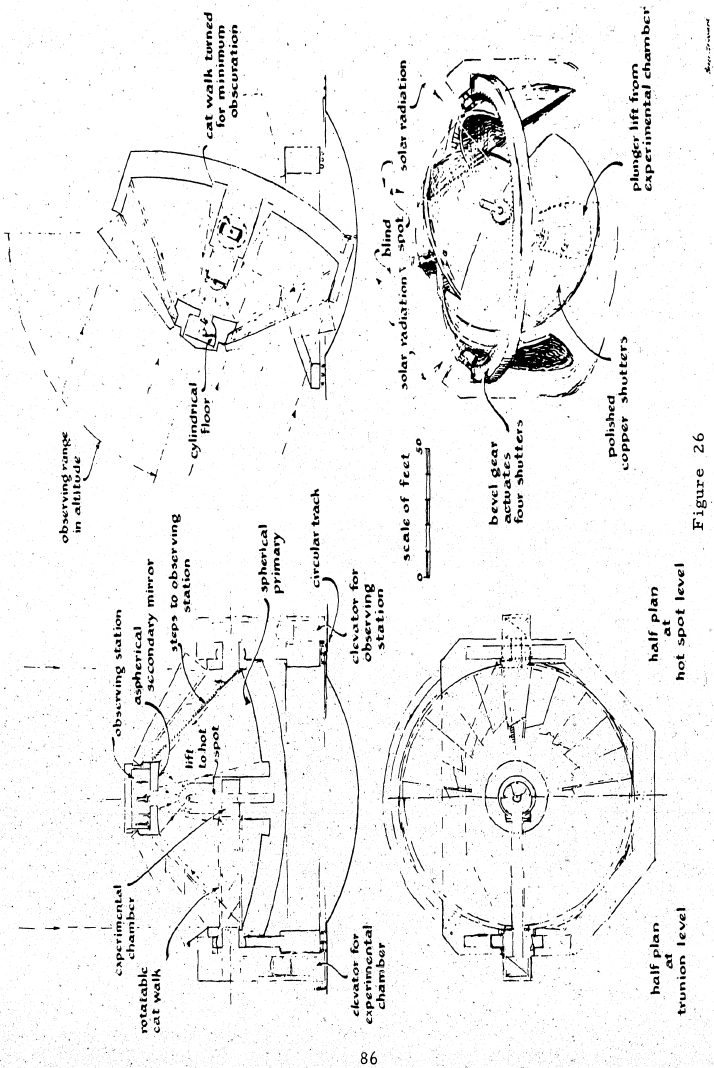


Figure 26

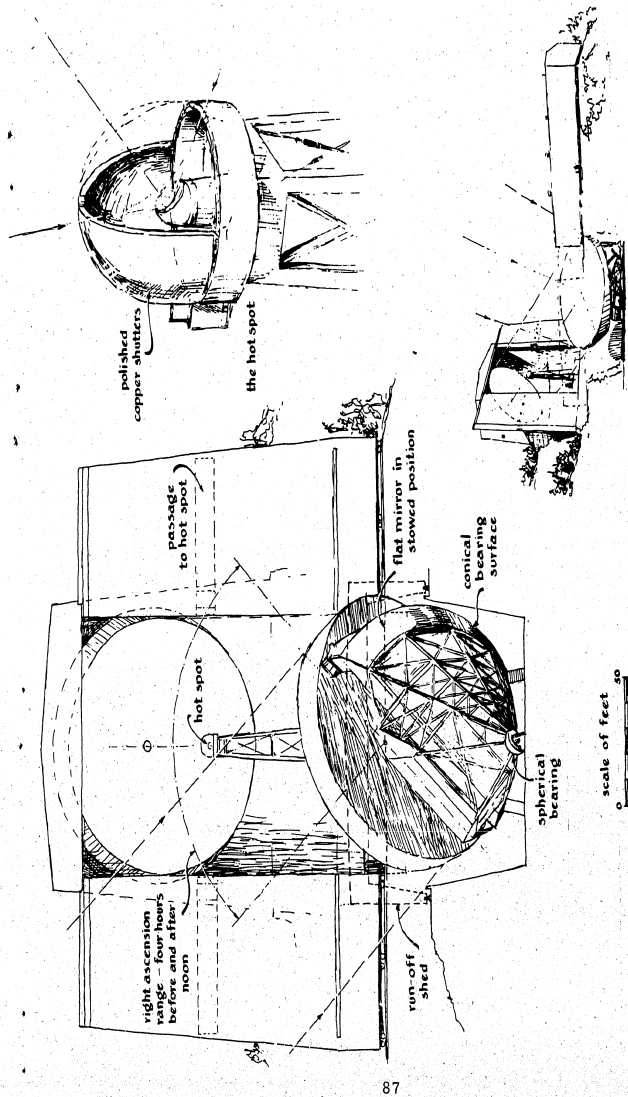


Figure 27

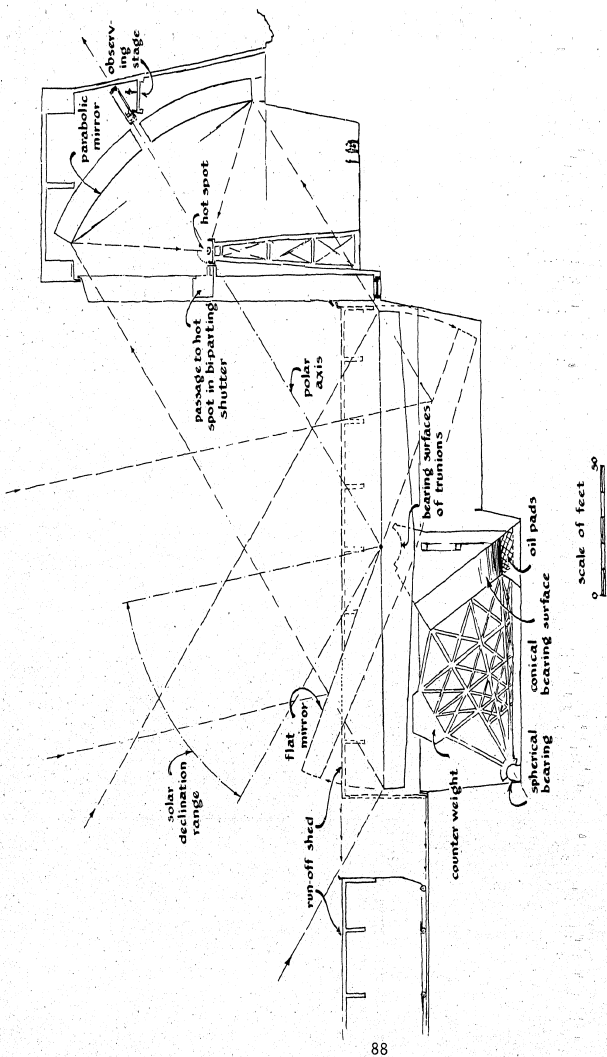


Figure 28

CHAPTER 5

THE LOSS OF ENERGY BY ABSORPTION AND REFLECTION IN THE HELIOSTAT AND PARABOLIC CONDENSER OF A SOLAR FURNACE



ABSTRACT

This chapter analyses the reflection and absorption losses for back silvered plate glass mirrors such as would be used in a solar furnace. Taken into account are: the amount of incident light reflected from the surface of the glass plate, the amount absorbed by the known thickness of the glass plate, the amount lost on reflection from the silver surface, and the higher order terms showing the losses as the light is reflected and transmitted back and forth within the glass.

I. The Method

If we denote by r the fraction of the intensity of the incident light which is reflected from the front surface of a mirror, by a the fraction of the intensity of the incident light which is refracted by the glass, by ρ the fraction of the intensity of the light incident on the silver surface which is reflected therefrom, by r' the fraction of the light incident internally on the glass surface reflected therefrom, by a' the fraction of the light incident internally on the glass surface refracted into the air, and by R the sum of the fractional intensities reflected by the combination, we see from Figure 29 that

$$R = r + \rho a a' + r' \rho a \rho a' + r' r' \rho a \rho \rho a' + \dots \quad (1)$$

Now we have the relation $a = (1 - r)$, and it can easily be shown that $r' = r$ and $a' = a$ so that we can put

$$R = r + \rho(1-r)^2 [1 + r\rho + (r\rho)^2 + \dots] \quad (2)$$

If now we use the subscripts \parallel and \perp to indicate the parallel and perpendicular components of the light, we have according to Fresnel

$$r_{\parallel} = \left[\frac{\tan(\phi - \chi)}{\tan(\phi + \chi)} \right]^2 \quad (3)$$

and

$$r_{\perp} = \left[\frac{\sin(\phi - \chi)}{\sin(\phi + \chi)} \right]^2, \quad (4)$$

where ϕ is the angle of incidence and χ the angle of refraction; we additionally note that

$$\sin \chi = (\sin \phi) / N \quad (5)$$

where N is the index of refraction of the glass, from which the angle of refraction can be calculated provided that the angle of incidence is given.

For the quantities ρ_p and ρ_s we have the relations

$$\rho_p = \frac{(\eta - N/\cos \phi)^2 + \kappa^2}{(\eta + N/\cos \phi)^2 + \kappa^2} \quad (6)$$

and

$$\rho_s = \frac{(\eta - N \cos \phi)^2 + \kappa^2}{(\eta + N \cos \phi)^2 + \kappa^2} \quad (7)$$

where η is the index of refraction of the silver and κ the extinction coefficient, and from these equations R_p and R_s can be calculated.

Assuming the incident light unpolarized, the resultant R is given by

$$R = (R_p + R_s) / 2 \quad (8)$$

II. Calculation of the Reflectivity of a Glass - Silver Mirror

Let I indicate the incident intensity of the light falling on the mirror, E the emergent intensity, μ the absorption coefficient of the glass and t the thickness of the glass, then upon referring to Figure 30 we have the following equations -

$$\begin{aligned} I &= I_0 \varepsilon^{-\mu t / \cos \chi} \\ I_1 &= \rho I \varepsilon^{-\mu t / \cos \chi} \\ I_2 &= r' I_1 \varepsilon^{-\mu t / \cos \chi} \\ I_3 &= \rho I_2 \varepsilon^{-\mu t / \cos \chi} \\ I_4 &= r' I_3 \varepsilon^{-\mu t / \cos \chi} \\ I_5 &= \rho I_4 \varepsilon^{-\mu t / \cos \chi} \end{aligned} \quad (9)$$

and so on

$$\begin{aligned} E &= r I_0 \\ E_1 &= r' I_1 \\ E_3 &= r' I_3 \\ E_5 &= r' I_5 \end{aligned} \quad (10)$$

and so on.

Substituting $(1-r)$ for A and A' and r for r' , we have as the sum of the emergent intensities

$$R = \sum E/I_0 = r + (1-r)^2 \rho \epsilon^{-2\alpha} + (1-r)^2 r \rho^2 \epsilon^{-4\alpha} + (1-r)^2 r^2 \rho^3 \epsilon^{-6\alpha} + \dots$$

$$= r + (1-r)^2 \rho \left[\epsilon^{-2\alpha} + r \rho \epsilon^{-4\alpha} + r^2 \rho^2 \epsilon^{-6\alpha} + \dots \right] \quad (11)$$

where we have put

$$\epsilon^{-2\alpha} = \epsilon^{-2\mu t / \cos \chi} \quad (12)$$

If we let $f = \epsilon^{-\alpha}$ we can further write

$$R = r + (1-r)^2 \rho^2 [1 + r \rho f^2 + r^2 \rho^2 f^4 + \dots] \quad (13)$$

The quantities r , ρ and f are functions of the angle of incidence as well as of the wave length.

It remains to show how f_0 , the fractional part of the light incident on a plate of glass which is absorbed by a known thickness t_0 of the glass, can be determined from the measured fraction p of the light transmitted by the glass. This transmitted portion p is given by

$$p = (1-r)^2 \epsilon^{-\alpha_0} + r^2 (1-r)^2 \epsilon^{-3\alpha_0} + r^4 (1-r)^2 \epsilon^{-5\alpha_0} + \dots \quad (14)$$

Since r is approximately 4%, we can write to a close degree of approximation

$$p = (1-r)^2 \epsilon^{-\alpha_0} = (1-r)^2 f_0 \quad (15)$$

whence

$$f_0 = p / (1-r)^2 \quad (16)$$

In order to calculate f we note

$$f = \epsilon^{-\mu t} \quad f_0 = \epsilon^{-\mu t_0} \quad t = t_0 / \cos \chi$$

whence we have

$$\log_{10} f = (\log_{10} f_0) / \cos \chi \quad (17)$$

III. Calculations

In a previous report⁽¹⁾ we have calculated the energies contained in various wave length bands in the spectrum of the sun. We shall use the same bands in this report. In Table IX the quantities η , K , N and K^2 are given for the glass and the silver coating. The index of refraction of water white plate glass as a function of wave length was not available; however, the Pittsburgh Plate Glass Company has advised it would be approximately the same as for crown-silicate glass. The

values for this glass are given by Morey⁽²⁾. The values of n and K were extrapolated from the data given in the Smithsonian Tables⁽³⁾.

From Eqs. (3), (4), (5), and (8), the values of \mathcal{R} corresponding to various angles of incidence and wave lengths were calculated and are given in Table X.

Next, from Eqs. (6), (7), and (8), the values of ρ were calculated for various angles and wave length bands and are given in Table XI.

From a table given by Wight⁽⁴⁾ for the transmission of water white plate glass, the factors t_0 were calculated. The data were extrapolated beyond 2.10μ and are given in Table XII.

From the values given in Table XII, the values of \mathcal{F} were calculated for various angles according to Eq. (17). The results are given in Table XIII.

From the values of n , ρ and \mathcal{F} given in the tables, the values of R for an angle of incidence of 40° , corresponding to an angle of elevation of the sun of 80° , and for the energy in the various bands as given in a previous report⁽¹⁾, the energy reflected from the heliostat was calculated, and the results are given in Table XIV.

One notes that the energy reflected by the heliostat is 89.8% of the energy falling on it when the angle of elevation of the sun is 80° .

Next the values of R corresponding to various wave lengths and angles ϕ were calculated. The results are given in Table XV. Only the first two terms of Eq. (13) were used.

Taking the values of $E(\theta)$ given in a previous report⁽¹⁾ for various angles θ and multiplying these values by the corresponding values of $\phi = \theta/2$ and integrating the energies corresponding to various wave lengths and angles θ of 50° , 60° and 70° , the partial fluxes were calculated and are given in Table XVI for an angle of elevation of the sun of 80° .

On the basis of $R = 1$, i. e., unit reflectivity, we obtained the following values for the energy⁽¹⁾,

50°	60°	70°
53,970	69,645	83,178 cal/cm ² per min.

giving for the combined reflectivities of the heliostat and paraboloid

50°	60°	70°
81.3%	81.3%	81.5%

while we note for the heliostat alone the reflectivities

50°	60°	70°
89.8%	89.8%	89.8%

leaving as the reflectivities of the paraboloid

50°	60°	70°
90.5%	90.5%	90.8%

On the basis of 1.76 cal/cm²/min incident solar radiation, these would correspond to energy concentrations of

	50°	60°	70°
	731	944	1130
cal/cm ² /second.			

Table IX.

λ	n	K	K^2	N
.425	.16	2.20	4.84	1.537
.625	.17	4.05	16.41	1.522
.875	.205	6.06	36.73	1.514
1.25	.345	8.83	77.99	1.510
1.75	.557	12.3	151.3	1.505
2.25	.77	15.4	237.2	1.498
2.75	1.36	18.5	342.3	1.490
3.75	2.93	26.3	691.9	1.450

Table X.

ϕ	λ							
	.425	.625	.875	1.25	1.75	2.25	2.75	3.75
0°	.0438	.0429	.0418	.0413	.0406	.0397	.0396	.0337
5°	.0440	.0428	.0420	.0408	.0408	.0400	.0392	.0336
10°	.0446	.0426	.0414	.0410	.0404	.0395	.0387	.0337
15°	.0448	.0425	.0419	.0411	.0405	.0395	.0386	.0339
20°	.0449	.0431	.0422	.0414	.0406	.0400	.0389	.0340
25°	.0455	.0434	.0421	.0419	.0415	.0401	.0395	.0342
30°	.0464	.0445	.0434	.0427	.0423	.0412	.0406	.0356
35°	.0478	.0458	.0448	.0443	.0436	.0427	.0417	.0366
40°	.0500	.0487	.0477	.0469	.0463	.0444	.0443	.0392

Table XI.

ϕ	λ							
	.425	.625	.875	1.25	1.75	2.25	2.75	3.75
0°	.873	.946	.969	.975	.978	.981	.977	.980
5°	.873	.946	.968	.974	.979	.981	.977	.978
10°	.873	.946	.969	.973	.979	.981	.977	.977
15°	.873	.947	.968	.974	.979	.981	.978	.977
20°	.873	.947	.968	.974	.978	.981	.978	.977
25°	.873	.946	.968	.974	.979	.981	.977	.977
30°	.873	.947	.968	.974	.978	.981	.977	.975
35°	.874	.947	.968	.974	.978	.981	.977	.975
40°	.875	.946	.967	.973	.978	.980	.978	.976

Table XII.

λ	f_0
.425	.991
.625	.997
.875	.991
1.250	.980
1.750	.927
2.250	.912
2.750	.911
3.750	.901

Table XIII.

ϕ°	.425	.625	.875	λ	1.25	1.75	2.25	2.75	3.75
0	.991	.997	.991	.980	.927	.912	.911	.910	.901
5	.991	.997	.991	.980	.927	.912	.911	.910	.901
10	.991	.997	.991	.980	.927	.911	.910	.910	.901
15	.991	.997	.991	.980	.926	.911	.910	.910	.901
20	.991	.997	.991	.980	.925	.910	.909	.909	.898
25	.991	.997	.991	.979	.924	.908	.907	.897	.897
30	.991	.997	.991	.979	.923	.907	.906	.895	.895
35	.990	.997	.991	.978	.921	.905	.904	.893	.893
40	.990	.997	.991	.978	.920	.903	.902	.890	.890

Table XIV (The heliostat)
Angle of elevation of the sun = 80°

λ	R	ℓ	$R\ell$
.425	.857	.44	.377
.625	.939	.48	.451
.875	.948	.28	.265
1.250	.929	.32	.297
1.750	.827	.14	.116
2.250	.756	.04	.030
2.750	.752	.03	.023
3.750	.735	.03	.022
Sum		1.76	1.58

cal/cm² per min.

Table XV.

λ	5°	10°	15°	ϕ	20°	25°	30°	35°	40°
.425	.854	.857	.857	.857	.857	.857	.858	.856	.857
.625	.939	.939	.940	.940	.939	.940	.940	.939	.939
.875	.950	.949	.950	.949	.950	.949	.949	.950	.948
1.25	.934	.933	.932	.934	.932	.933	.933	.930	.929
1.75	.841	.841	.840	.837	.837	.837	.833	.830	.827
2.25	.817	.815	.815	.813	.809	.809	.806	.804	.756
2.75	.812	.809	.810	.808	.805	.805	.805	.799	.752
3.75	.795	.794	.794	.789	.787	.783	.780	.735	

Table XVI.

λ	50°	60°	70°
.425	10,592	13,642	16,302
.625	13,482	17,452	20,872
.875	7,350	9,510	11,427
1.25	7,990	10,290	12,260
1.75	2,761	3,558	4,319
2.25	699	900	1,072
2.75	516	665	792
3.75	494	636	751
Sum	43,884	56,653	67,801

cal/cm²/min.

References

- (1) Alfred W. Simon, "Calculations of the Concentration of the Solar Radiation through the Focal Spot of a Parabolic Mirror," Technical Memorandum No. HDGR-57-10, Holloman Air Development Center, 15 August 1957.
- (2) Geo. W. Morey, "Properties of Glass," Second Edition (1954), Reinhold Publishing Co., New York.
- (3) William E. Forsythe, Smithsonian Physical Tables, Ninth Revised Edition (1954), Smithsonian Institution, Washington, 1. 559.
- (4) Ralph H. Wight, Jour. Solar Energy Sci. and Engr., Vol. 1 (1957), p. 84.

FIGURE 29

Reflection of Light from a Plate Glass Mirror

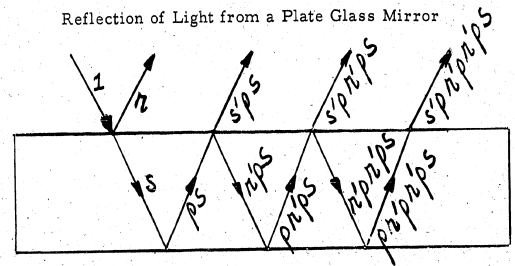


FIGURE 30

Reflection of Light from a Plate Glass Mirror in Terms of Incident and Emergent Intensities

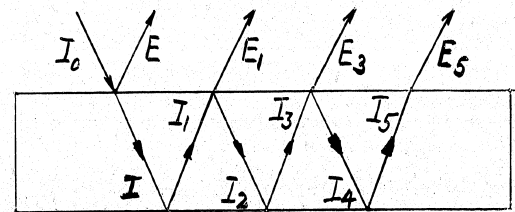
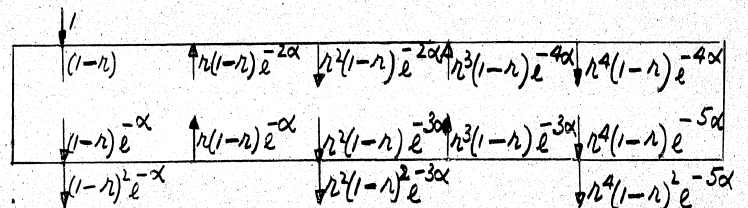


FIGURE 31

Transmission of Light by a Sheet of Plate Glass



CHAPTER 6

CALCULATION OF THE CONCENTRATION
OF THE SOLAR RADIATION THROUGH THE
FOCAL SPOT OF A PARABOLIC MIRROR



ABSTRACT

This chapter is an analysis of the power, or the energy per unit area per unit time, falling on the focal spot from a paraboloidal mirror. It is unique in that it takes account of the distribution of intensity over the solar disk as a function of wave length. The results are compared with the work of two other men who used different assumptions.

I. The Method

The energy falling per square centimeter per minute on the focal spot of a parabolic mirror has been calculated by Bliss⁽¹⁾ for a uniform sun and by Jose⁽²⁾ for a distribution curve of the intensity over the solar disc averaged for all the wave lengths. In the present report we shall take account of the fact that the distribution of intensity over the solar disc is a function of the wave length.

Suppose we have given for a certain wave length band first $f(x)$, where x is the ratio of the intensity I at a distance r from the center of the solar disc to the intensity I_0 at the center of the solar disc, i. e., let

$$I/I_0 = f(x) \quad (1)$$

where

$$x = r/R_S \quad (2)$$

R_S being the radius of the solar disc; and, secondly, let ℓ be the energy in calories per minute falling on one square centimeter of area normal to the direction of the sun for the given wave length band.

Let R be the radius of the image of the solar disc formed in a plane which is perpendicular to the axis of the cone of light reflected from a projected area of one square centimeter. The power passing through this disc is ℓ cal/cm² per second. I_0 may be determined as a function of R ; we have

$$e = \int_0^R I(r) ds = \int_0^R I(r) 2\pi r dr = \int_0^1 2\pi R^2 I_0 f(\alpha) \alpha d\alpha \quad (3)$$

so that

$$I_0 = e / 2\pi R^2 \int_0^1 f(\alpha) \alpha d\alpha \quad (4)$$

$$= e / 2\pi R^2 S \quad (5)$$

where

$$S = \int_0^1 f(\alpha) \alpha d\alpha \quad (6)$$

The focal spot of a solar furnace is considered to be the circular area in the focal plane which is produced by the sunlight which is reflected from the vertex of the parabolic condenser. The radius R_a of the spot is given by $R_a = F\alpha/2$, where F is the focal length of the condenser and α is the apparent angular diameter of the sun. The cone of light which is reflected from any point of zone angle θ has the circular cross-sections,

$$R = \rho\alpha/2 = \frac{2F}{(1+\cos\theta)} \frac{\alpha}{2} = \frac{2R_a}{(1+\cos\theta)} \quad (7)$$

where ρ is the distance from the point on the paraboloid from which the light is reflected to the focal point since it can be shown that

$$\rho = 2F / (1 + \cos\theta) \quad (8)$$

In the vicinity of the focal plane the reflected cone of light has a circular base of radius R . The flux through an elliptical area centered on the circular section of this cone is the part of the total flux which it passes through the focal area. This elliptical area is the projection of the focal spot on the circular section of the cone.

The semimajor axis a of the ellipse is R_a . The semiminor b is $R_a \cos\theta$. The energy passing through the ellipse is

$$E(\theta) = 4 \int_a^R I(r) r \phi(-dr) + \int_0^R I(r) 2\pi r dr \quad (9)$$

where

$$\phi = \arcsin \left\{ \cot\theta \sqrt{\frac{R^2(1+\cos\theta)^2}{4r^2} - 1} \right\} \quad (10)$$

Changing variables, we can write

$$E(\theta) = -4 \int_{x_1}^{x_2} R^2 I_0 f(x) \phi(x) x dx \quad (11)$$

$$+ \int_0^{x_2} R^2 I_0 f(x) 2\pi x dx$$

where

$$\phi(x) = \arcsin \left\{ \cot \theta \sqrt{\left(\frac{1+\cos \theta}{2x}\right)^2 - 1} \right\} \quad (12)$$

$$x_1 = a/R = (1 + \cos \theta)/2 \quad (13)$$

and

$$x_2 = b/R = (1 + \cos \theta)(\cos \theta)/2 \quad (14)$$

Substituting for I_0 its value, we have

$$E(\theta) = -\frac{2e}{\pi S} \int_{x_1}^{x_2} f(x) \phi(x) x dx \quad (15)$$

$$+ \frac{e}{S} \int_0^{x_2} f(x) x dx = E_1(\theta) + E_2(\theta)$$

$E(\theta)$ is the energy passing through the focal spot from light reflected at an angle θ to the axis of the paraboloid per unit area of incident light projected on the paraboloid for the chosen wave length band. The total energy $dE(\theta)$ reflected at the angle θ is proportional to the area of a ring of radius $2\pi \rho \sin \theta$ and of width $\rho d\theta$, that is

$$dE(\theta) = E(\theta) 2\pi \rho^2 \sin \theta d\theta \quad (16)$$

so that the total energy $\Sigma(\theta)$ over the whole paraboloid is given by

$$\Sigma(\theta) = 8\pi F^2 \int_0^{\theta_1} \frac{E(\theta) \sin \theta d\theta}{(1 + \cos \theta)^2} \quad (17)$$

where θ_1 is the angle of opening of the paraboloid.

The concentration $C(\lambda)$ is the total energy passing through the focal spot divided by the area of the focal spot so that we have

$$C(\lambda) = \frac{8\pi F^2}{\pi \alpha^2 F^2/4} \int_0^{\theta_1} \frac{E(\theta) \sin \theta d\theta}{(1 + \cos \theta)^2} \quad (18)$$

$$= \frac{32}{\alpha^2} \int_0^{\theta_1} \frac{E(\theta) \sin \theta d\theta}{(1 + \cos \theta)^2} \quad (19)$$

The concentration $C(\lambda)$ represents the concentration due to the chosen wave length band. The total concentration C_T is obtained by

summing the energies concentrated in each wave length band, that is

C_t is given by

$$C_t = \sum c(\lambda)$$

where the summation is extended over all the wave length bands in the spectrum of the sun.

II. Procedure

Given $f(x)$ and e for a given wave length band, determine from the equation

$$S = \int_0^1 f(x) x dx \quad (6)$$

Next determine x_1 and x_2 from the equations,

$$x_1 = (1 + \cos \theta) / 2 \quad (13)$$

and

$$x_2 = (1 + \cos \theta)(\cos \theta) / 2 \quad (14)$$

Then determine $E(\theta)$ from the formula,

$$E(\theta) = \frac{2e}{\pi S} \int_{x_1}^{x_2} f(x) \phi(x) x dx + \frac{e}{S} \int_0^{x_2} f(x) x dx \quad (15)$$

where

$$\phi(x) = \arcsin \left\{ \cos \theta \sqrt{\left(\frac{1 + \cos \theta}{x} \right)^2 - 1} \right\} \quad (12)$$

then calculate

$$c(\lambda) = \frac{32}{x^2} \int_0^{\theta_1} \frac{E(\theta) \sin \theta d\theta}{(1 + \cos \theta)^2} \quad (19)$$

Finally calculate C_t , where C_t is given by

$$C_t = \sum c(\lambda)$$

III. Check of the Formulas for a Uniform Sun

The concentration factor for a uniform sun has been given by Bliss⁽¹⁾. We will see if the formulas developed above give the same result.

For a uniform sun $f(x) = 1$ and $S = 1/2$ so that we have

$$\begin{aligned} E(\theta) &= \frac{e}{2\pi S} 4 \int_{x_1}^{x_2} \phi(x) x (-dx) + \frac{e}{S} \int_0^{x_2} x dx \\ &= (e/\pi) (\pi x_1 x_2 - \pi x_2^2) + e x_2^2 = e x_1 x_2 \end{aligned}$$

$$= \frac{4}{\alpha^2} (1 + \cos \theta)^2 (\cos \theta) / 4$$

Substituting this value in Eq. (17), there results

$$C = \frac{32l}{\alpha^2} \int_0^{\theta_1} \sin \theta \cos \theta d\theta = \frac{8}{\alpha^2} \frac{\sin^2 \theta_1}{2}$$

$$= (4l \sin^2 \theta_1) / \alpha^2 = C_l$$

where C_l is the concentration factor of Bliss, which gives

$$C = (4 \sin^2 \theta_1) / \alpha^2$$

This checks the result given by Bliss.

As a further check lets us compare with the formula given by Jose⁽²⁾ for the concentration factor.

According to Jose, this is given by

$$C = \frac{4}{\alpha^2} \int_0^{\theta_1} R_x \sin \theta d\theta$$

where R_x is given by

$$R_x = \frac{E_0}{l} \frac{4}{(1 + \cos \theta)^2} \sin 2\theta$$

so that

$$C = \frac{4}{\alpha^2} \int_0^{\theta_1} \frac{E(\theta)}{l} \frac{4}{(1 + \cos \theta)^2} 2 \sin \theta d\theta$$

$$= \frac{32}{\alpha^2} \int_0^{\theta_1} \frac{E(\theta)}{l} \frac{\sin \theta d\theta}{(1 + \cos \theta)^2}$$

This checks Eq. (19) of this paper since $C = C_l$.

IV. Calculations

By interpolation from Table 814⁽³⁾, the values given in Table XVII were derived.

Table XVII. $f(x)$

	λ								
x	.425	.625	.875	1.25	1.75	2.25	2.75	3.75	
.30	.977	.978	.985	.988	.993	.995	.996	.996	
.50	.906	.937	.953	.967	.980	.980	.983	.988	
.60	.855	.902	.928	.947	.969	.968	.972	.980	
.70	.797	.855	.895	.922	.952	.953	.959	.969	
.80	.710	.785	.847	.885	.928	.931	.939	.952	
.90	.577	.687	.771	.821	.882	.891	.905	.928	
.95	.470	.605	.703	.759	.837	.850	.870	.902	
.975	.389	.537	.647	.710	.792	.814	.837	.875	

From the values given in Table XVII, the values of $f(x)$ were calculated and are given in Table XVIII.

Table XVIII. $x f(x)$

x	λ							
	.425	.625	.875	1.25	1.75	2.25	2.75	3.75
.00	.000	.000	.000	.000	.000	.000	.000	.000
.30	.293	.293	.296	.296	.298	.299	.299	.299
.50	.453	.468	.477	.484	.490	.490	.492	.494
.60	.513	.541	.557	.568	.581	.581	.583	.588
.70	.558	.599	.627	.645	.666	.667	.671	.678
.80	.568	.628	.678	.708	.742	.745	.751	.761
.90	.519	.618	.694	.739	.794	.802	.814	.835
.95	.497	.575	.668	.721	.795	.807	.826	.855
.975	.379	.524	.631	.692	.772	.794	.816	.853

From the values given in Table XVIII, the values of $\delta = \int_0^1 f(x) x dx$ were calculated and are given in Table XIX.

Table XIX. Partial Integrands for δ .

x	λ							
	.425	.625	.875	1.25	1.75	2.25	2.75	3.75
0-.30	.0440	.0440	.0444	.0444	.0447	.0449	.0449	.0449
.30-.50	.0746	.0761	.0773	.0780	.0788	.0789	.0791	.0793
.50-.60	.0483	.0505	.0527	.0526	.0536	.0536	.0538	.0541
.60-.70	.0536	.0570	.0592	.0607	.0624	.0624	.0627	.0633
.70-.80	.0563	.0614	.0653	.0677	.0704	.0706	.711	.0720
.80-.90	.0544	.0623	.0686	.0724	.0768	.0774	.0783	.0798
.90-.95	.0242	.0299	.0341	.0365	.0397	.0402	.0410	.0423
.95-.975	.0103	.0137	.0163	.0177	.0196	.0200	.0205	.0214
.975-1.00	.0047	.0065	.0079	.0087	.0097	.0099	.0102	.0107
	.3704	.4017	.4258	.4387	.4557	.4579	.4616	.4678

The values of e given in Table XX were taken from the paper by Wight⁽⁴⁾. The value of the wave length at the center of the band as well as the wave length interval are also given in Table XX.

Table XX.

λ	e	λ_0	$\Delta\lambda$
.35-.50	.44	.425	.15
.50-.75	.48	.625	.25
.75-1.00	.28	.875	.25
1.00-1.50	.32	1.25	.50
1.50-2.00	.14	1.75	.50
2.00-2.50	.04	2.25	.50
2.50-3.00	.03	2.75	.50
3.00-4.50	.03	3.75	1.50

From the values for e given in Table XX and the values of δ given in Table XIX, the constants $2e/\pi\delta$ and e/δ were calculated and are given in Table XXI.

Table XXI.

λ	$2e/\pi\delta$	e/δ
.425	.756	1.188
.625	.761	1.295
.875	.419	.658
1.25	.464	.729
1.75	.195	.307
2.25	.0556	.0874
2.75	.0414	.0650
3.75	.0411	.0646

The values of λ_1 and λ_2 were calculated and the results are given in Table XXII.

Table XXII.

θ	λ_1	λ_2	$\Delta\lambda = \lambda_1 - \lambda_2$
0°	1.000	1.000	.000
10°	.993	.978	.015
20°	.970	.912	.058
30°	.933	.808	.125
40°	.883	.676	.207
50°	.822	.529	.293
60°	.750	.375	.375
70°	.671	.229	.442
80°	.587	.102	.485
90°	.500	.000	.500

The values $\lambda_1 - \lambda_2$ were split up into intervals and the value of $\phi(\lambda)$ calculated for the end points of each interval. The results are given in Table XXIII.

Table XXIII.

θ	Intervals	$\Delta\lambda$	λ	$\phi(\lambda)$
10°	1	.015	.978	1.571
			.993	.000
20°	1	.058	.912	1.571
			.970	.000
30°	1	.125	.808	1.571
			.933	.000
40°	2	.103	.676	1.571
			.779	.693
			.883	.000
50°	3	.098	.529	1.571
			.627	.792
			.725	.466
			.822	.000
60°	4	.094	.375	1.571
			.469	.793
			.563	.533
			.657	.323
			.750	.000
70°	4	.1105	.2290	1.571
			.3395	.670
			.4500	.415
			.5605	.242
			.6710	.000

Corresponding to the same intervals, the values of $f(x)$ were calculated by interpolation from Table XVII and the results entered in

Table XXIV.

Table XXIV. $f(x)$

θ	x	λ							
		.425	.625	.875	1.25	1.75	2.25	2.75	3.75
10°	.978	.342	.531	.569	.625	.697	.716	.718	.770
20°	.912	.551	.667	.755	.806	.871	.881	.897	.922
30°	.808	.699	.777	.841	.880	.924	.928	.936	.950
40°	.676	.811	.866	.903	.928	.956	.957	.963	.972
	.779	.728	.800	.857	.893	.933	.936	.943	.956
50°	.529	.891	.927	.946	.961	.987	.977	.980	.986
	.627	.840	.890	.919	.940	.964	.964	.969	.977
	.725	.775	.837	.883	.913	.946	.948	.954	.965
60°	.375	.950	.962	.973	.980	.988	.989	.991	.993
	.469	.917	.943	.958	.970	.982	.982	.985	.989
	.563	.874	.915	.937	.954	.973	.972	.976	.985
	.657	.822	.875	.910	.933	.959	.959	.965	.974
70°	.2290	.982	.983	.989	.991	.995	.996	.997	.997
	.3395	.963	.970	.979	.984	.990	.992	.993	.994
	.4500	.924	.961	.961	.972	.983	.984	.986	.990
	.5605	.875	.916	.940	.955	.973	.973	.976	.984

From the values of the constants given in Table XXI, the values of $\phi(x)$ given in Table XXIII and the values of $f(x)$ given in Table XXIV, the integrals $E_1(\theta)$ were calculated and the results are given in Table XXV.

The intervals given in Table XXIII were used.

Table XXV. $E_1(\theta)$

θ	λ							
	.425	.625	.875	1.25	1.75	2.25	2.75	3.75
10°	.00298	.00466	.00275	.00334	.00157	.00046	.00034	.00037
20°	.0173	.0211	.0132	.0155	.00706	.00204	.00154	.00158
30°	.0419	.0469	.0280	.0324	.0143	.00409	.00307	.00311
40°	.0641	.0699	.0407	.0466	.0203	.0060	.00435	.00449
50°	.0777	.0828	.0471	.0534	.0231	.0066	.00491	.00493
60°	.0751	.0784	.0439	.0467	.0211	.0060	.00451	.00451
70°	.0575	.0589	.0328	.0366	.0155	.0044	.00330	.00329

From the values of λ_2 given in Table XXII and those of $f(x) x dx$ given in Table XIX, the values of the integrals $E_2(\theta)$ were calculated.

The results are given in Table XXVI.

Table XXVI. $E_2(\theta)$

θ	λ							
	.425	.625	.875	1.25	1.75	2.25	2.75	3.75
10°	.4353	.5125	.2757	.3142	.1373	.0393	.0294	.0296
20°	.4004	.4643	.2472	.2803	.1216	.0347	.0260	.0261
30°	.3342	.3807	.2003	.2254	.0970	.0277	.0207	.0206
40°	.2468	.2770	.1443	.1612	.0689	.0196	.0147	.0146
50°	.1575	.1745	.0901	.1004	.0427	.0122	.0091	.0090
60°	.0854	.0939	.0482	.0537	.0229	.0065	.0049	.0048
70°	.0399	.0435	.0223	.0247	.0105	.0030	.0022	.0022

The results entered in Tables XXV and XXVI were added to give $E(\theta)$ and are entered in Table XXVII.

Table XXVII. $E(\theta)$

θ	λ							
	.425	.625	.875	1.25	1.75	2.25	2.75	3.75
10°	.4383	.5172	.2785	.3175	.1389	.0398	.0297	.0300
20°	.4177	.4854	.2604	.2958	.1287	.0367	.0275	.0277
30°	.3761	.4276	.2283	.2578	.1113	.0318	.0238	.0237
40°	.3109	.3469	.1850	.2078	.0892	.0256	.0191	.0191
50°	.2352	.2573	.1372	.1538	.0658	.0188	.0140	.0139
60°	.1605	.1723	.0921	.1004	.0440	.0125	.0094	.0093
70°	.0974	.1024	.0551	.0613	.0260	.0074	.0055	.0055

Next the values of the function $\frac{\sin \theta}{(1 + \cos \theta)^2}$ were calculated and entered in Table XXVIII.

Table XXVIII.

θ°	$\frac{\sin \theta}{(1 + \cos \theta)^2}$
10	.0442
20	.0909
30	.144
40	.206
50	.284
60	.385
70	.522

From the values of $E(\theta)$ given in Table XXVII and the values of

$\frac{\sin \theta}{(1 + \cos \theta)^2}$ given in Table XXVIII, the values of the elements

$$\frac{1.76}{0.093} E(\theta) \left(\frac{\sin \theta}{(1 + \cos \theta)^2} \right) d\theta$$

were calculated and entered in Table XXIX.

Table XXIX.

θ	λ							
	.425	.625	.875	1.25	1.75	2.25	2.75	3.75
10°	625	738	397	453	198	57	42	43
20°	1230	1420	764	868	378	108	81	81
30°	1750	1990	1060	1200	517	148	110	110
40°	2070	2310	1230	1380	593	170	127	127
50°	2160	2360	1260	1410	603	172	128	127
60°	1990	2140	1140	1250	547	155	117	116
70°	1640	1730	929	1030	438	125	93	93

By adding the values given in Table XXIX, the values of $C(\lambda)$ were obtained for various values of λ as given in Table XXX. The values were added to give the final values of the concentration for $\theta = 50^\circ, 60^\circ$ and 70° .

Table XXX. $C(\lambda)$

	$\theta = 50^\circ$	$\theta = 60^\circ$	$\theta = 70^\circ$
.425	14,510	18,660	22,290
.625	15,276	19,776	23,646
.875	8,162	10,562	12,631
1.25	9,212	11,872	14,152
1.75	3,975	5,125	6,110
2.25	1,138	1,465	1,745
2.75	848	1,093	1,303
3.75	809	1,092	1,301
	53,970	69,645	83,178

These final results give the energy in cal/cm² per minute concentrated in the focal spot. The corresponding values in cal/cm² per second are given by

	conc.
50°	896 cal/cm ² /sec.
60°	1161 " " "
70°	1386 " " "

These values are on the basis of a total of 1.76 cal/cm² per min received at the earth's surface.

Comparing with the values obtained by Jose⁽²⁾ for a total of 1.94 cal/cm² per min, we find:

	Simon	Jose	Ratio S/J
50°	53,970	55,300	.976
60°	69,645	71,800	.970
70°	83,178	85,500	.973

Or, if we calculate the concentration ratio by dividing these values respectively by 1.76 and 1.94, we obtain

	Simon	Jose	Ratio S/J
50°	30,700	28,498	1.076
60°	39,600	37,016	1.069
70°	47,300	44,104	1.072

The difference is apparently due to the fact that Jose has used an average distribution curve for all the wave lengths, while in this report distribution curves corresponding to various wave length bands have been used. While the concentration ratio obtained by Simon is 7.2% higher than that of Jose, the total energy used by Simon is 9.3% lower than that used by Jose, which accounts for the fact that Simon obtains an energy concentration 2.7% lower than that of Jose. However, Simon calculates the concentration on the basis of the energy reaching the surface of the earth (Wight) while Jose calculates the concentration on the basis of the energy striking the outer atmosphere, i.e., he neglects atmospheric absorption.

References

- (1) Raymond W. Bliss, Jr., "Notes on Optical Design Principles, Concentration Ratios, and Maximum Temperature of Parabolic Solar Furnaces," Technical Memorandum No. HDW-TM-56-1, Holloman Air Development Center, July 1956.
- (2) Paul D. Jose, "The Flux through the Focal Spot of a Solar Furnace," Technical Memorandum No. HDRRM-TM-57-3, Holloman Air Development Center, April 1957.
- (3) William E. Forsythe, Smithsonian Physical Tables, Ninth Revised Edition (1954), Smithsonian Institution, Washington, p. 722.
- (4) Ralph H. Wight, Jour. Solar Energy Sci. and Engr., Vol. 1 (1957), p. 84.

CHAPTER 7

CALCULATION OF THE CONCENTRATION
OF ENERGY AT POINTS OUTSIDE THE
FOCAL SPOT OF A PARABOLIC CONDENSER

STAT



ABSTRACT

This chapter is an analysis of the distribution of intensity and of energy falling outside of the circular projection of the cone of reflected radiation coming from all infinitesimal areas of the surface of a paraboloidal mirror. The method integrates the energy and intensity falling in the area swept by the major semi-axis of the ellipses subtended by the focal plane. The results are tabulated and graphed.

The energy collected by an infinitesimal area on the surface of the paraboloid mirror is spread in the focal plane over the area of an ellipse of semimajor axis $R/\cos \theta$ and semiminor axis equal to R , where R is the radius of the base of cone of light whose axis makes an angle θ with the axis of the paraboloid and whose center lies at the center of the focal spot. As the axis of the cone moves around the paraboloid at constant angle θ , the major axis of the ellipse will rotate so that the energy collected by a ring of radius $\rho \sin \theta$ and width $\rho d\theta$, where ρ is the distance from the ring to the focal spot of the paraboloid, is spread over a circle of radius $R/\cos \theta$.

Inside a circle of radius R the intensities add, being equal to

$$dI_c = \frac{e}{\pi R^2 / \cos \theta} 2\pi \rho^2 \sin \theta d\theta \quad (1)$$

where dI_c represents the differential with respect to θ of the intensity inside the circle of radius R and e represents the solar constant.

The energy spread over a circle of radius R is given by $\pi R^2 dI_c$ that is

$$dE_c = 2\pi e \rho^2 \sin \theta \cos \theta d\theta \quad (2)$$

but the total energy dE collected by the ring is given by

$$dE = 2\pi e \rho^2 \sin \theta d\theta \quad (3)$$

leaving an amount of energy dE_n given by

$$dE_n = 2\pi e p^2 \sin \theta (1 - \cos \theta) d\theta \quad (4)$$

to be spread over a ring in the focal plane of inner radius R and outer radius $R/\cos \theta$. This energy falls on an area A_n given by

$$A_n = (\pi R^2 / \cos^2 \theta) - \pi R^2 \quad (5)$$

hence, the corresponding intensity dI_n is

$$dI_n = \frac{2\pi e p^2 \sin \theta (1 - \cos \theta) \cos^2 \theta d\theta}{\pi R^2 \sin^2 \theta} \quad (6)$$

$$= \frac{2e p^2 (1 - \cos \theta) \cos^2 \theta d\theta}{R^2 \sin \theta} \quad (7)$$

Substituting for R its value $\rho \alpha / 2$ where α is the angular diameter of the sun, we have

$$dI_n = (8e/\alpha^2) \sin \theta \cos \theta d\theta \quad (8)$$

$$dI_n = \frac{(8e/\alpha^2)(1 - \cos \theta) \cos^2 \theta d\theta}{\sin \theta} \quad (9)$$

If now we choose a circle in the focal plane of radius R where $R > R_a$, the radius of the focal spot, up to a certain angle θ_2 given by $R_2 = r$, all the circles of radius $R < r$ will lie within the circle of radius r , while all the circles such that $R > r$ will lie without the circle of radius r . For the radius R_2 we have

$$R_2 = 2R_a / (1 + \cos \theta_2) = r \quad (10)$$

whence

$$\cos \theta_2 = (2R_a / r) - 1 \quad (11)$$

The outer radius R_3 of the ring over which the energy dE_n is distributed is given by

$$R_3 / \cos \theta_3 = 2R_a / (1 + \cos \theta_3) \cos \theta_3 = r \quad (12)$$

so that

$$\cos \theta_3 = \left\{ \frac{-1 + \sqrt{1 + 8R_a / r}}{2} \right\} \quad (13)$$

Now provided that $r < R_1$ where R_1 is the radius of the base of the cone of light corresponding to the maximum value θ_1 of the paraboloid, we have as the resulting intensity I_n inside a circle of radius r

$$I_n = (8e/\alpha^2) \int_{\theta_3}^{\theta_1} \sin \theta \cos \theta d\theta + (8e/\alpha^2) \int_{\theta_3}^{\theta_2} \frac{(1 - \cos \theta) \cos^2 \theta d\theta}{\sin \theta} \quad (14)$$

while if $R_1 < n < R_1/\cos \theta_1$

$$I_n = (8e/\alpha^2) \int_{\theta_3}^{\theta_1} \frac{(1 - \cos \theta) \cos^2 \theta d\theta}{\sin \theta} \quad (15)$$

while if $n \geq R_1/\cos \theta_1$, the resulting intensity is zero.

The resulting functions can all be easily integrated. We have for

$$R_a < n < R_1 \\ I = (8e/\alpha^2) [\cos \theta_2 - \log_e (1 + \cos \theta_2) + (\sin^2 \theta_1)/2 - \cos \theta_3 + \log_e (1 + \cos \theta_3) - (\sin^2 \theta_3)/2] \quad (16)$$

while for $R_1 < n < R_1/\cos \theta_1$

$$I = (8e/\alpha^2) [\cos \theta_1 - \log_e (1 + \cos \theta_1) + (\sin^2 \theta_1)/2 - \cos \theta_3 + \log_e (1 + \cos \theta_3) - (\sin^2 \theta_3)/2] \quad (17)$$

while finally for $n > R_1/\cos \theta_1$, we have $I = 0$.

It is of interest to calculate the values of θ_2 and θ_3 for various special cases.

Firstly, for $n = R_a$, we have $\theta_2 = \theta_3 = 0$, so that for this case we have the result

$$I = (8e/\alpha^2) (\sin^2 \theta_1)/2$$

which is the result given by Bliss⁽¹⁾ for the intensity in the focal spot.

Secondly, for $n = R_1$, $\theta_2 = \theta_1$, or for $\theta_1 = 60^\circ$, $n = (4/3) R_a$.

Thirdly, for $n = R_1/\cos \theta_1$, $\theta_3 = \theta_1$, when $I = 0$. For $\theta_1 = 60^\circ$ this corresponds to a value of n/R_a of 2.67.

The values of $\cos \theta_2$, $\log_e (1 + \cos \theta_2)$, $\cos \theta_3$, $\log_e (1 + \cos \theta_3)$ and $(\sin^2 \theta_3)/2$ were calculated and are given in Table XXXI.

TABLE XXXI.

r/R_0	$\cos \theta_0$	$\log(1 + \cos \theta_0)$	$\cos \theta_0$	$\log(1 + \cos \theta_0)$	$\frac{1}{2} \sin^2 \theta_0$
1.0	1.0000	.6931	1.0000	.6931	.0000
1.1	.8182	.5978	.9382	.6618	.0599
1.2	.6667	.5108	.8816	.6321	.1114
1.3	.5385	.4308	.8346	.6068	.1516
1.4			.7930	.5839	.1856
1.5			.7558	.5629	.2143
1.6			.7248	.5451	.2374
1.7			.6920	.5299	.2606
1.8			.6644	.5095	.2793
1.9			.6392	.4942	.2957
2.0			.6180	.4812	.3091
2.2			.5747	.4541	.3348
2.4			.5389	.4311	.3547
2.67			.5000	.4055	.3750

The results given in Table XXXI were combined to give the quantities in brackets in Eqs. (16) or (17) depending on the value of r/R_0 and are in the second column of Table XXXII. The quantities in the second column were divided by .375 to obtain the ratio I/I_a given in the third column. To obtain the ratio of the total energy E falling within the circle of radius r to the energy E_a falling within the focal spot, it was noted that this quantity is given by the equation

$$E/E_a = \sum \frac{2\pi r_m (I_i + I_{i+1}) \Delta r}{\pi R_a^2 2 I_a} \quad (18)$$

where r_m is the mean radius of a ring of inner radius r_i and outer radius r_{i+1} and thickness Δr . This reduces to the equation

$$E/E_a = \sum \frac{r_m}{R_a} \left(\frac{I_i}{I_a} + \frac{I_{i+1}}{I_a} \right) \frac{\Delta r}{R_a} \quad (19)$$

From this equation the values in the fourth column of Table XXXII were calculated.

TABLE XXXII.

r/R_a	Σ	I/I_a	E/E_a
1.0	.3750	1.0000	1.0000
1.1	.2591	.6909	1.1175
1.2	.1700	.4533	1.3091
1.3	.1033	.2755	1.4002
1.4	.0748	.1995	1.4643
1.5	.0623	.1661	1.5173
1.6	.0524	.1397	1.5647
1.7	.0428	.1141	1.6066
1.8	.0353	.09413	1.6430
1.9	.0288	.07680	1.6746
2.0	.0236	.06293	1.7018
2.2	.0141	.03760	1.7440
2.4	.0070	.01867	1.7699
2.67	.0000	.0000	1.7827

Needless to say, these values are obtained on the basis of a uniform sun.

The values of I/I_a and E/E_a as a function of r/R_a have been plotted in Figures XXXI and XXXII.

Finally, it is of interest to compute the fractional part of the total energy concentrated in the focal spot and compare with result given in Table XXXII. We have as the energy dE collected by a ring of radius $\rho \sin \theta$ and width $\rho d\theta$ at an angle θ with the axis.

$$dE = e 2\pi \rho^2 \sin \theta d\theta \quad (20)$$

and as the total energy E collected by the paraboloid

$$E = \int_0^{\theta_1} e 2\pi \rho^2 \sin \theta d\theta \quad (21)$$

Substituting for ρ its value $2F/(1+\cos \theta)$ this becomes

$$E = \int_0^{\theta_1} \frac{8\pi e F^2 \sin \theta d\theta}{(1+\cos \theta)^2} \quad (22)$$

which gives for E the value

$$E = -4\pi e F^2 (1 - \cos \theta_1) / (1 + \cos \theta_1) \quad (23)$$

For $\theta_1 = 60^\circ$ this becomes

$$E = 4\pi e^2 F^2 / 3 \quad (24)$$

For the focal spot we had as the intensity I

$$I = (8e/\alpha^2) (\sin^2 \theta_1) / 2 \quad (25)$$

so that the total energy E_a collected by the focal spot is given by

$$E_a = \pi R_a^2 (8e/\alpha^2) (\sin^2 \theta_1) / 2 \quad (26)$$

Substituting in this expression for R_a its value $F\alpha/2$, we have

$$E_a = \pi F^2 e \sin^2 \theta_1 \quad (27)$$

For $\theta_1 = 60^\circ$ this becomes

$$E_a = \pi F^2 e 3/4 \quad (28)$$

so that we have for the ratio

$$E_a/E = \frac{3}{4} \times \frac{3}{4} = 9/16 = 56.3\%$$

Comparing this with the values given in Table XXXII, namely

$$E_a/E = 1.000/1.7827 = 56.1\%$$

we see that the agreement is very good.

References

- (1) Raymond W. Bliss, Jr., "Notes on Optical Design Principles, Concentration Ratios, and Maximum Temperature of Parabolic Solar Furnaces," Technical Memorandum No. HDW-TM-56-1, Holloman Air Development Center, July 1956.

FIGURE 32.

Intensity as a Function of Distance from Center of Focal Spot

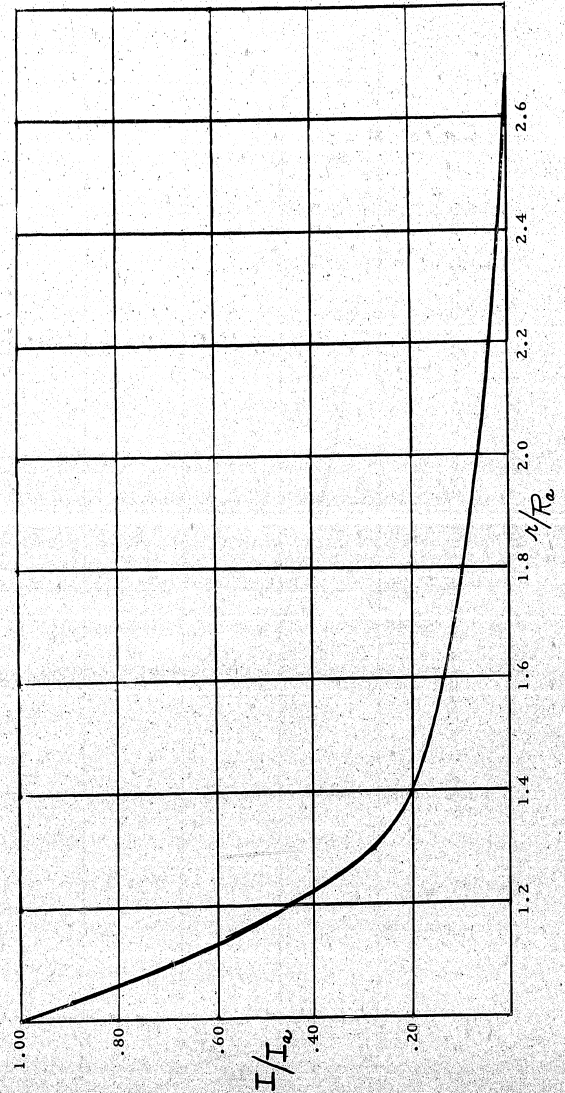
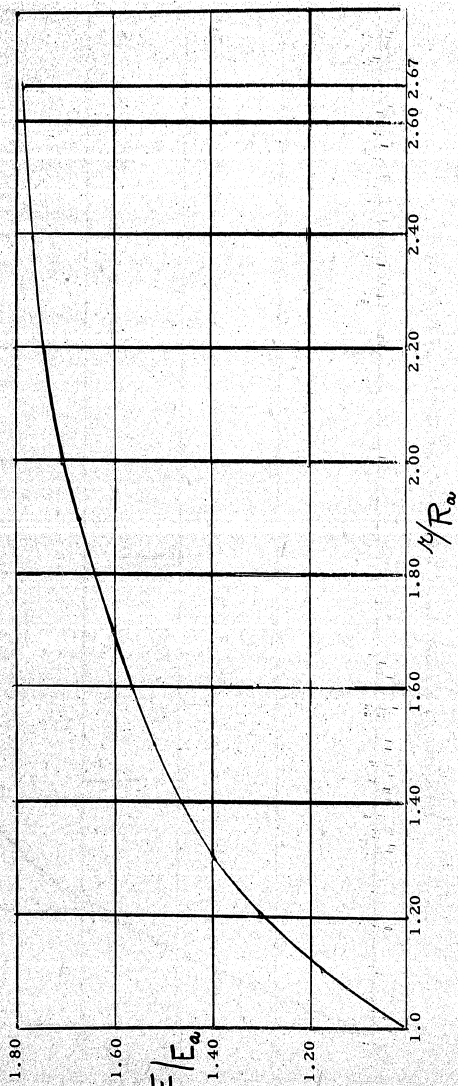


FIGURE 33.

Total Energy as a Function of Distance from Center of Focal Spot



CHAPTER 8

RIGID-BODY TORSIONAL
OSCILLATIONS OF AXIALLY
SUPPORTED HELIOSTAT MIRROR



ABSTRACT

The rotational oscillations of a large-scale flat mirror structure are studied on the basis of random input response of a second order linear system. The excitation is supplied by the random pressure distribution across the mirror surface under various assumptions pertaining to the turbulent characteristics of wind.

It is concluded that the axial support, as proposed in the existing preliminary design, has little chance to perform within the expected tolerance specifications above a few mph average wind velocity. Suggestions of principle are made for radically different support designs, leading to improved performance, and possibly some cost savings.

I. Introduction

Discussed in this report are the torsional oscillations of an unusually large-scale flat "heliostat" mirror intended to be part of the Department of Defense Solar Furnace in Cloudcroft, New Mexico. The preliminary design sketches and the expected operating characteristics have been examined by the 1957 Summer Research Group, Operations Research Office, Air Force Missile Development Center.

The purpose of the group activity is to secure an independent and possibly more general appraisal of the problems involved and solutions proposed thereto. It is definitely intended that the findings be interpreted not as alternate designs but rather as orientations for the next design steps.

The heliostat mirror discussed here is essentially a 145-ft x 145-ft flat plate, composed of 4-ft x 4-ft plate glass second surface mirrors, arranged in a mosaic array to cover the reflecting surface required for the solar furnace operation.*

The normal to the heliostat surface is intended to follow the sun's apparent diurnal motion so that the reflected ray originating in the center of the solar disk be coincident with the (fixed) horizontal axis of the

* The numbers quoted here are meant to be representative, based on various reports, design notes and verbal information received from the Air Force Missile Development Center monitoring group and the Pittsburgh-Des Moines Steel Co. Minor changes in these numbers will not essentially affect the conclusions reported here.

parabolic concentrator within ± 1 minute of arc.

On the basis of astronomical data at 33° latitude, the maximum azimuthal motion of the sun is $\pm 103^\circ$, and the maximum altitude above the horizon is about 80° .

The axis of the heliostat must thus be orientable by $\pm 51\frac{1}{2}^\circ$ centered on South around the vertical axis; it should also assume any position between $+15^\circ$ and $+40^\circ$ altitude around the horizontal axis.

It is desirable, though not essential, that the mirror may be placed completely horizontal for cleaning and alignment purposes.

The supporting and actuating structures are unusual with respect to

- a. The extraordinarily large dimensions,
- b. The close tolerance specifications on the variable positions,
- c. The severe environmental conditions such as wind, insulation and corrosion.

The problems of structural rigidity, self-excited vibrations and effects of Karman vortices were considered by other members of the group.

Some experimental indications are available on the effect of thermal stresses in the plate glass surface. The problem discussed here is the rigid-body motion of a flat plate elastically supported at its central horizontal axis. (See Figure 34)

It is assumed that the structure is represented by the flat plate AB having the same weight and dimensions as the actual heliostat frame. The 6' diameter drum (shaft) is said to position the frame on the transverse supports C, D, E and F, it being understood that none of these present torsional rigidity. The positioning and torsional rigidity is purportedly assured by the gear and pinion assembly in G. Whereas the operation of gears with the required torques and accuracies may present a problem of no inconsiderable magnitude, it is felt that one of the main objections against such an arrangement is found in the poor rigidity characteristics of the drum-shaft.

The problem of elastic shaft deformation cannot be eliminated by multiplying the points of rotational support. The torque-position synchronization between a number of such supports is almost impossible within the tolerances required.

The ensuing discussion is based on the sketches now available, i.e., a single driving gear, located at about 25 ft from the nearest torsional support. The possible motion around the (horizontal) shaft is studied under random turbulent wind excitation.

II. Numerical Data

a. Heliostat Mirror Structure

The weight of $1/4$ inch plate glass, based on 200 lb/cu. ft, is approximately 4.2 lb/sq. ft. The metal support and adjustment structure can be estimated at 6 lb/sq. ft. with an additional 5 lb/sq. ft. for

the structural steel frame itself. On the basis of 15 lb/sq. ft., the weight of the total 145 ft. x 145 ft. frame is 315,375 lbs. The mass moment of inertia of the mirror (in simulation of a rigid plate) is then:

$$I_{m_{xx}} = \frac{1}{12} M \left[L^2 - (\text{Thickness})^2 \right] \approx \frac{1}{12} \frac{w}{g} L^2 = 17.16 \times 10^6 \text{ lb. ft. sec}^2$$

(with respect to the horizontal axis) and, the area moment of inertia is

$$I_{xx} = \frac{L^4}{12} = \frac{145^4}{12} \text{ ft}^4 = 36.8 \times 10^6 \text{ ft}^4.$$

The torsional spring can be taken, for the purpose of this discussion as shown in Figure 35 the 6-foot diameter one-inch wall thickness drum being subjected to the driving torque reaction (idealized here by the built-in end) and the torque τ transmitted from the mirror frame to the drum. The 25 ft free length may appear excessive in view of the comparatively small space needed to accommodate the driving gear mechanism. In fact, however, the assumption of having all the frame reaction in this point is also unrealistic since the other torsional supports are located at 50 to 120 ft from the driving gear. The torsional spring constant under these assumptions is:

$$C = \frac{GI_p}{\ell}$$

G = Torsional Modulus of Elasticity

$$G = 12 \times 10^6 \text{ psi} \times 144 \text{ (lbs/ft}^2\text{)}$$

$$I_p = \frac{\pi}{2} (r^4 - r_i^4) \approx 2\pi r^3 t \text{ (where } t \ll r) \approx 2\pi 3^3 \frac{1}{12} \text{ (ft}^4\text{)}$$

$$\ell = 25 \text{ ft.}$$

$$C = 9.75 \times 10^8 \frac{\text{lb ft}}{\text{rad}}$$

$$C = 17 \times 10^6 \frac{\text{lb ft}}{\text{degree}}$$

The structural damping may be safely neglected with respect to the viscous forces of aerodynamic origin; one possible way to evaluate damping is to assume that the differential drag due to the torsional oscillations is responsible therefor.

Let C_D be the drag coefficient ≈ 1.1 for flat plate,

V_0 = the average wind velocity (15 ft/sec assumed),

ρ = mass density of air at 8800 ft altitude,

$$\rho \approx 1.84 \times 10^{-3} \text{ slugs/ft}^3.$$

The force on a double strip of length L , width dy , located at distance $\pm y$ from the axis is:

$$F_{\mathcal{L}} = C_D \frac{1}{2} \rho (V_0 + dv)^2 L dy \text{ and } F_{\mathcal{R}} = C_D \frac{1}{2} \rho (V_0 - dv)^2 L dy$$

which act as a couple on both sides of the axis so that the elementary torque is: (at lever arm "y")

$$d\mathcal{T} = C_D \frac{1}{2} \rho \left[(V_0 + dv)^2 - (V_0 - dv)^2 \right] L dy \times y$$

$$d\mathcal{T} = C_D \frac{1}{2} \rho 4 V_0 dv L y dy$$

On the other hand, $dv = y \frac{d\theta}{dt}$ if θ is the angle thru which the plate (heliostat) rotates and there is no wind gradient with respect to y ,

i. e., $\frac{dv}{dy} = 0$.

$$\tau = I_{m_{xx}} \alpha + 2 C_D \int_0^{L/2} \frac{1}{2} \rho^4 V_0^2 dy + C \theta$$

$$\alpha = \frac{\rho^2 \theta}{2 \rho^2}$$

The aerodynamic viscous damping torque, from the second term, is found by integration:

$$\tau_d = 4 C_D \rho V_0 L \int_0^{L/2} dv y dy$$

But: $dv = y \frac{d\theta}{dt} = y \omega$

$$\tau_d = 4 C_D \rho V_0 L \omega \int_0^{L/2} y^2 dy$$

$$= 4 C_D \rho V_0 L \omega \left[\frac{y^3}{3} \right]_0^{L/2}$$

$$= 4 C_D \rho V_0 L \omega \left[\frac{L^3}{3 \times 8} \right]$$

$$= \frac{1}{6} C_D \rho V_0 L^4 \omega, \text{ or } 2 C_D \rho V_0 I_{xx} \omega$$

Because, $I_{xx} = \frac{L^4}{12}$

$$\therefore \beta = \frac{1}{6} C_D \rho V_0 L^4, \text{ or } 2 C_D \rho V_0 I_{xx}$$

β = damping coefficient

For $\alpha = 0$; this may be numerically evaluated for various constant values of " ω " and of " V_0 ".

This analysis is good only for the "steady state" case, $V_0 =$ a constant.

$$\beta = 2 C_D \rho V_0 I_{xx}$$

$$C_D = 1.1$$

$$\rho = 1.84 \times 10^{-3} \text{ slugs/ft}^3$$

$$V_0 = 15 \text{ ft/sec}$$

$$I_{xx} = \frac{145^4}{12} \text{ ft}^4 = 36.8 \times 10^6 \text{ ft}^4$$

$$\beta = 2.23 \times 10^6 \frac{\text{lb. ft.}}{\text{rad/sec}}$$

It is necessary to observe that the damping will increase with the average wind velocity. The mirror structure is seen to be idealized as a second-order system with transfer function

$$F(s) = \frac{1}{I_{m_{xx}} s^2 + \beta s + C} = \frac{10^{-6}}{17.16 s^2 + 2.23 s + 975} \frac{\text{rad}}{\text{ft. lb.}}$$

b. Nature and Magnitude of Excitation Torques

The actual wind velocity distribution is unknown and largely unpredictable at the chosen solar furnace site. The presence of mountainous areas and artificial obstacles (such as the parabolic concentrator at not more than 250 ft. distant) renders the available micrometeorological data unapplicable.

We shall assume here that in the presence of turbulent flow

(a) the average wind velocity V_0 can be approximated by the analytical expression:

$$V_0 = V_{\infty} \left(1 - e^{-\frac{h}{h_0}} \right) \quad (1)$$

V_{∞} = velocity measured at altitude not influenced by the surface

h = altitude

h_0 = characteristic altitude of the air flow, representatively 20 to 30 ft.

(b) the fluctuation of wind velocity with respect to the average is stationary, random with known probability distribution (possibly function of the average value V_0).

(1) Steady State Wind Torque

Call H the altitude of the shaft, y the distance from the shaft, and p_y the pressure acting on a strip $L dy$, as shown on Figure 3. Then

$$p_y = p_h = C_D \frac{1}{2} \rho V_h^2$$

p = "pressure"

C_D = drag coefficient

ρ = density

V_h = velocity at altitude

with

$$V_h = V_{\infty} \left(1 - e^{-\frac{h}{h_0}} \right)$$

The elementary torque on the shaft is

$$d\tau = L p_y y dy = C_D \frac{1}{2} \rho V_{\infty}^2 \left(1 - e^{-\frac{h}{h_0}} \right)^2 L y dy.$$

The integration can be simplified by replacing the actual wind profile by its first-order approximation at the center:

$$V_y \approx \bar{V} + \frac{\partial V_h}{\partial h} y = \bar{V} + \frac{V_{\infty}}{h_0} e^{-\frac{H}{h_0}} y = \bar{V} + \mu y.$$

So that the total steady state wind torque is

$$\tau = C_D \frac{1}{2} \rho L \int_{-\frac{L}{2}}^{+\frac{L}{2}} (\bar{V} + \mu y)^2 y dy$$

$$\tau = \frac{1}{12} C_D \rho L^4 \bar{V} \frac{V_{\infty}}{h_0} e^{-\frac{H}{h_0}}$$

$$\tau = \frac{1}{12} C_D \rho L^4 \frac{V_{\infty}^2}{h_0} e^{-\frac{H}{h_0}} \left(1 - e^{-\frac{H}{h_0}} \right) \quad (2)$$

The ratio of this "wind gradient" torque to the one supplied by the average wind velocity at the center on one-half of the plate is of some interest.

$$\frac{\tau}{\frac{1}{2} C_D \rho \bar{V}^2 \frac{L^3}{8}} = \frac{4}{3} \frac{L}{h_0} \frac{e^{-\frac{H}{h_0}}}{\left(1 - e^{-\frac{H}{h_0}} \right)}$$

H = Altitude of shaft

h_0 = Characteristic of wind profile (See Eq. (1))

This relationship, put under the form

$$\frac{\tau}{\frac{1}{16} C_D \rho \bar{v}^2 L^3} = \frac{4}{3} \frac{L}{H} \frac{H}{h_o} \frac{e^{-\frac{H}{h_o}}}{1 - e^{-\frac{h}{h_o}}}$$

is represented on Fig. 37 for the largest $\frac{L}{H}$ value possible. $\frac{L}{H}$ is expected to be around 1.5 so that the actual gradient torques could easily be about 35% lower than represented.

The conclusion is that unless h_o is very small (say 5 to 15 ft) the gradient torque is extremely significant (20 to 40%) with respect to the aerodynamic torque acting on any half-portion of the heliostat mirror.

Numerical example on Eq. (2):

$$C_D = 1.10$$

$$\rho = 1.84 \times 10^{-3} \text{ slugs/ft}^3$$

$$L = 145 \text{ ft.}$$

$$V_\infty = 5 \text{ ft/sec}$$

$$h_o = 15 \text{ ft}$$

$$H = 75 \text{ ft}$$

$$\tau = 1035 \text{ lb. ft.}$$

with $V_\infty = 50 \text{ ft/sec } (\approx 34 \text{ mph})$

$$h_o = 35 \text{ ft}$$

$$\tau = 553,500 \text{ lb. ft.}$$

It is seen that, in the presence of moderate winds and reasonable gradients, the net torque is small compared with the shaft stiffness computed previously. The above 553,500 lb. ft. torque would cause a rigid-body rotation of the mirror of about 1.9' of arc with $C = 9.75 \times 10^8 \text{ lb. ft./rad.}$, or $17 \times 10^6 \text{ lb. ft./degree.}$

(2) Fluctuating Excitation Torques

It is our assumption that in addition to the average aerodynamic pressure accounted for in the preceding section, a fluctuating pressure \tilde{p} is applied to the mirror owing to the turbulent characteristics of the air flow. An approximation of the net fluctuating torque can be computed by subdividing the mirror area in "cells" of side Δ wherein the pressure is a stationary random function of time uncorrelated with the pressure fluctuations of any other cell.* The only assumption necessary is the shape of the distribution function of pressure.

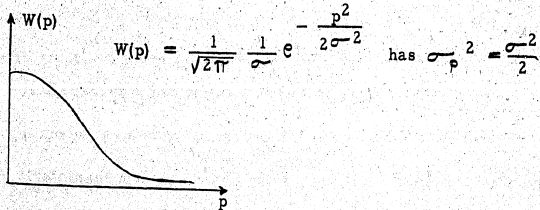
$W(\tilde{p}) d\tilde{p}$ is the probability that \tilde{p} will remain between p and $p + dp$ at any given time. Owing to the stationary characteristic assumed, such distribution is time-invariant and the time average properties can be immediately obtained from the distribution.

* It is to be noted that moderate scale correlation (5 to 25 ft) would increase the net fluctuating torque.

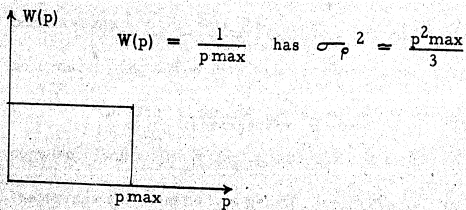
In particular, the variance is obtained by

$$\sigma_p^2 = \int_0^\infty \bar{p}^2 W(\bar{p}) \cdot d\bar{p}$$

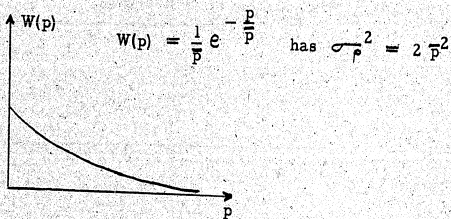
so that, for example the Gaussian Distribution



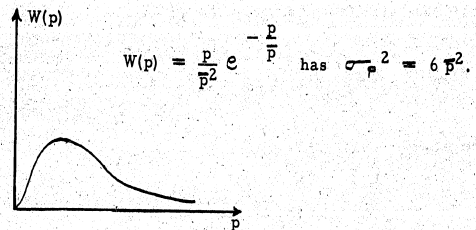
The "Equiprobable" distribution



The zero-order Poisson distribution



And the first-order Poisson distribution



From the preceding examples, it is plain that the nature of the assumed distribution $W(p)$ will not essentially change the conclusions for variances of the same order of magnitude.

A fluctuating pressure $\bar{p}(y)$ acting on a cell of dimensions λ^2 produces a force variance $\sigma_f^2(y) = \lambda^4 \sigma_p^2(y)$ and, since there are $\frac{L}{\lambda}$ such cells in the strip distance (y) from the shaft xx' , the variance of the total force acting on this strip is $\sigma_F^2(y) = L \lambda^3 \sigma_p^2(y)$ and thus the variance of the corresponding torque is

$$\sigma_\tau^2(y) = \left\{ L \lambda^3 \sigma_p^2(y) \right\} (n \lambda)^2$$

n = number of cells
 $n \lambda \approx y$

The total torque variance is, therefore

$$\sigma_\tau^2 = L \lambda^5 \sum_1^{L/\lambda} n^2 \sigma_p^2(n \lambda) \tag{3}$$

In particular, if $\sigma_p^2(y)$ is independent of y (uniform turbulence characteristics over the whole mirror surface),

$$\sigma_c^2 = L \lambda^5 \sigma_p^2 \sum_{n=1}^{\lambda} n^2 \approx \frac{L^4 \lambda^2 \sigma_p^2}{3} \quad (3')$$

using the approximation

$$\sum n^2 = \frac{n}{6} (n+1) (2n+1) \approx \frac{n^3}{3}$$

Another possible approach is to assume that σ_p^2 is a linear function following the velocity distribution across the height of the mirror

$$\begin{aligned} \sigma_p^2(n\lambda) &= \sigma_p^2 \left(1 + \frac{y}{H}\right) \\ \text{so that } \sigma_c^2 &= L \lambda^3 \sum_{n=1}^{\lambda} (n\lambda)^2 \sigma_p^2 \left(1 + \frac{n\lambda}{H}\right) \\ &\approx \frac{L^4 \lambda^2}{3} \sigma_p^2 + \frac{L \lambda^3}{H} \sigma_p^2 \sum_{n=1}^{\lambda} (n\lambda)^3 \approx \\ \sigma_c^2 &\approx L^4 \lambda^2 \sigma_p^2 \left[\frac{1}{3} + \frac{2}{7} \frac{L}{H} \right] \quad (4)* \end{aligned}$$

Numerical Example:

$$L = 145 \text{ ft.}$$

$$\lambda = 5 \text{ ft.}$$

* Using the approximation $\sum n^3 \approx \frac{2n^4}{7}$ for $n \approx 10$ to 14.

$$H = 75 \text{ ft.}$$

$$\sigma_p = .5 \text{ lb/sq.ft.*}$$

$$\sigma_c \approx 49,400 \text{ lb.ft.}$$

III. Response to Random Torque Excitation

The input-output relationship of the torsional system being characterized by the transfer function

$$F(s) = \frac{1}{I s^2 + \theta s + C}$$

the power spectrum of the output is

$$\begin{aligned} \theta(s) &= \{F(s) \cdot F(s)^*\} \tau(s) \\ \theta(s) &= \text{Power spectrum of output (angle)} \\ \tau(s) &= \text{Power spectrum of input (torque)} \end{aligned}$$

For real excitations $s = j\omega$ and $s^* = -j\omega$ so that

$$\theta(\omega) = [F(j\omega)]^2 \tau(\omega)$$

* Corresponding roughly to a 15 mph "gustiness".

From the previously determined torque fluctuation and Parseval's theorem*

$$\sigma_{\tau}^2 = \int_0^{\omega_c} \tau(\omega) d\omega \quad (5)$$

ω_c = Maximum frequency present in the torque "signal".

One possible view is that the torque signal is "white", i.e., carries equal spectral power density at all frequencies between 0 and ω_c ; then Eq. (5) becomes

$$\tau(\omega) \equiv \tau_0(\omega) = \frac{\sigma_{\tau}^2}{\omega_c}$$

and

$$\sigma_{\theta}^2 = \frac{\sigma_{\tau}^2}{\omega_c} \int_0^{\omega_c} \left[\frac{1}{(C - I\omega^2) + j\beta\omega} \right]^2 d\omega$$

The major portion being supplied in the presence of small damping by the close-to-resonance components ω_0 .

$$\sigma_{\theta}^2 \approx \frac{\sigma_{\tau}^2}{C^2} \frac{\omega_0}{\omega_c} \int_0^{\omega_c} \frac{d \left(\frac{\omega}{\omega_0} \right)}{\left[\left(\frac{\omega}{\omega_0} \right)^2 - 1 \right]^2 + 4\beta^2 \left(\frac{\omega}{\omega_0} \right)^2}$$

$$\sigma_{\theta}^2 = \frac{\pi}{4C^2\beta} \frac{\omega_0}{\omega_c} \sigma_{\tau}^2 \quad (6)$$

* H. S. Tsien, Engineering Cybernetics, McGraw-Hill Book Company, 1954, p. 116.

where

$$\beta = \frac{\xi}{\sqrt{C/I}}$$

(damping ratio) $\omega_0 = \sqrt{C/I}$

Equation (6) can be transformed in

$$\sigma_{\theta}^2 = \frac{\pi}{2I\beta\omega_0^2} \frac{\sigma_{\tau}^2}{\omega_c} \text{ with } \omega_0 = \sqrt{C/I}$$

Numerical Example:

$$I = 17.16 \times 10^6 \text{ lb-ft-sec}^2$$

$$\beta = 2.23 \times 10^6 \text{ lb-ft-sec}$$

$$C = 9.75 \times 10^8 \text{ lb-ft-rad}^{-1}$$

$$\omega_c = 12.5 \text{ rad/sec (2 cps)}$$

$$\sigma_{\tau} = 4.94 \times 10^4 \text{ lb.ft.}$$

$$\omega_0 = 7.44 \text{ rad/sec (1.2 cps)}$$

$$\sigma_{\theta} = 1.3' \text{ arc R.M.S.}$$

The same figure with a turbulent cell size of 15 ft, with wind pressure fluctuation of 1 lb/sq. ft., R.M.S., would reach about 2.34' arc R.M.S.

When interpreting such figures, it should be remembered that

- (1) Correlation between adjacent cells would substantially increase the fluctuation,

(2) The fluctuation is added to the steady-state displacement and to any elastic deformation of the plate itself,

(3) The fluctuation would again be substantially increased if the excitation torque would contain substantial power concentration in the resonant domain of the plate-shaft combination.

On the other hand, the damping used here did neglect structural damping in the plate and shaft itself and may be considered on the low side.

IV. Conclusions

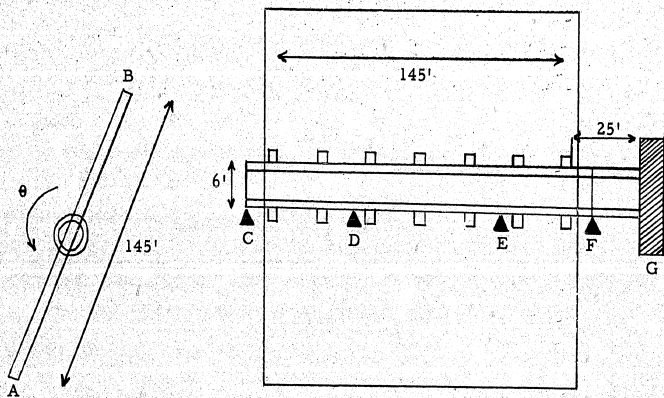
Under conservative wind gradient and turbulence estimates, the steady state and R.M.S. rigid-body oscillations of a 145 ft x 145 ft heliostat mirror are shown to be easily of the order of magnitude of the required construction tolerance of ± 1 minute of arc.

This situation is apparently due to the relatively poor stiffness characteristics of the rotational support and possibly to the absence of structural damping. In the presence of the close position tolerances, it is suggested that artificial damping and a more rational support method be used.

It is believed to be necessary to support the mirror frame at several points along its height so that not only considerable torsional

stiffness but also lower bending deformations would result. Figure 39 shows one possible arrangement. Appropriate damping can easily be inserted in the driving wheel shafts.

FIGURE 34



TORSIONAL SCHEMATIC

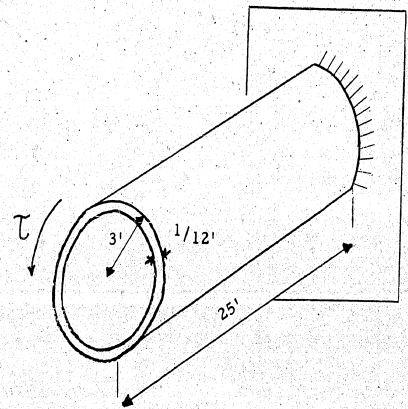
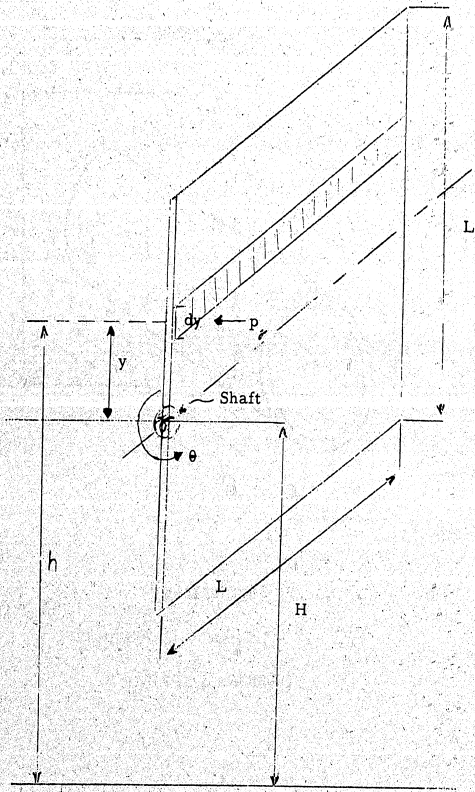


FIGURE 35

TORSIONAL SPRING

FIGURE 36



NOTATIONS FOR STEADY STATE WIND TORQUE

FIGURE 37

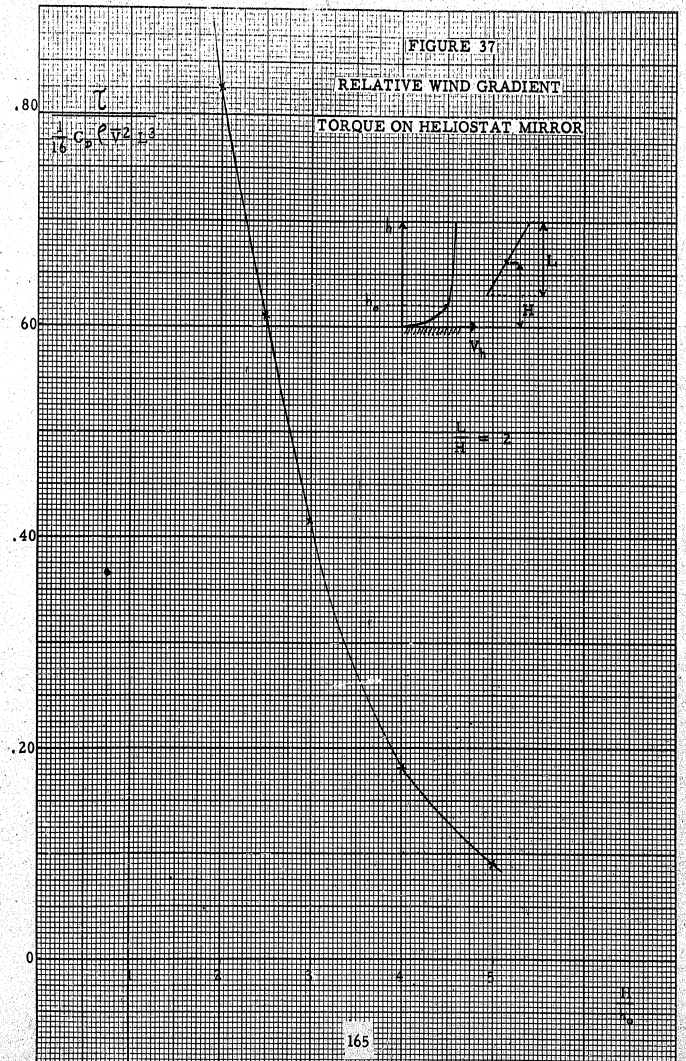
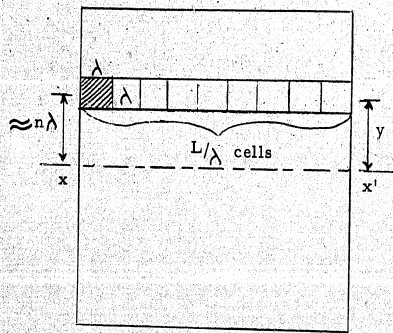
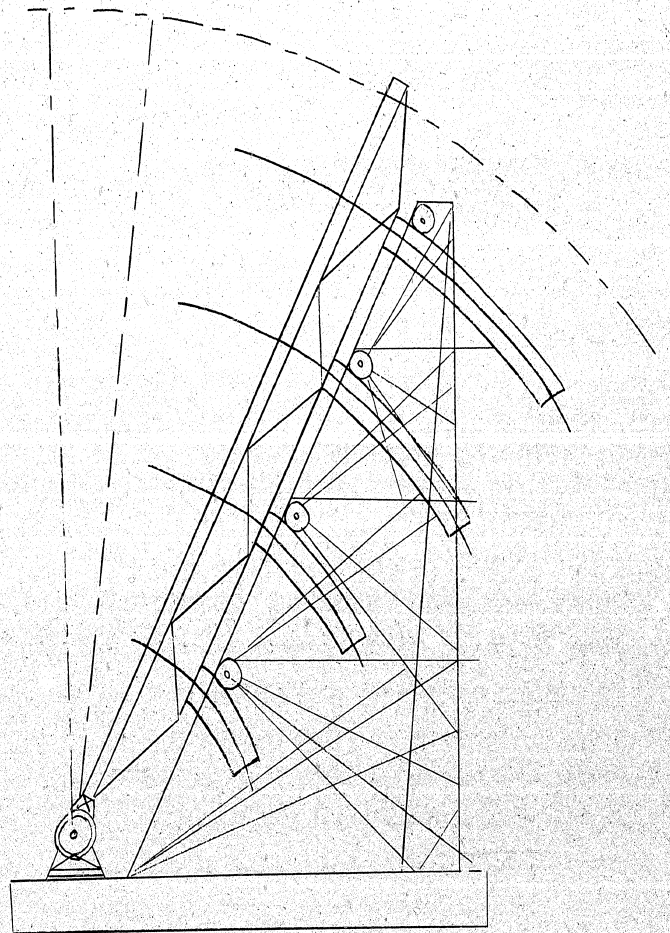


FIGURE 38



LOCATION OF UNCORRELATED TURBULENCE CELLS

FIGURE 39



MULTIPLE SUPPORT HELIOSTAT STRUCTURE

CHAPTER 9

TRANSIENT TEMPERATURE DISTRIBUTION
IN A THERMALLY IRRADIATED BODY
WITH VARIABLE HEAT-TRANSFER COEFFICIENT

STAT



ABSTRACT

Two methods, one numerical and the other graphical, are presented for the calculation of transient temperature distribution in a thermally irradiated body with heat losses which are non-linear in temperature dependence. The numerical method is derived on the basis of the method of superposition and makes use of analytical solutions for the case where the net radiant intensity absorbed is constant. The graphical method is based on that of Schmidt. Although the graphical method is simple and convenient, the numerical method is recommended for better accuracy.

I. Introduction

In the calculation of transient temperature distribution of a body exposed to thermal radiation, the simultaneous existence of convective and re-radiation heat losses has to be taken into consideration. Terms accounting for these heat losses, in particular re-radiation loss, are non-linear in temperature dependence. This non-linear relationship not only results in great difficulties in obtaining an analytical solution of a particular problem but also prohibits the use of the method of superposition by the addition of known solutions available in the literature.

Because of the low temperature attained with incident radiation of low intensity, the above problem can be linearized without undue error by the use of an average over-all heat-transfer coefficient to account for the heat losses. However, for radiation of higher intensity, this technique is quite inadequate because of larger variations in the value of the over-all heat-transfer coefficient. Two methods, one numerical and the other graphical, are presented in this report for the solution of such a problem.

The numerical method is derived on the basis of the method of superposition and makes use of analytical solutions for the case where the net radiant intensity absorbed is constant. The validity of this method is further demonstrated by comparing the results obtained therefrom for the case of constant heat-transfer coefficient with those of the

exact solution. This method is also illustrated by an example where both emissivity and convective heat-transfer coefficient are functions of temperature.

The use of the graphical method --- a modified Schmidt method --- is illustrated by an example. For better accuracy, however, the numerical method is recommended.

II. Results

Two methods, one numerical and the other graphical, are presented below for the solution of transient temperature distribution of a thermally irradiated body when the heat losses due to convection and re-radiation are non-linear in temperature dependence. Although the discussion will be devoted mainly to a simple case of a one-dimensional, semi-infinite, opaque solid with constant density, thermal conductivity, specific heat and reflectivity, exposed to a constant ambient temperature and to a thermal radiation of constant intensity with no resulting evaporation, melting, mass transfer and chemical reaction, all these restrictions are not necessary. The methods can be used to deal with more general problems.

a. Numerical Method

(1) Theoretical Considerations

Fig. 40a shows a thermally irradiated, semi-infinite solid, with a constant absorbed intensity I_0 and an over-all heat loss $h\Delta T$,

where h is the variable heat-transfer coefficient and ΔT is the difference between the instantaneous values of surface and ambient temperature. Because of the heat loss, the net absorbed intensity I would vary with time as is shown qualitatively therein.

The model used in the numerical method is given in Fig. 40b. There, the continuous variation of the net absorbed intensity is represented by a broken curve. The temperature distribution at any instant t is then computed by the superposition of the results obtained in the following events:

(a) From the initial instant of irradiation till the time in question, there is a constant absorbed intensity of $I_0 - \Delta I_1$.

(b) From the time t_1 , the instant when the intensity suddenly changes from $I_0 - \Delta I_1$ to $I_0 - \Delta I_2$, to the time in question, there is a constant "negatively absorbed" intensity (or constant heat loss) of $\Delta I_2 - \Delta I_1$.

(c) From the time t_2 , the instant when the intensity suddenly changes from $I_0 - \Delta I_2$ to $I_0 - \Delta I_3$, to the time in question, there is another constant heat loss of $\Delta I_3 - \Delta I_2$.

Etc., etc., till the time in question.

Since solutions for the case of irradiation at a constant net intensity are readily available, the superposition method suggested above permits the computation of the transient temperature distribution at any instant.

For a given problem, however, the curve of the net absorbed intensity versus time is at first unknown. In other words, the question still remains as how to find ΔI_1 , ΔI_2 , etc. This can be achieved by any familiar method of successive approximations; for example, the first approximation of ΔI_1 is equal to the over-all heat loss corresponding to conditions attained at a time equal to $t_1/2$ due to a constant net absorbed intensity at the initial instant of irradiation. If necessary, its value can be improved by computing a new heat loss at time $t_1/2$ corresponding to a constant absorbed intensity corrected by the first approximation. Similarly, the first approximation of ΔI_2 is equal to the over-all heat loss corresponding to conditions attained at a time equal to $(t_1 + t_2)/2$ due to an absorbed intensity of $I_0 - \Delta I_1$; the first approximation of ΔI_3 is equal to the over-all heat loss corresponding to condition attained at a time equal to $(t_2 + t_3)/2$ due to an absorbed intensity of $I_0 - \Delta I_1$ superimposed to those attained at a time equal to $(t_2 + t_3)/2 - t_1$ due to an absorbed intensity of $\Delta I_1 - \Delta I_2$, etc. These values can further be improved by successive approximations, although this has not been found necessary in the work to be described below.

(2) A Special Case

As it was pointed out earlier, the present numerical method is derived on the basis of the method of superposition and makes use of

analytical solutions for the case where the net radiant intensity absorbed is constant. To further demonstrate the validity of this method, the results obtained therefrom for a particular example are compared with those of the exact solution.

The example chosen is the case of a one-dimensional, semi-infinite, opaque solid, exposed to a thermal radiation of constant intensity and losing heat to a constant-temperature surrounding with a constant heat-transfer coefficient. The solid is further assumed to have constant physical properties, to be homogeneous throughout at all times, and to be initially at a uniform temperature equal to the ambient temperature. The equation and its boundary conditions for such a problem are as follows:

$$\frac{\partial T}{\partial t} = \alpha \frac{\partial^2 T}{\partial x^2} \quad (1)$$

$$T(x, 0) = T_a \quad (2)$$

$$k \frac{\partial T}{\partial x}(0, t) = -I_0 + h [T(0, t) - T_a] \quad (3)$$

$$T(\infty, t) = T_a \quad (4)$$

The symbols are defined in Appendix I.

Solutions of this problem with either zero or constant heat-transfer coefficient can be easily obtained by standard techniques including the method of Laplace Transformation. Because of space limitations, only the final results are given below:

(a) Zero Heat-Transfer Coefficient

$$\frac{k(T - T_a)}{I_0 \sqrt{\alpha t}} = \frac{2}{\sqrt{\pi}} \exp\left(-\frac{x^2}{4\alpha t}\right) - \frac{x}{\sqrt{\alpha t}} \operatorname{erfc}\left(\frac{x}{2\sqrt{\alpha t}}\right) \quad (5)$$

(b) Constant Heat-Transfer Coefficient

$$\frac{k(T - T_a)}{I_0 \sqrt{\alpha t}} = \left(\frac{h\sqrt{\alpha t}}{k}\right)^{-1} \left\{ \begin{array}{l} \operatorname{erfc}\left(\frac{x}{2\sqrt{\alpha t}}\right) - \\ \exp\left[\frac{h\sqrt{\alpha t}}{k} \left(\frac{x}{\sqrt{\alpha t}} + \frac{h\sqrt{\alpha t}}{k}\right)\right] \\ \operatorname{erfc}\left(\frac{x}{2\sqrt{\alpha t}} + \frac{h\sqrt{\alpha t}}{k}\right) \end{array} \right\} \times \quad (6)$$

where

$$\operatorname{erfc}\left(\frac{x}{2\sqrt{\alpha t}}\right) = 1 - \operatorname{erf}\left(\frac{x}{2\sqrt{\alpha t}}\right) = \frac{2}{\sqrt{\pi}} \int_{x/2\sqrt{\alpha t}}^{\infty} \exp(-v^2) dv \quad (7)$$

For the case of zero heat-transfer coefficient, there are two dimensionless groups; viz., $k(T - T_a) / I_0 \sqrt{\alpha t}$ and $x/\sqrt{\alpha t}$. For the case of constant heat-transfer coefficient, there is a third dimensionless group, $h\sqrt{\alpha t}/k$. Various other dimensionless groups can, of course, be formed by combining the ones given above.

Curves showing the solution for the case of zero heat-transfer coefficient may be found in the literature, e.g., reference⁽¹⁾. The solution for the case of constant heat-transfer coefficient is shown in Figures 41, 42 and 43.

Because of the presence of more than one variable of physical interest in the above dimensionless groups, these groups, or a combination of them, cannot be conveniently used to give a clear graphical picture of the transient temperature distribution. Three figures are thus presented to show separately the effects of some of the important variables. Fig. 41 shows clearly the effect of heat-transfer coefficient on the temperature attained at a given position and time, Fig. 42 shows the temperature distribution at any instant for a given heat-transfer coefficient, and Fig. 43 shows the transient temperature change at a given position and for a given heat-transfer coefficient. It is to be noted that two new dimensionless groups, $h(T - T_a)/I_0$ and hx/k have been used in Fig. 43.

Fig 44 shows the transient temperature change at two positions for an arbitrary value of the heat-transfer coefficient. The change in surface temperature for zero value of the heat-transfer coefficient is also included. Shown for comparison are also points calculated by the numerical procedure outlined in the Theoretical Considerations*. The agreement indicated therein further demonstrates the validity of the method.

* The first few steps of the calculation are shown in Appendix II.

In Fig. 45 is shown the transient variation of the net radiant intensity absorbed obtained from the exact solution for the same problem. The dashed line shows the variation obtained in the numerical method.

Although a unit of centimeter has been indicated in Figs. 44 & 45, it is to be pointed out that any unit of length can be used in the interpretation of the results, so long as all the variables are expressed in terms of a consistent set of units.

(3) A Numerical Example

The numerical method presented here has been used to calculate the transient temperature distribution of a semi-infinite solid of tungsten, until the surface begins to melt. The emissivity is assumed to vary directly with the absolute temperature and the heat-transfer coefficient due to natural convection is assumed to vary directly with the one-third power of the temperature difference according to a correlation obtained for steady-state processes. The computed results are shown in Fig. 46, which also includes a tabulation of values of the physical properties and of the incident radiant intensity absorbed. The temperature rise is indicated for three different positions, with that corresponding to the case of zero heat loss shown by the dashed curves. Because of the small ratio of heat loss to radiant intensity absorbed,

even when the surface starts to melt, the effect of heat loss on the temperature variation is rather small. This effect, of course, is even smaller at a position farther away from the surface.

Fig. 47 shows, for the case corresponding to Fig. 46, the transient variation of net radiant intensity absorbed, together with that of heat losses due to natural convection and re-radiation. Except during the first second of irradiation, the loss due to natural convection is negligible as compared with that due to re-radiation.

The broken curve in Fig. 47 shows the step changes in the net radiant intensity absorbed used in the calculation of the transient temperature distribution.

b. Graphical Method

The graphical method described below is based on that of Schmidt⁽²⁾. For the special case of a one-dimensional, semi-infinite opaque solid, the boundary condition at the irradiated surface is

$$-k \left(\frac{\partial T}{\partial x} \right)_s = I_0 - h_c (T_s - T_a) - \sigma \epsilon T_s^4 \quad (8)$$

or

$$\left(\frac{\partial T}{\partial x} \right)_s = \frac{T_s - (T_a - I_0/h_c - \sigma \epsilon T_s^4/h_c)}{k/h_c} \quad (9)$$

As shown in Fig. 48, the numerator in the right-hand member of Eq. (9) is plotted as ordinate at a distance k/h_c from the surface. A straight

line joining points A and B gives the slope $\left(\frac{\partial T}{\partial x}\right)_s$ and the ordinate at the intersection with a fictitious plane at a distance of $-0.5 \Delta x$ from the surface is designated as T^* . As an approximation, $\left(\frac{\partial T}{\partial x}\right)_s$ is replaced by the chord slope $(T^* - T_{0.5}) / \Delta x$. Then, according to the Schmidt method, a heat balance on the slice from the irradiated surface to plane "1", which is at a distance Δx away, gives

$$T'_{0.5} = (T^* + T_{1.5}) / 2 \quad (10)$$

where $T'_{0.5}$ is the new temperature in plane "0.5" at a time Δt later. Here Δx and Δt are related as follows:

$$(\Delta x)^2 / \alpha \Delta t = 2 \quad (11)$$

Heat balances for the interior layers give further

$$T'_{1.5} = (T_{0.5} + T_{2.5}) / 2 \quad (12)$$

$$T'_{2.5} = (T_{1.5} + T_{3.5}) / 2 \quad (13)$$

Fig. 48 illustrates the use of the graphical method for a semi-infinite solid originally at a uniform temperature equal to the ambient temperature. In order to simplify the figure, the values of k/h_c , T_a and I_0/h_c are assumed to be constant. These restrictions are, of course, not necessary.

Although the graphical method presented here is simple and convenient, the numerical method is recommended when better accuracy is desired.

References

1. Hottel, H. C. and Gardon, R., "Temperatures Attained in Wood Exposed to High Intensity Thermal Radiation", Technical Report No. 3, Fuels Research Laboratory, Massachusetts Institute of Technology, 1953.
2. McAdams, W. H., "Heat Transmission", McGraw-Hill Book Co., Inc., New York, 1954, pp 48-49,

or

Schmidt, E., Forsch. Gebiete Ingenieurw., Vol. 13 (1942), pp 177-184.

APPENDIX I

Nomenclature

h	Heat-transfer coefficient
I	Net absorbed radiant intensity
k	Thermal conductivity
q	Heat loss
t	Time
T	Absolute temperature
x	Distance from irradiated surface
α	Thermal diffusivity
ϵ	Emissivity
σ	Stefan-Boltzmann constant

Subscripts:

o	Refers to incident radiation
1, 2, ...	Refer to values at successive instants in the numerical method and at successive planes in the graphical method
a	Refers to ambient condition
c	Refers to convection
r	Refers to re-radiation
s	Refers to irradiated surface

Superscript * refers to condition at a fictitious plane

Primes indicate values at successive instants in the graphical method.

APPENDIX II

Sample Calculations

The numerical method presented in this report has been used to calculate the transient temperature distribution for the special case considered in the Results. The first few steps of the method are given below.

According to Eq. (5), the surface temperature for the case of zero heat-transfer coefficient is computed as follows:

$$\frac{\sqrt{\pi}}{2} \frac{k(T_s - T_a)}{I_o} = \sqrt{\alpha t} \quad (\text{II-1})$$

Let $\alpha t_1 = 0.1 \text{ cm}^2$ and $h/k = \sqrt{\pi}/2 \text{ cm}^{-1}$. Then,

$$\frac{\Delta I_1}{I_o} = \frac{h(T_s - T_a)}{I_o} \text{ at } \alpha t = 0.05 \text{ cm}^2$$

or, with Eq. (II-1),

$$\frac{\Delta I_1}{I_o} = \frac{2}{\sqrt{\pi}} \frac{h}{k} \sqrt{0.05} = 0.2236$$

Hence, the temperature rise in terms of $\frac{\sqrt{\pi}}{2} \frac{k(T_s - T_a)}{I_o}$ at a time corresponding to a value of 0.1 cm^2 for αt_1 and due to a net absorbed intensity of $I_o - \Delta I_1$ is equal to

$$\left(1 - \frac{\Delta I_1}{I_o}\right) \sqrt{\alpha t_1} = 0.7764 \sqrt{0.1} = 0.2455$$

Next, the surface temperature rise at $\alpha t_2 = 0.2 \text{ cm}^2$ is to be calculated. At a value of αt equal to $(0.1 + 0.2)/2 \text{ cm}^2$ or 0.15 cm^2 , the net rise in terms of $\frac{\sqrt{\pi}}{2} \frac{k(T_s - T_a)}{I_0}$ is

$$\left(1 - \frac{\Delta I_1}{I_0}\right) \sqrt{\alpha t} = 0.7764 \sqrt{0.15} = 0.3002.$$

Hence,

$$\frac{\Delta I_2}{I_0} = \frac{h(T_s - T_a) \text{ at } \alpha t = 0.15 \text{ cm}^2}{I_0} = 0.3002.$$

At $\alpha t_2 = 0.2 \text{ cm}^2$, the net rise in terms of $\frac{\sqrt{\pi}}{2} \frac{k(T_s - T_a)}{I_0}$ is then the sum of the following two terms:

$$(1) \text{ Rise due to } I_0 - \Delta I_1 = \left(1 - \frac{\Delta I_1}{I_0}\right) \sqrt{\alpha t_2} \\ = 0.7764 \sqrt{0.2} = 0.3472$$

$$(2) \text{ Rise due to } \Delta I_1 - \Delta I_2 = \left(\frac{\Delta I_1 - \Delta I_2}{I_0}\right) \sqrt{\alpha(t_2 - t_1)} \\ = (0.2236 - 0.3002) \sqrt{0.1} = -0.02422$$

or, the net rise is the difference between 0.3472 and 0.02422 or 0.3230.

Next, the surface temperature rise at a time corresponding to a value of 0.3 cm^2 for αt_3 is to be calculated. At $\alpha t = (0.2 + 0.3)/2 = 0.25 \text{ cm}^2$, the net rise in terms of $\frac{\sqrt{\pi}}{2} \frac{k(T_s - T_a)}{I_0}$ is the sum of the following:

$$(1) \left(1 - \frac{\Delta I_1}{I_0}\right) \sqrt{\alpha t} = 0.7764 \sqrt{0.25} = 0.3882$$

$$(2) \left(\frac{\Delta I_1 - \Delta I_2}{I_0}\right) \sqrt{\alpha(t - t_1)} = -0.0766 \sqrt{0.15} = -0.02965$$

or 0.3585.

Thus,

$$\frac{\Delta I_3}{I_0} = \frac{h(T_s - T_a) \text{ at } \alpha t = 0.25 \text{ cm}^2}{I_0} = 0.3585$$

and the net temperature rise at $\alpha t_3 = 0.3 \text{ cm}^2$ is as follows:

$$\frac{\sqrt{\pi}}{2} \frac{k(T_s - T_a)}{I_0} = \left(1 - \frac{\Delta I_1}{I_0}\right) \sqrt{\alpha t_3} + \left(\frac{\Delta I_1 - \Delta I_2}{I_0}\right) \sqrt{\alpha(t_3 - t_1)} \\ + \left(\frac{\Delta I_2 - \Delta I_3}{I_0}\right) \sqrt{\alpha(t_3 - t_2)} = 0.3722.$$

Eq. (5) is also used to calculate the temperature rise at any position and time. For convenience, it is written as follows:

$$\frac{\sqrt{\pi}}{2} \frac{k(T - T_a)}{I_0} = \sqrt{\alpha t} \exp\left(-\frac{x^2}{4\alpha t}\right) - \frac{\sqrt{\pi}}{2} x \operatorname{erfc}\left(\frac{x}{2\sqrt{\alpha t}}\right) \quad (\text{II-2})$$

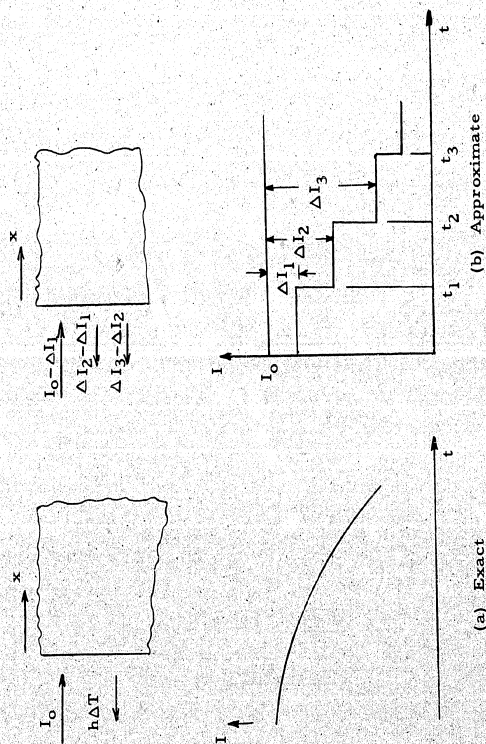
For $x = 0.4/\sqrt{\pi} \text{ cm}$ and $\alpha t_1 = 0.1 \text{ cm}^2$, the right-hand side of Eq. (II-2) is equal to 0.1558. Because of the heat loss, the net rise here is

$$\frac{\sqrt{\pi}}{2} \frac{k(T - T_a)}{I_0} = \left(1 - \frac{\Delta I_1}{I_0}\right) (0.1558) \\ = 0.7764 \times 0.1558 = 0.1210.$$

Similarly, at $x = 0.4 / \sqrt{\pi}$ cm and $\alpha t_2 = 0.2$ cm², the right-hand side of Eq. (II-2) is 0.2753. Thus, the net temperature rise at this instant is

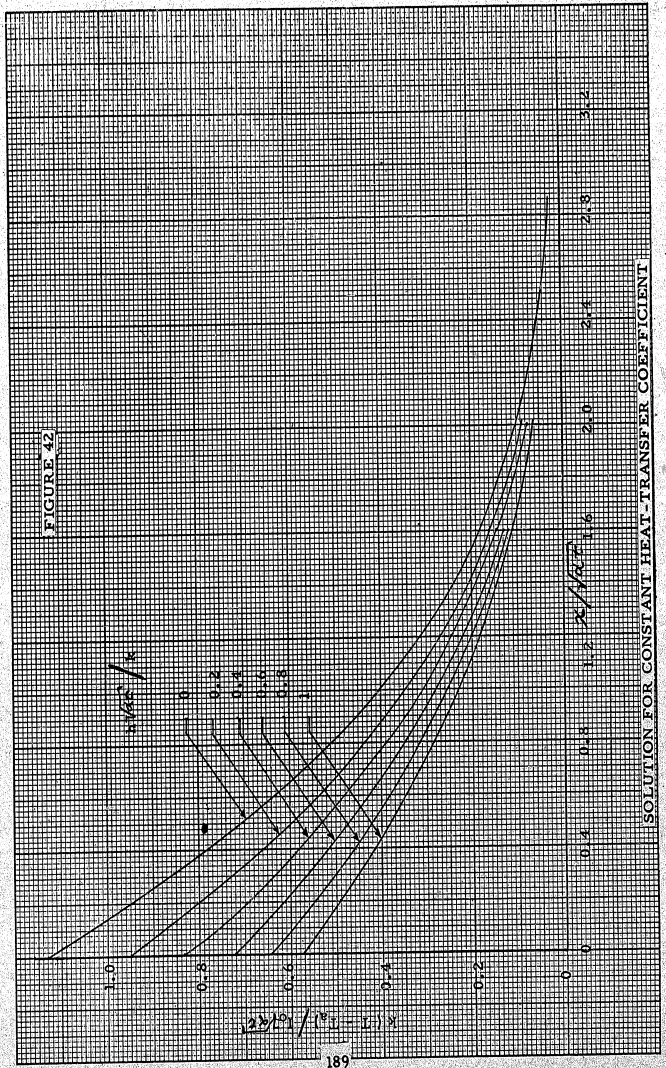
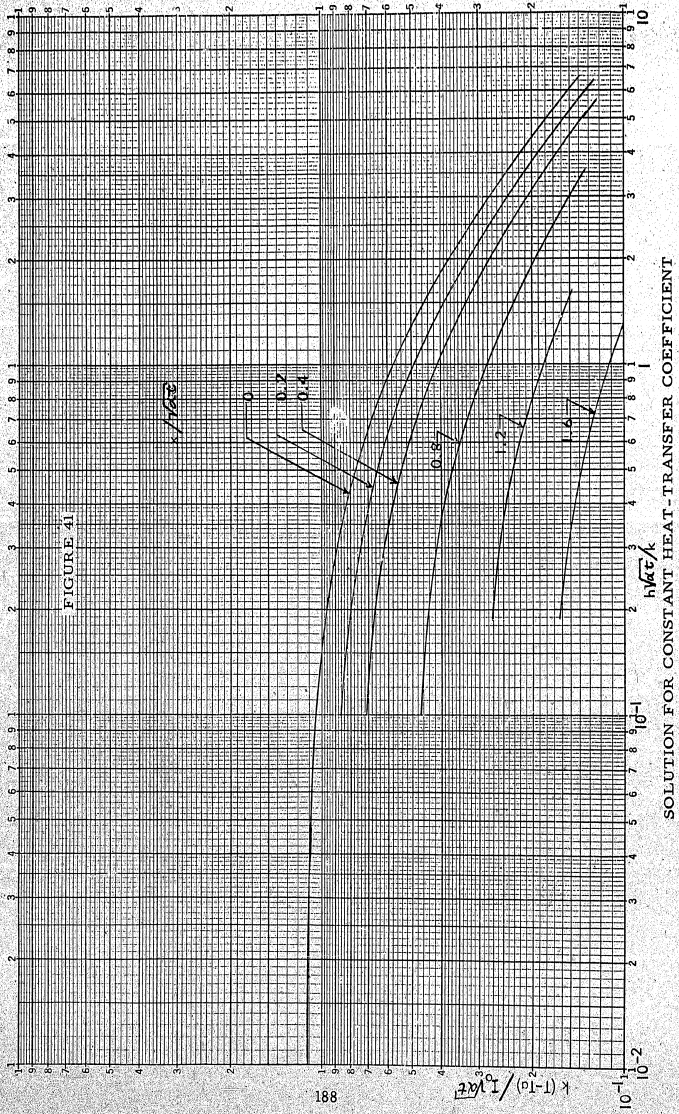
$$\frac{\sqrt{\pi}}{2} \frac{k(T - T_a)}{I_0} = \left(1 - \frac{\Delta I_1}{I_0}\right) (0.2753) + \left(\frac{\Delta I_1 - \Delta I_2}{I_0}\right) (0.1558)$$

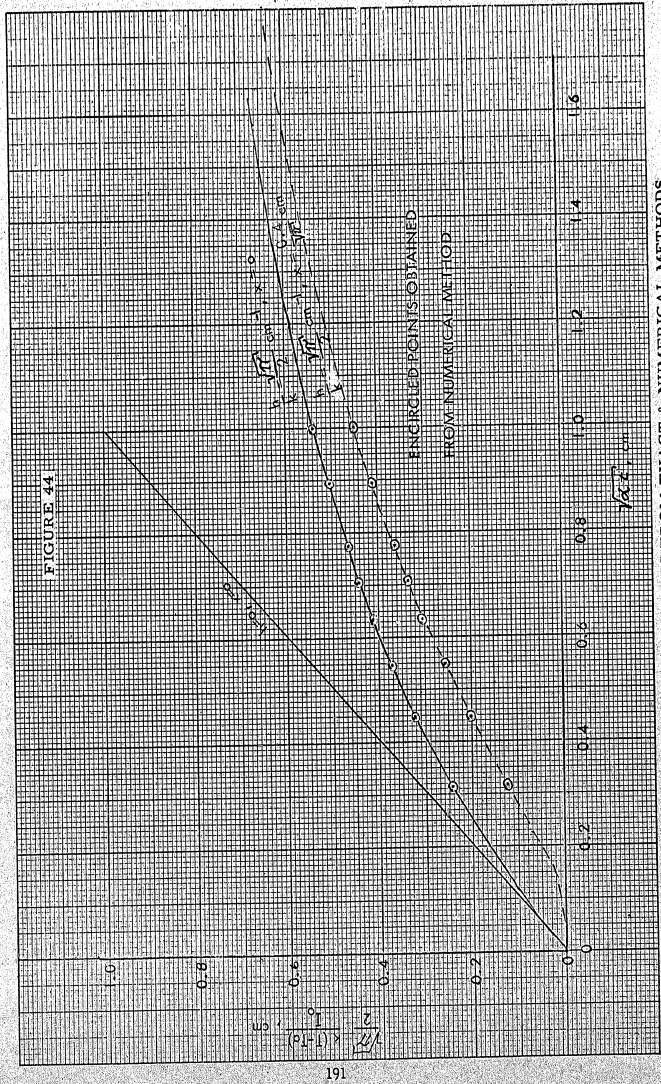
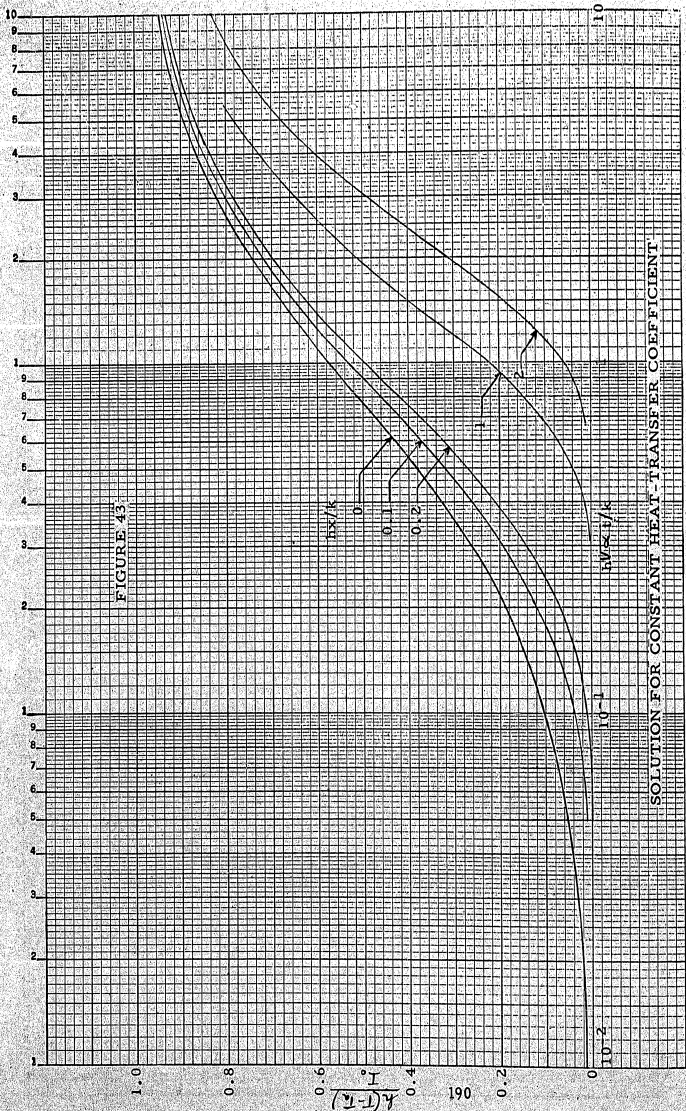
= 0.2017.

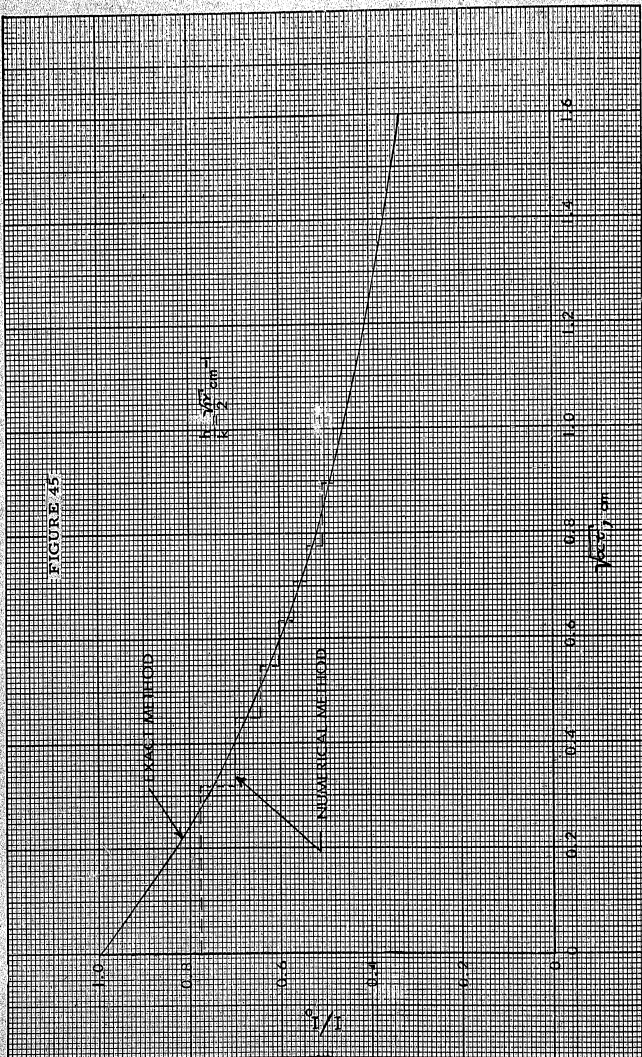


MODEL USED IN THE NUMERICAL METHOD

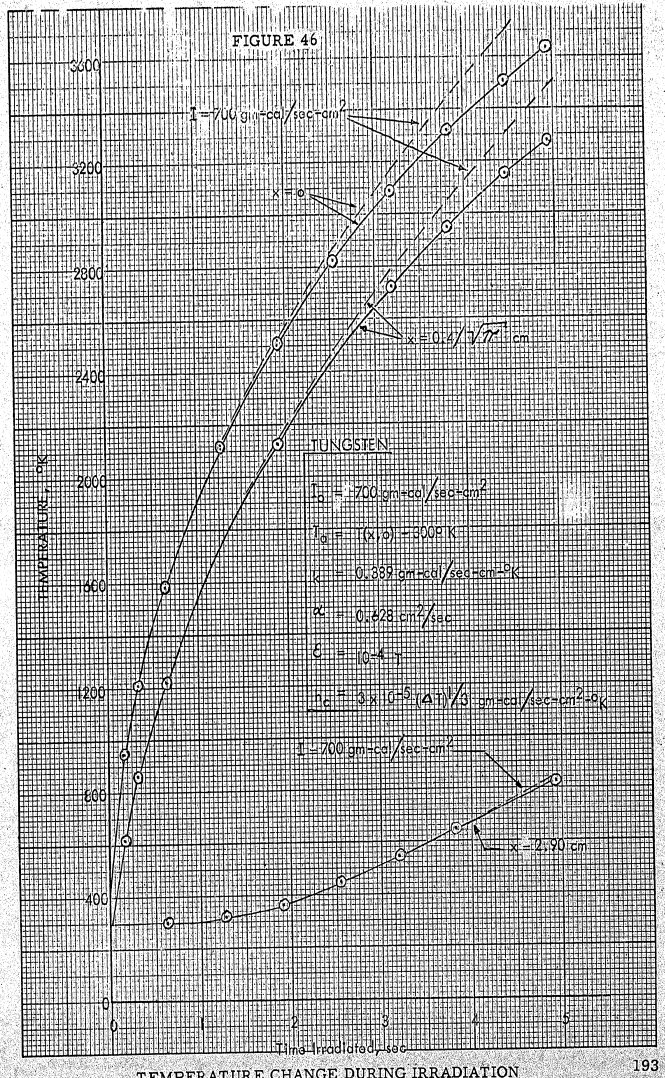
FIGURE 40







COMPARISON OF RESULTS FROM EXACT & NUMERICAL METHODS



TEMPERATURE CHANGE DURING IRRADIATION

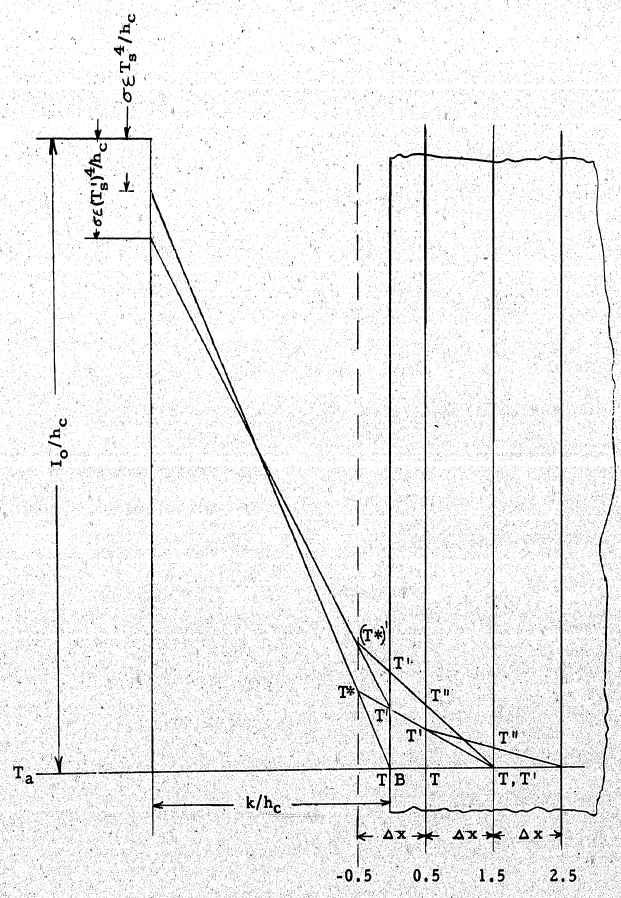
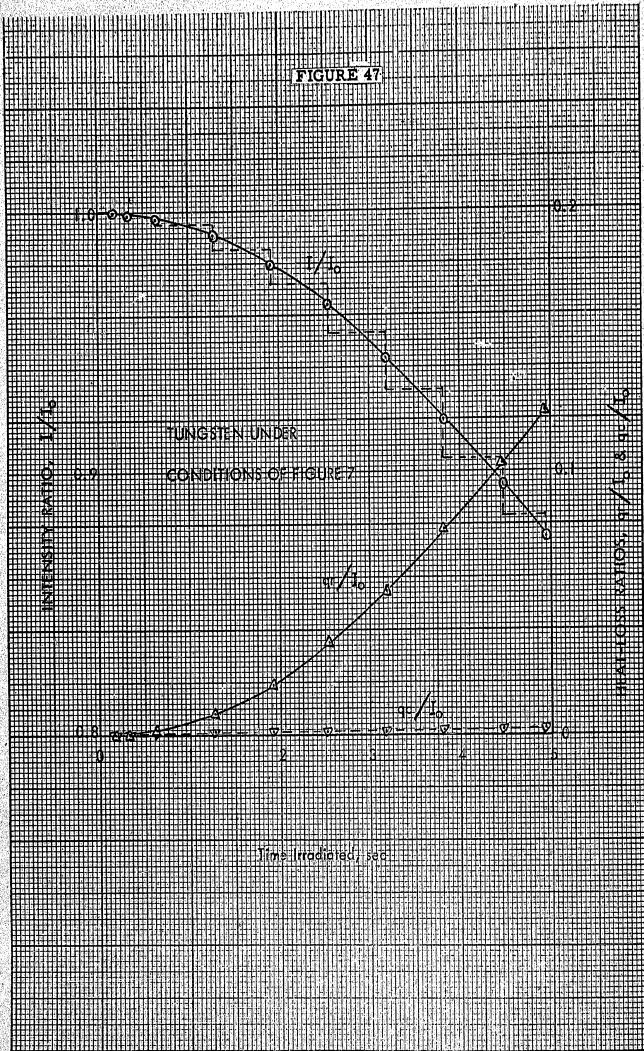


FIGURE 48

CHAPTER 10.

A SOLAR FURNACE USING
A HORIZONTAL HELIOSTAT ARRAY

STAT



ABSTRACT

A two-component solar furnace, condenser-heliostat combination, is described in which the condenser faces downward at 30° towards a heliostat comprised of numerous rows of plane mirrors mounted on a horizontal turntable. It is shown that for a South-facing condenser, and by limiting the angle of the final flux beam to 30° below the horizontal, the rows of heliostat mirrors may be mounted so they overlap, resulting in a reduction of the edge losses occurring when the heliostat mirrors are all held in a single plane. The overall size of the heliostat turntable is calculated for a 6-hour workday throughout the year, and a suggestion is made for using the heliostat control mechanism to provide shutter action. The saving in flux possible by the elimination of an independent shutter is estimated at about eight percent.

I. Introduction

The design for a solar furnace presented here has been developed as a study to overcome some of the less desirable features in the present design of the Department of Defense solar furnace to be built near Cloudcroft, New Mexico. Some of these objectionable features are:

- a. The required construction of a very large movable structure which must be tilted and rotated with considerable accuracy.
- b. The required construction of several additional movable structures.
- c. The horizontal direction of the final flux beam,
and
- d. The lack of protection of the optical elements from the weather.

The first of these objectionable features will make the furnace more difficult and expensive to construct when windy weather is taken into account. The horizontal direction of the flux beam will limit the usefulness of the furnace for metallurgical work. The last of the undesirable features mentioned may limit the use of the furnace after storms of sleet, snow, hail, etc.

II. The Condenser and Its Housing

In the production of high temperature alloys and ceramics, heat flux incident from above is a distinct advantage, if not a necessity. If an angle of 30° is sufficient for the purposes anticipated in alloying

studies, then this proposed solar furnace may be made in a simple manner. If a larger angle of incidence is required, the design becomes more complicated.

Since the design calls for no large movable structures aboveground level, wind load problems are reduced to a minimum. One tall stationary building is required, however, to house the condenser mirror with space enough unused to house all the laboratories, shops, offices, etc., that may be required. This single tall building, except for its open front, is in no way unusual and might be constructed in the manner of factory buildings of steel frame and corrugated Transite walls.

The condenser mirror, as previously stated, is housed in the single central building, and thus protected from the weather. Since it faces slightly downward, it is somewhat protected from dust. The heliostat mirrors, as shown later, are mounted in long rows and may be faced downward when not in use so they too are somewhat protected. If facing the heliostat mirrors downward is not sufficient protection, a low metal shed structure might be constructed to roll over the entire heliostat since it will be at ground level.

Figure 49 indicates the general scheme of the furnace.

The tall building, facing south, carries the condenser just under its roof, facing slightly downward toward the heliostat mirror. The height of the condenser mirror above ground depends on the choice of

angle of the final flux beam with the horizontal. For the 30° angle, a building 58 feet by 105 feet by 142 feet high would accommodate not only the mirror but a spectrographic laboratory directly behind the center of the mirror, and numerous working spaces below the mirror. In any case, the condenser mirror should be mounted high enough so that the heliostat mirror may be constructed completely outside of the main building.

The target house is a 12-foot diameter cylinder, tilted so that its axis is parallel to the principal axis of the condenser mirror. The floor of this house is made similar to stair steps, their size and shape dependent on the tilt angle.

If a shutter is thought necessary in this design, it should be placed in the plane of the target house as in the Cloudcroft design.

III. The Heliostat

The heliostat of this proposed solar furnace consists of a number of parallel rows of flat mirrors, 4 x 4 feet, mounted on a horizontal ground level turntable. The extreme cases of heliostat mirror position may be calculated from the altitude and azimuth data of Table XXXIII, which is correct for a location at North Latitude 33° .

Table XXXIII

Date	Hour Angle	Azimuth	Altitude
June 21	0 ^h	180°	80° 30'
"	-3 ^h	91° 37'	49° 33'
Dec. 21	0 ^h	180°	33° 40'
"	-3 ^h	136° 41'	19° 41'

The minimum slope angle of the heliostat mirrors, assuming a 30° angle of incidence of the flux onto the target, is determined from the December 21 altitude of the sun of 33° 30' at noon. All other hours and days of the year require a larger angle. A choice of 1° and 45' for the minimum slope angle for the heliostat mirrors for this hour and date will permit a slight spacing between the upper and lower faces of adjacent mirrors if the rows of mirrors slightly overlap, and if they are 48 inches wide and 1/4 inch thick. Figure 50 indicates the angles which occur in the extreme case.

The mirror rows of the heliostat should slightly overlap one another, the one closer to the condenser overlapping the next row farther away in order to minimize the reflection loss due to mirror edges. A suggested spacing is 47 1/2 inches. If the mirror edges are sharp, the loss in reflection at the edge is due to the cone of the sun and to the fact that the mirrors are back surface reflecting as shown in Figure 51.

Comparing the edge loss in overlapping mirrors with that in flush-mounted mirrors, as in the present design for the Cloudcroft furnace, it is seen that the loss due to the cone of the sun is present in both types of mounting. Any spacing between flush-mounted adjacent mirrors produces a loss not seen in overlapped mirrors. This applies to the beveled edges of the mirrors as well. The fact of back surfacing produces a loss common to both types of mounting. This back-surface loss increases with increasing angles of incidence on the mirror and therefore would be larger with a South-facing solar furnace than with a North-facing one.

The rotation of each row of heliostat mirrors about its horizontal axis should be controlled by a sun-tracking servo system which might be mounted in the unused center part of the heliostat turntable. It should be possible to introduce an error signal into the sun-tracking servo network in order to defocus the optical system quickly. If such could be accomplished, then the need for an independent shutter might be eliminated completely with a resulting increase in available flux of about 8% above that of the present plan.

IV. The Turntable

The several rows of heliostat mirrors are mounted as a unit on a large turntable whose axis of rotation may coincide at the ground level with the intersection of the condenser mirror axis and the ground or it

may rotate about any point in the turntable, provided that point is on the center line of the optical system. The turntable is large, but since it may be supported on a number of concentric horizontal tracks its rigidity requirement should not be excessive. If an angle of 30° between the condenser mirror axis and the horizontal will suffice, then the heliostat mirror supports may be mounted in a horizontal plane. If this angle is not sufficient for the furnace user, then the turntable surface must be raised on the side toward the condenser through an angle equal to the difference between the desired angle and 30° .

If the turntable surface is to be horizontal, then its shape for a particular instant must be an ellipse, and for a 105-foot condenser at 30° the ellipse will have a minor axis of 105 feet and a major axis of 210 feet. For use from 9:00 a.m. to 3:00 p.m. over a period of a year, the extreme rotation of the heliostat turntable will occur on June 21 in the amount of $45^\circ 36'$ to the east and west of the noon position.

As stated above, the rotation of the heliostat turntable may be about a number of points but for the sake of economy should be about that point where the total area of the turntable is a minimum. The shape of the heliostat, as required for center rotation, is shown in Figure 52. The areas for rotation of the turntable about its center and about one end are approximately as follows:

Rotation about one end	52,000 ft ²
Rotation about the center	27,500 ft ²

Since these represent the extreme cases, it is obvious that center rotation is the desirable type.

The areas above and the dimensions of Fig. 52 have been calculated as though the sun were a point source. It can be shown that the dimensions of the surface of the heliostat should be enlarged on each side by an amount αl where α is the mean angular diameter of the sun and l is the distance from a particular point at the edge of the heliostat to the corresponding point on the condenser. These additional widths are given in Table XXXIV for the points as indicated in Figure 52.

Table XXXIV.

Points	Addition to the Width
a, e	0.88 ft
b, c, d	1.25 ft
f, g, h	0.41 ft
j, k	0.56 ft
l, m	0.70 ft

V. Conclusion

A comparison of the advantages and disadvantages of this proposal and the present design for the Department of Defense solar furnace is presented as a conclusion to this report.

a. Advantages

(1) One high stationary structure required rather than one high stationary plus one movable and one high accessory structure.

(2) Factory type construction may be used for the main building.

(3) All working spaces will be under one roof.

(4) Radiation flux is incident on sample from above.

(5) Heliostat mirrors may be aligned and cleaned from ground level.

(6) Condenser mirror is protected and should stay clean for long periods.

(7) Condenser mirror may be realigned or repaired in bad weather down-time of the furnace.

(8) Heliostat mirrors may face downward when not in use and, if provided with shed cover, may be cleaned in adverse weather down-time of the furnace or at night.

(9) Eliminates a difficult wind load problem for an extremely large tilting structure.

(10) This proposal brings the target house lower to the ground.

(11) The shutter might be eliminated with a saving in flux.

b. Disadvantages

(1) The single structure required is some 50% higher.

(2) Target house stands at an angle with some less working space available.

(3) Heliostat turntable is somewhat larger in area in this proposal but will carry some less load.

(4) Shutter, if required, will cause somewhat greater loss in flux and, being larger, will be somewhat more difficult to construct.

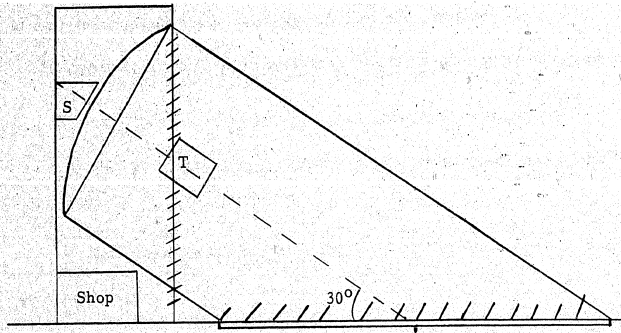


FIGURE 49

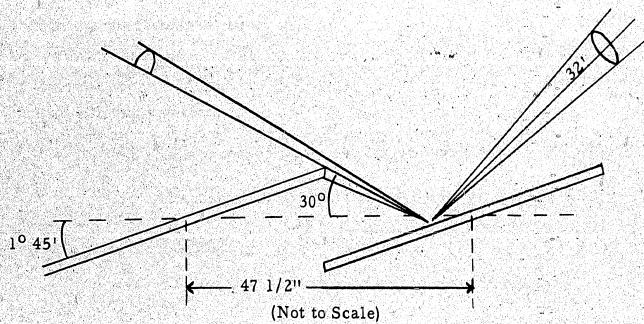


FIGURE 50

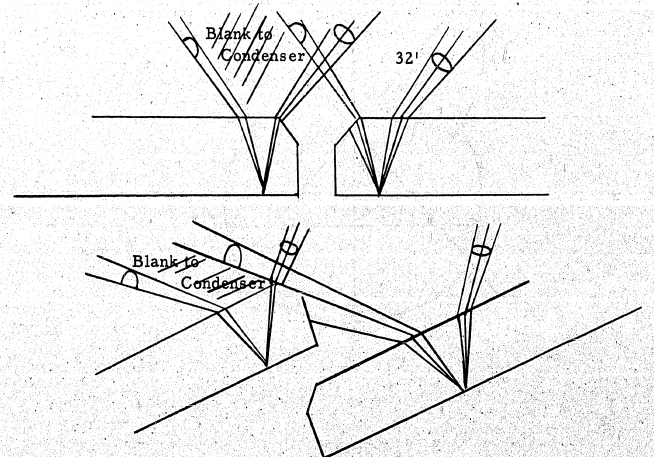


FIGURE 51

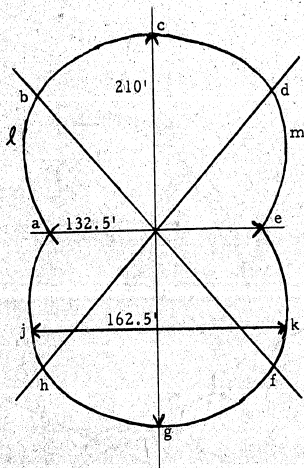


FIGURE 52

<p>AD 135014 Air Force Missile Development Center Holloman AFB, New Mexico SOLAR FURNACE SUPPORT STUDIES, by Scientific Consultants to the Opera- tions Research Office, 1958. 221p incl. illus. 19 ref. (AFMDC TR 58-7) Unclassified report Pyrheliometer measurements showing solar energy available at the pro- posed site are followed by appraisals of potential performance of solar furnaces. Basic optical considera- tions are explained. Absorption and reflection in solar furnace (over)</p>	<p>UNCLASSIFIED</p>	<p>AD 135014 Air Force Missile Development Center Holloman AFB, New Mexico SOLAR FURNACE SUPPORT STUDIES, by Scientific Consultants to the Opera- tions Research Office, 1958. 221p incl. illus. 19 ref. (AFMDC TR 58-7) Unclassified report Pyrheliometer measurements showing solar energy available at the pro- posed site are followed by appraisals of potential performance of solar furnaces. Basic optical considera- tions are explained. Absorption and reflection in solar furnace (over)</p>	<p>UNCLASSIFIED</p>
<p>AD 135014 Air Force Missile Development Center Holloman AFB, New Mexico SOLAR FURNACE SUPPORT STUDIES, by Scientific Consultants to the Opera- tions Research Office, 1958. 221p incl. illus. 19 ref. (AFMDC TR 58-7) Unclassified report Pyrheliometer measurements showing solar energy available at the pro- posed site are followed by appraisals of potential performance of solar furnaces. Basic optical considera- tions are explained. Absorption and reflection in solar furnace (over)</p>	<p>UNCLASSIFIED</p>	<p>AD 135014 Air Force Missile Development Center Holloman AFB, New Mexico SOLAR FURNACE SUPPORT STUDIES, by Scientific Consultants to the Opera- tions Research Office, 1958. 221p incl. illus. 19 ref. (AFMDC TR 58-7) Unclassified report Pyrheliometer measurements showing solar energy available at the pro- posed site are followed by appraisals of potential performance of solar furnaces. Basic optical considera- tions are explained. Absorption and reflection in solar furnace (over)</p>	<p>UNCLASSIFIED</p>

<p>AD 135014</p> <p>components are discussed. Rigid body torsional oscillation in heliostats is examined. Transient temperature distribution in a solar target is discussed. An alternate design for a vertical-axis solar furnace is presented.</p>	<p>UNCLASSIFIED</p>	<p>AD 135014</p> <p>components are discussed. Rigid body torsional oscillation in heliostats is examined. Transient temperature distribution in a solar target is discussed. An alternate design for a vertical-axis solar furnace is presented.</p>	<p>UNCLASSIFIED</p>
<p>AD 135014</p> <p>components are discussed. Rigid body torsional oscillation in heliostats is examined. Transient temperature distribution in a solar target is discussed. An alternate design for a vertical-axis solar furnace is presented.</p>	<p>UNCLASSIFIED</p>	<p>AD 135014</p> <p>components are discussed. Rigid body torsional oscillation in heliostats is examined. Transient temperature distribution in a solar target is discussed. An alternate design for a vertical-axis solar furnace is presented.</p>	<p>UNCLASSIFIED</p>

<p>AD 135014</p> <p>Air Force Missile Development Center Holloman AFB, New Mexico SOLAR FURNACE SUPPORT STUDIES, by Scientific Consultants to the Operations Research Office, 1958. 221p incl. illus. 19 ref. (AFMDC TR 58-7) Unclassified report</p> <p>Pyreheliometer measurements showing solar energy available at the proposed site are followed by appraisals of potential performance of solar furnaces. Basic optical considerations are explained. Absorption and reflection in solar furnace (over)</p>	<p>UNCLASSIFIED</p>	<p>AD 135014</p> <p>Air Force Missile Development Center Holloman AFB, New Mexico SOLAR FURNACE SUPPORT STUDIES, by Scientific Consultants to the Operations Research Office, 1958. 221p incl. illus. 19 ref. (AFMDC TR 58-7) Unclassified report</p> <p>Pyreheliometer measurements showing solar energy available at the proposed site are followed by appraisals of potential performance of solar furnaces. Basic optical considerations are explained. Absorption and reflection in solar furnace (over)</p>	<p>UNCLASSIFIED</p>
<p>AD 135014</p> <p>Air Force Missile Development Center Holloman AFB, New Mexico SOLAR FURNACE SUPPORT STUDIES, by Scientific Consultants to the Operations Research Office, 1958. 221p incl. illus. 19 ref. (AFMDC TR 58-7) Unclassified report</p> <p>Pyreheliometer measurements showing solar energy available at the proposed site are followed by appraisals of potential performance of solar furnaces. Basic optical considerations are explained. Absorption and reflection in solar furnace (over)</p>	<p>UNCLASSIFIED</p>	<p>AD 135014</p> <p>Air Force Missile Development Center Holloman AFB, New Mexico SOLAR FURNACE SUPPORT STUDIES, by Scientific Consultants to the Operations Research Office, 1958. 221p incl. illus. 19 ref. (AFMDC TR 58-7) Unclassified report</p> <p>Pyreheliometer measurements showing solar energy available at the proposed site are followed by appraisals of potential performance of solar furnaces. Basic optical considerations are explained. Absorption and reflection in solar furnace (over)</p>	<p>UNCLASSIFIED</p>

<p>AD 135014</p> <p>components are discussed. Rigid body torsional oscillation in heliostats is examined. Transient temperature distribution in a solar target is discussed. An alternate design for a vertical-axis solar furnace is presented.</p>	<p>UNCLASSIFIED</p>	<p>AD 135014</p> <p>components are discussed. Rigid body torsional oscillation in heliostats is examined. Transient temperature distribution in a solar target is discussed. An alternate design for a vertical-axis solar furnace is presented.</p>	<p>UNCLASSIFIED</p>
<p>AD 135014</p> <p>components are discussed. Rigid body torsional oscillation in heliostats is examined. Transient temperature distribution in a solar target is discussed. An alternate design for a vertical-axis solar furnace is presented.</p>	<p>UNCLASSIFIED</p>	<p>AD 135014</p> <p>components are discussed. Rigid body torsional oscillation in heliostats is examined. Transient temperature distribution in a solar target is discussed. An alternate design for a vertical-axis solar furnace is presented.</p>	<p>UNCLASSIFIED</p>

STAT